

# Ilham Prasetyo V9 disertation

*by Ilham Prasetyo*

---

**Submission date:** 01-Nov-2021 01:10PM (UTC+0700)

**Submission ID:** 1689756316

**File name:** dissertation\_v9\_turnitin.pdf (1.78M)

**Word count:** 26650

**Character count:** 114532

# CHAPTER 1

## INTRODUCTION

### 1.1 Background and Motivation

The gravitational-wave (GW) astronomy by The Laser Interferometer Gravitational-Wave Observatory (LIGO) collaboration [1] gave rise to many studies about what kind of massive bodies produce such waves in the fabric of space-time. The studies are not only limited to “relativist” but also including contributions from other fields of study, especially astronomy. The process of two massive bodies orbiting each other until they combine gives electromagnetic signals which are detected by radio telescope and so on. From these, people can measure many astronomical properties. From the point of view of astronomy, the coalescing process of two neutron stars can synthesize heavy metals, e.g., silver and platinum. This is just one of the advantages of studying the source of GW. The matter properties of neutron stars, which are still mysterious, can also be examined quite directly.

From the theoretical physics point of view, the GW itself after the coalescence is the playground. If the resulting object after the two massive bodies combined gave an object other than a black-hole dan has compactness larger than a third ( $GM/R > 1/3$ , with  $G$  the Newton constant,  $M$  the mass, and  $R$  the radius), it is said that there will be a series of GW echo [2]. Motivated by this, many proposals had discussed such horizonless ultra-compact objects, which is more massive than a neutron star (NS) whose compactness is much less ( $1/6 < GM/R < 1/3$ ), and their main way to detect it is by the GW echo. One such proposal is called gravastar [3, 4], where the surface of the star acts like a shield that divides de-Sitter space-time inside and the Schwarzschild space-time outside. The surface is said to be a thin shell of ultra-relativistic matter. Interestingly, Carballo-Rubio [5] had proposed how to produce a star similar to gravastar using semiclassical gravity theory (SCGrav). SCGrav can be seen as a modified theory of gravity by adding a term called renormalized stress-energy tensor (RSET) with its strength determined by a coupling constant  $l_p$ .

In this dissertation, we shall discuss SCGrav. The theory predicts two branches of equations called positive and negative branches. The negative branch goes to the standard Tolman-Oppenheimer-Volkoff (TOV) equation in general relativity (GR) in the limit  $l_p \rightarrow 0$ , while the positive branch does not. We focus on the negative branch and compare its differences with TOV GR. This theory is interesting since not only the TOV equation is

modified but the differential equation for the mass itself is also modified significantly.<sup>21</sup> This modification can restrict what type of equation of state (EoS) of the nuclear matter inside the NS.

On the other hand, the recent GW190814 event [6] triggers another excitement. They found a new mysterious compact object whose mass is around  $2.6M_{\odot}$  ( $M_{\odot}$  is the solar mass). There are various studies that tried to determine the nature of this object, since it is known that the most massive neutron star PSR J0740+6620 has mass around  $2.1M_{\odot}$  [7]. The  $0.4M_{\odot}$  gap leads people to investigate what mechanism that allows such object to exist. Some proposed that either it is a black hole (BH) [6, 8, 9, 10] or a fast rotating neutron star (NS) [6, 11, 12, 13, 14]. Other exotic objects are also proposed, e.g., quark star [15, 16, 17, 18, 19, 20, 21] or hybrid star [22, 23], with or without rotation. Some others also proposed that it is possible to obtain an NS with mass around  $2.6M_{\odot}$  using modified gravity theories [24, 25, 26, 27].

In this work, we shall use another modified gravity called Eddington-inspired Born Infeld gravity (EiBI) [28, 29, 30, 31, 32]. The EiBI parameters  $\kappa$  and  $\lambda$  can be used to increase or decrease the maximum mass  $M$  and radius  $R$ . The cosmological constant is related to  $\lambda$  by  $\lambda = \kappa\Lambda_c + 1$ . In Ref. [33], the role of  $\kappa$  has been discussed extensively with  $\lambda$  set to unity or equivalently  $\Lambda_c = 0$ . We shall discuss what is happening if we set  $\Lambda_c \neq 0$ . Then our calculations extract the moment of inertia  $I$  of the NS if it is slowly rotating and its tidal deformability  $\Lambda$  if the NS is perturbed. The results are analyzed in the also compared with the various known observations.

## 1.2 The Outline

In this work, we present our results in two parts. The first part is the result of applying a linear EoS in the SCGrav theory. From this, we analyze the effect of parameter  $l_p$  compared to the standard TOV in GR. The second part is the result of calculating the moment of inertia and the tidal deformation aspect from an NS whose matter is described by Relativistic Mean Field theory (RMF) using the G3 parameter set from Ref. [34]. With this, we compare the results with the observed data from various papers and analyze its impact on the range of  $\kappa$  and  $\Lambda_c$ .<sup>22</sup>

This dissertation is organized as follows. In chapter 1, we briefly discuss the background of our research, the specific problems that we investigate, and the goals. In chapter 2, we briefly explain the tools we use from general relativity. In chapter 3, we briefly discuss a little bit of introduction about the compact and ultra-compact objects including their current status in the research community. In chapter 4, we briefly introduce the notion of neutron stars and we include their current status in the research community. In

chapter 5, we shall very briefly discuss RMF, which is the tool to produce the EoS which will be important to describe the matter content in a particular massive object. The contents will outline the main ideas. In chapter 6, we show the first part of our results, i.e., our analysis of SCGrav. In chapter 7, the second part of our results is shown, i.e., our analysis of the moment of inertia and tidal deformation in EiBI. Lastly, in chapter 8, we discuss the conclusions from both parts of our work. We also include Appendix A and B which, respectively, are essential for the first and second part of our work. Fig. 1.1 may help explain the connection behind the two works.

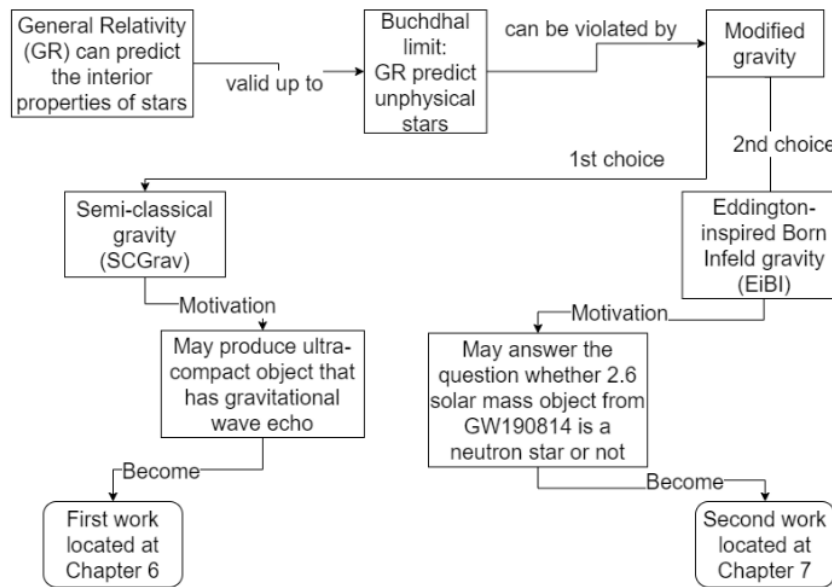


**Figure 1.1:** This is the flowchart that show the motivation on why we do the two works.

### 1.3 Publications

Our dissertation is a compilation of the following papers and proceedings:

- I. Prasetyo, H. S. Ramadhan and A. Sulaksono, “Ultra-compact objects from semi-classical gravity,” Phys. Rev. D **103**, no.12, 123536 (2021) [arXiv:2105.11691 [gr-qc]],
- I. Prasetyo, H. S. Ramadhan and A. Sulaksono, “ $2.6M_{\odot}$  compact object and neutron stars in Eddington-inspired Born-Infeld theory of gravity,” accepted by PRD, [arXiv:2109.05718 [gr-qc]].
- I. Prasetyo, H. S. Ramadhan, and A. Sulaksono, “Exterior solutions of ultra-compact object candidate from semi-classical gravity,” AIP Conference Proceedings **2320**, 050024 (2021).
- I. Prasetyo, H. S. Ramadhan, and A. Sulaksono, “Moment of Inertia of a Slowly Rotating Compact Star in Eddington-inspired Born Infeld Theory,” AIP Conference Proceedings **2374**, 020001 (2021).

## CHAPTER 2

### A BRIEF REVIEW OF GENERAL RELATIVITY

In this chapter, we revisit some tools in general relativity (GR) that are necessary for our work in the following chapters. This review is not comprehensive, so the readers are referred to some literature listed as follows depending on their notable features. These are just some of the literature:

- Some great introductory books: Ryder [35], Carroll [36], and D’Inverno [37];
- A haven for tools, many are not explained in other books: Poisson [38];
- An very popular encyclopedia covering many topics in GR, both theoretical and experimental: Misner, Thorne, and Wheeler [39];
- Another haven for tools that contain many other things, e.g., differential geometry: Nakahara [40] and Baez and Muniain [41];
- Full of elegant derivations but quite advanced contains the short version of singularity theorems: Wald [42];
- Hailed as the classic which contains very mathematical treatment on both black holes and cosmology, very comprehensive discussions on black holes, contains the full version of the singularity theorems: Hawking and Ellis [43];
- A classic book on differential geometry with physicists as the target audience: Nash and Sen [44];
- Covering the origin of Hawking temperature obtained by semi-classical gravity, i.e., quantum field theory employed alongside GR, one the most frontier research topics out there: Birrell and Davies [45], Parker and Toms [46], and Wald [47];
- The books for astrophysicists and nuclear scientists studying NS and other compact stars: Glendenning [48], Weber [49], and Poisson and Will [50].
- A very detailed book to study black-holes and their perturbation aspects: Chandrasekhar [51].

This list contains books that discuss the mathematical background of GR and other books discuss some frontier physics related to GR. The most bottom two points are related to our work in this dissertation.

We start with a few discussions about the physical phenomena in GR. The gravitational field exerted by a typical neutron star (NS) is considerably different compared to the flat space-time, where the special relativity holds and the gravity is still Newtonian. An NS with mass  $M$  around  $1.5M_{\odot}$  and radius  $R$  around 10 km has compactness  $C = GM/R$  (with  $G$  the Newton constant) much larger than the Sun and the Earth, i.e.,  $2C \sim 0.4$  for NS,  $2C \sim 10^{-6}$  for Sun, and  $2C \sim 10^{-9}$  for Earth. So even if the NS is non-rotating, its gravity potential implies the need for GR.

Furthermore, if any massive bodies are rotating, the phenomenon of frame dragging (known as the Lense-Thirring effect) happens. This effect is not intuitive since it has no analogy in Newtonian physics. When Newton first investigates the role of rotation on a bucket filled with water in 1686, he was interested in whether non-uniform motion is relative or not to its surroundings. Newton argued that the water is forced to rise the sides of the bucket due to centrifugal force, so the bucket's rotation is absolute. E. Mach reexamined this argument in 1883 in an attempt to better understand how inertial force arises. He asked if the bucket is fixed and the universe is rotating about it then what causes the water to rise. This is known as Mach's principle. He suggested that if the vessel's thickness and mass are sufficiently large, the surface of the water may depend on the rotation of the vessel. The Einstein formulation of gravity in 1916 made such a question be answered with explicit calculations by Lense and Thirring [52] in 1918.

In the following, we try to explain what the Lense-Thirring effect is. A gyroscope is an apparatus that can automatically orient itself, which is why it is used in airplanes. In special relativity, the precession of a gyroscope is dependent on the force which influences the gyroscope. From GR, there exist two more called de-Sitter precession and Lense-Thirring precession. The de-Sitter precession is similar to Thomas's precession with the force replaced by gravitational force with a factor of 3. The Lense-Thirring precession, on the other hand, depends not on force but angular momentum from the rotating massive body [35]. This effect is the basis of GR tests performed by the Gravity Probe B satellite.

Now that we can somehow see that the fabric of space-time is real, we turn to the mathematical description of such a thing. The origin of the tools was already been developed by Riemann and other mathematicians, and it is connected to physics by Einstein. It came from a branch of study in mathematics called differential geometry. Differential geometry turns not only useful for gravity but also useful as a tool to study other things, such as the Aharonov-Bohm phenomenon and Yang-Mills field. But in this dissertation, we intend to restrict our review on GR only to the tools necessary for our work.

Suppose a particle's trajectory in a space is a line denoted by a function  $f(s)$  with an auxilliary parameter  $s$ . The position of the particle in that line can be denoted as a vector. In Newtonian mechanics, this vector is basically a triple of real numbers denoted

as  $x^i = (x^1, x^2, x^3)$ . In special relativity, we know that time is not an arbitrary parameter so it is included as  $x^0 = ct$  in a 4-vector  $x^\mu = (x^0, x^1, x^2, x^3)$  or more generally,

$$\vec{x} = x^0 \hat{e}_0 + x^1 \hat{e}_1 + x^2 \hat{e}_2 + x^3 \hat{e}_3 \equiv x^\mu \hat{e}_\mu. \quad (2.1)$$

Here  $\hat{e}_\mu$  is called *vector basis*. We omit the sum symbol in the last equality since we use the Einstein summation convention. The component of this vector  $x^\mu$ , denoted by an superscript index, is called *contravariant* quantity. The particle should have the “speed” when moving along the line. This can be extracted by the chain rule

$$\frac{d}{ds} f = \left( \frac{dx^0}{ds} \frac{\partial}{\partial x^0} + \frac{dx^1}{ds} \frac{\partial}{\partial x^1} + \frac{dx^2}{ds} \frac{\partial}{\partial x^2} + \frac{dx^3}{ds} \frac{\partial}{\partial x^3} \right) f = \frac{dx^\mu}{ds} \frac{\partial}{\partial x^\mu} f. \quad (2.2)$$

The form of  $d/ds$  in the right hand side, in mathematics, is called *the* vector with basis vector  $\hat{e}_\mu = \partial/\partial x^\mu$ . So in a sense, the basis vector acts like an operator acting on a scalar function.

In physics, we usually denote an infinitesimal quantity of, say a function  $F(x^\mu)$ , as

$$dF = \frac{\partial F}{\partial x^\mu} dx^\mu. \quad (2.3)$$

The components can be relabeled as, e.g.,  $\omega_\mu = \partial F/\partial x^\mu$ . This quantity, with subscript index, is called *covariant* quantity. In mathematics, a quantity resembling  $dF$  is called covector and  $dx^\mu$  is called *covector basis*. In general, covector basis is denoted as something with superscript index  $\hat{\omega}^\mu$  while the vector basis use subscript index:

$$\omega = \omega_\mu \hat{\omega}^\mu. \quad (2.4)$$

The definition of covector and vector in turn is necessary to define the generalisation of dot product. While the vector basis act like an operator to a scalar function, the covector basis act like an operator to vector basis. This condition

$$\hat{\omega}^\mu(\hat{e}_\nu) = \delta_\nu^\mu \quad (2.5)$$

is necessary to obtain the dot product between a covector  $\underline{\omega}$  and a vector  $\vec{V}$

$$\underline{\omega}(\vec{V}) = \omega_\mu V^\mu. \quad (2.6)$$

From now on, we shall call something with superscript (subscript) index, e.g.,  $V^\mu$  ( $\omega_\mu$ ), as a vector (covector).

Another way to obtain a dot product of two vectors can be used via the so-called

**Universitas Indonesia**

*metric tensor*  $g_{\mu\nu}$ . In a *finite* dimensional space-time, we can obtain the covector of  $V^\mu$  by

$$V_\mu = g_{\mu\nu} V^\nu. \quad (2.7)$$

In physics, this metric tensor is usually introduced by the infinitesimal length of a flat space-time in Cartesian coordinate

$$ds^2 = -c^2 dt^2 + dx^2 + dy^2 + dz^2 = g_{\mu\nu} dx^\mu dx^\nu. \quad (2.8)$$

So the metric  $g_{\mu\nu}$  can be visualized as a  $4 \times 4$  matrix, whose diagonal components has sign  $(-, +, +, +)$ . Its inverse is denoted as  $g^{\mu\nu}$ , which can be used to make a subscript index become superscript index

$$V^\mu = g^{\mu\nu} V_\nu. \quad (2.9)$$

Now we introduce the notion of tensors. A scalar  $f$ , vector  $V^\mu$ , covector  $\omega_\mu$ , metric  $g_{\mu\nu}$  and inverse metric  $g^{\mu\nu}$ , respectively, are tensor rank  $(0, 0)$ ,  $(1, 0)$ ,  $(0, 1)$ ,  $(0, 2)$ , and  $(2, 0)$ . Except for the scalar, the tensor indices denote the *local* version of the tensor. In mathematics a tensor  $T$  rank  $(1, 1)$  is written locally in a coordinate system  $x^\mu$  as

$$T = T^\mu{}_\nu \left( \frac{\partial}{\partial x^\mu} \otimes dx^\nu \right). \quad (2.10)$$

The entity inside the round bracket can be thought of as the basis of the said tensor. If we choose another coordinate system, say  $x'^\mu$ , we write the tensor as

$$T = T^{\mu'}{}_{\nu'} \left( \frac{\partial}{\partial x'^\mu} \otimes dx'^\nu \right). \quad (2.11)$$

The tensor  $T$  is still the same but described with different set of coordinates. The two coordinate is related to each other by  $x'^\mu = x'^\mu(x^\nu)$ . With chain rule, the vector basis and the covector basis can be related to each other by

$$\frac{\partial}{\partial x^\alpha} = \left( \frac{\partial x'^\mu}{\partial x^\alpha} \right) \frac{\partial}{\partial x'^\mu}, \quad (2.12)$$

$$dx^\alpha = \left( \frac{\partial x^\mu}{\partial x'^\alpha} \right) dx'^\mu, \quad (2.13)$$

Since the round bracketed entities above are scalars, then we obtain

$$T^{\mu'}{}_{\nu'} = T^\alpha{}_\beta \frac{\partial x'^\mu}{\partial x^\alpha} \frac{\partial x^\beta}{\partial x'^\nu}. \quad (2.14)$$

This is the *coordinate transformation condition* that should be satisfied by any tensor. A

tensor can have either symmetric or antisymmetric properties in its indices. The symmetric property is denoted by round brackets and the antisymmetric property by square brackets. For example, a tensor rank  $(2, 0)$  is symmetric if

$$T^{(\mu\nu)} = \frac{1}{2!}(T^{\mu\nu} + T^{\nu\mu}), \quad (2.15)$$

or antisymmetric if

$$T^{[\mu\nu]} = \frac{1}{2!}(T^{\mu\nu} - T^{\nu\mu}). \quad (2.16)$$

Now we introduce the Lie derivative. We shall denote partial derivative over  $x^\mu$  as  $\partial_\mu$ . Since a vector intuitively has magnitude and orientation, covector and tensors, in general, have their magnitude and orientation. Suppose we have a curved space-time. Suppose there is a tensor  $T^{\mu\nu}(x)$  and a vector  $X^\mu$  where both are “attached” at the same point  $p$  in the space-time. The tensor is then moved in a direction of a vector  $X$ , which became  $T'^{\mu\nu}(x')$  and the new position  $q$  is denoted as

$$x'^\mu = x^\mu + X^\mu(x)\delta u, \quad (\delta u \text{ is a small constant}). \quad (2.17)$$

By the coordinate transformation condition, we have

$$T'^{\alpha\beta}(x') \stackrel{26}{=} T^{\mu\nu}(x) \frac{\partial x'^\alpha}{\partial x^\mu} \frac{\partial x'^\beta}{\partial x^\nu} = T^{\mu\nu}(x) + [\partial_\mu X^\alpha T^{\mu\beta}(x) + \partial_\nu X^\beta T^{\alpha\nu}(x)], \quad (2.18)$$

where we omit  $\mathcal{O}(\delta u^2)$ . Now we want to compare it with the original tensor  $T^{\mu\nu}(x')$  if its origin is at  $q$ . By Taylor expansion up to first order, we have

$$T^{\mu\nu}(x^\alpha + X^\alpha(x)\delta u) = T^{\mu\nu}(x) + \delta u X^\alpha \partial_\alpha T^{\mu\nu}(x). \quad (2.19)$$

The definition of the *Lie derivative*, in our case here, is just the difference between  $T^{\mu\nu}(x')$  and  $T'^{\mu\nu}(x')$  as  $\delta u \rightarrow 0$ ,

$$\mathbf{L}_X T^{\mu\nu} = \lim_{\delta u \rightarrow 0} \frac{T^{\mu\nu}(x') - T'^{\mu\nu}(x')}{\delta u}. \quad (2.20)$$

This gives us

$$\mathbf{L}_X T^{\alpha\beta} = X^\mu \partial_\mu T^{\alpha\beta} - \partial_\mu X^\alpha T^{\mu\beta} - \partial_\nu X^\beta T^{\alpha\nu}. \quad (2.21)$$

To find  $\mathbf{L}_X T_{\alpha\beta}$ , one can use  $x'^\mu = x^\mu + X^\mu(x')\delta u$ , which gives us

$$\mathbf{L}_X T_{\alpha\beta} = X^\mu \partial_\mu T_{\alpha\beta} + \partial_\alpha X^\mu T_{\mu\beta} + \partial_\beta X^\mu T_{\alpha\mu}. \quad (2.22)$$

If the Lie derivative acts on a scalar, it behaves like a partial derivative

$$\mathbf{L}_X f = X^\alpha \partial_\alpha f. \quad (2.23)$$

Now a *Killing vector*  $\xi$  is a vector that satisfies

$$\mathbf{L}_\xi g_{\mu\nu} = 0. \quad (2.24)$$

This vector is special since, along  $\xi$ , the metric is unchanged, thus the space denoted by the metric is also unchanged.  $\xi$  describes what type of *isometry* from the given metric. For example, the surface of a cylinder with radius  $R$ , whose metric is

$$ds^2 = R^2 d\theta^2 + dz^2, \quad (2.25)$$

is of course invariant if we rotate them along  $\phi$ , so  $\xi = \partial_\phi$ .

Next is the affine connection, or simply, connection. The connection is defined so that we have the so-called *covariant derivative*  $\nabla_\mu$  over any tensor is a tensor. The covariant derivative is related to the partial derivative through the *connection*  $\Gamma_{\mu\nu}^\alpha$ . For example,

$$\nabla_\mu T_\beta^\alpha = \partial_\mu T_\beta^\alpha + \Gamma_{\mu\nu}^\alpha T_\beta^\nu - \Gamma_{\mu\beta}^\nu T_\nu^\alpha. \quad (2.26)$$

If the covariant derivative act on a scalar, it became partial derivative

$$\nabla_\alpha f = \partial_\alpha f. \quad (2.27)$$

From the definition of  $\nabla_\mu T^\alpha$  above and the coordinate transformation condition, one can obtain

$$\Gamma'{}^\beta_{\alpha\sigma} = \frac{\partial x^\rho}{\partial x'^\sigma} \frac{\partial x^\lambda}{\partial x'^\alpha} \frac{\partial x'^\beta}{\partial x^\gamma} \Gamma^\gamma_{\lambda\rho} - \frac{\partial x^\lambda}{\partial x'^\alpha} \frac{\partial x^\rho}{\partial x'^\sigma} \frac{\partial^2 x'^\beta}{\partial x^\lambda \partial x^\rho}. \quad (2.28)$$

The second term tells us that the connection is not a tensor. There is the so-called *torsion tensor*  $T_{\mu\nu}^\alpha$  which is the antisymmetric part of connection

$$T_{\mu\nu}^\alpha = \Gamma_{\mu\nu}^\alpha - \Gamma_{\nu\mu}^\alpha. \quad (2.29)$$

GR is torsionless, so the connection is symmetric

$$\Gamma_{\mu\nu}^\alpha = \Gamma_{\nu\mu}^\alpha. \quad (2.30)$$

From now on, we shall focus on zero torsion theory. The explicit expression of  $\Gamma_{\mu\nu}^\alpha$  can

**Universitas Indonesia**

be obtained by the fact that the metric vanishes if a covariant derivative act on it,

$$\nabla_\alpha g_{\mu\nu} = 0. \quad (2.31)$$

From this, one can obtain

$$\Gamma_{\mu\nu}^\alpha = \frac{1}{2} g^{\alpha\beta} (\partial_\mu g_{\beta\nu} + \partial_\nu g_{\beta\mu} - \partial_\beta g_{\mu\nu}). \quad (2.32)$$

An *affine geodesic* is a curve in the space-time whose tangent vectors are parallel to the curve itself. Suppose that the curve, whose auxilliary parameter is  $u$ , is located at  $x^\mu$  and its tangent vector is  $X^\mu = dx^\mu/du$ , then it is an affine geodesic if

$$X^\alpha \nabla_\alpha X^\beta = \lambda X^\beta. \quad (2.33)$$

If there is an auxilliary parameter  $s$  that is defined such that all the tangent vectors have same length, then  $s$  become *affine parameter* and the above equation becomes *geodesic equation* (same as above but  $\lambda = 0$ ).

Now we turn to the *Riemann tensor* which contains all the information about the curvature of space-time. It is defined as

$$R^\alpha{}_{\mu\beta\nu} = \partial_\beta \Gamma_{\mu\nu}^\alpha - \partial_\nu \Gamma_{\mu\beta}^\alpha + \Gamma_{\beta\delta}^\alpha \Gamma_{\mu\nu}^\delta - \Gamma_{\nu\delta}^\alpha \Gamma_{\mu\beta}^\delta. \quad (2.34)$$

It has four properties:

1.  $R_{\alpha\mu\beta\nu} = -R_{\alpha\mu\nu\beta} = -R_{\mu\alpha\beta\nu}$ ,
2.  $R_{\alpha\mu\beta\nu} = R_{\beta\nu\alpha\mu}$ ,
3. the *first Bianchi identity*  $R^\alpha{}_{[\mu\beta\nu]} = 0$ ,
4. and the *second Bianchi identity*  $R^\alpha{}_{\mu[\beta\nu;\kappa]} = 0$ , with  $T_{\alpha;\kappa} = \nabla_\kappa T_\alpha$ .

The Riemann curvature is also named as the *intrinsic curvature*, since from an observer can now the curvature of a  $d$ -dimensional space-time  $\mathcal{M}$  even though he/she lives in  $\mathcal{M}$  itself. Then there is the so-called *Ricci tensor*, which is the trace of the Riemann tensor

$$R_{\mu\nu} = R^\beta{}_{\mu\beta\nu}. \quad (2.35)$$

The Ricci tensor does not contain all the information about the intrinsic curvature. This

missing information is contained in the *Weyl tensor*

$$\begin{aligned} C_{\alpha\beta\mu\nu} &= R_{\alpha\beta\mu\nu} + \frac{1}{d-2}(R_{\alpha\nu}g_{\beta\mu} + g_{\alpha\nu}R_{\beta\mu} - R_{\alpha\mu}g_{\beta\nu} - g_{\alpha\mu}R_{\beta\nu}) \\ &\quad + \frac{R}{(d-2)(d-3)}(g_{\alpha\mu}g_{\beta\nu} - g_{\alpha\nu}g_{\beta\mu}), \end{aligned} \quad (2.36)$$

with  $d$  the dimension of the space-time. We can see that  $C^{\beta}_{\mu\beta\nu} = 0$ .

Now that all basic ingredients are in place, we can discuss the Einstein Field Equation (EFE)

$$R_{\mu\nu} - \frac{1}{2}Rg_{\mu\nu} = \frac{8\pi G}{c^4}T_{\mu\nu}. \quad (2.37)$$

The stress-energy tensor  $T_{\mu\nu}$  contains the matter information. In general  $T^{00} = \epsilon/c^2$  where  $\epsilon$  the energy density,  $T^{0i}$  = the momentum density,  $T^{ij}$  =  $p$  with  $p$  the pressure, and  $T^{ij}$  = the shear stress ( $i \neq j$ ). If one use Lagrangian density  $\mathcal{L}$  to describe the matter, then one can use

$$T_{\mu\nu} = -2\frac{\partial \mathcal{L}}{\partial g^{\mu\nu}} + g_{\mu\nu}\mathcal{L} \quad (2.38)$$

to obtain the stress-energy tensor components. One can derive the identity  $\nabla_{\mu}G^{\mu\nu} = 0$  from  $R^{\alpha}_{\mu[\beta\nu;\kappa]} = 0$  by first contracting  $\alpha$  with  $\beta$  then contracting  $\mu$  with  $\nu$ . By EFE, we have the covariant conservation equation

$$\nabla_{\mu}T^{\mu\nu} = 0. \quad (2.39)$$

This equation is necessary since both the continuity equation and the Euler equation can be derived from it [50]. The EFE can be derived from action, but it will be a long dicussion so we refer the readers to Ref. [38] for the details. We only show the useful relations for varying the action [45, 46, 37, 35]:

$$\delta g_{\mu\nu} = -g_{\mu\alpha}g_{\nu\beta}\delta g^{\alpha\beta}, \quad (2.40)$$

$$\delta\sqrt{-g} = -\frac{1}{2}\sqrt{-g}g_{\mu\nu}\delta g^{\mu\nu}, \quad (2.41)$$

$$\delta R = R_{\mu\nu}\delta g^{\mu\nu} + g^{\rho\sigma}g^{\mu\nu}(\delta g_{\rho\mu;\sigma\nu} - \delta g_{\rho\sigma;\mu\nu}), \quad (2.42)$$

$$\delta R^{\alpha}_{\mu\beta\nu} = (\delta\Gamma^{\alpha}_{\mu\nu})_{;\beta} - (\delta\Gamma^{\alpha}_{\mu\beta})_{;\nu}, \quad (2.43)$$

$$\delta\Gamma^{\lambda}_{\mu\nu} = \frac{1}{2}g^{\lambda\beta}\left[(\delta g_{\beta\nu})_{;\mu} + (\delta g_{\beta\mu})_{;\nu} - (\delta g_{\mu\nu})_{;\beta}\right], \quad (2.44)$$

with  $g = \det(g_{\mu\nu})$  and  $T_{\alpha;\kappa} = \nabla_{\kappa}T_{\alpha}$ .

One can obtain the Riemann tensor components using an algebraic program, e.g., *Mathematica*. There is another method, which uses differential forms rather than  $\Gamma^{\mu}_{\nu\rho}$ , called *tetrad method*. We show its steps in the Appendix.

## CHAPTER 3

### COMPACT AND ULTRA-COMPACT OBJECTS

The excitement over GW astronomy by LIGO and Virgo [1] in the last 5 years since the GW150914 event gave rise to many investigations on what mechanisms produce the waves. From the astronomical point of view, there is an emphasis on the possibility of finding the synthesizing process of heavy metals, e.g., silver, and platinum. This hypothesis can be tested from the collision of two neutron stars at the GW170817 event. From the theoretical physics point of view, some investigations ask what kind of heavy objects may mimic black holes. These objects are horizonless and usually called ultra-compact objects (UCOs). These objects are more compact than the known compact objects, e.g., neutron stars (NSs) or white dwarfs. The existence of these UCOs, if they are the final state of two massive bodies colliding that produce GW, can be detected by the existence of the so-called GW echo.

As we have known, black holes (BHs) cannot be observed directly and their existence is usually confirmed by their intense gravity effects. One such effect is the famous light deflection, known since the observation of a total solar eclipse at the island of Principe at Sobral on 29 May 1919 by Eddington and his colleagues. Since Eddington only measures the deflection by the Sun, the deflection of black holes is much more tremendous than the visualization is very weird. One can see an approximate illustration of such rotating black holes in the film Interstellar, which includes Kip Thorne as its staff.

The other effect that triggers recent excitement is the GW. One such apparatus is the LIGO, the abbreviation of Laser Interferometer Gravitational-Wave Observatory. The success of detecting the event at 09.51 UTC on 14 September 2015 led Rainer Weiss, Kip Thorne, and Barry C. Barish, the initiators of the LIGO project, as the receiver of the Nobel Prize in Physics in 2017. This achievement opens the possibility to observe the universe not only by using electromagnetic waves, which is done a long time ago by astronomers but also by looking at ripples of space-time.

When two massive objects going revolve around each other and they are going closer and closer, the curve of space-time around these two undergoes rapid changes. This change is like a perturbing fabric of elastic sheets, which will produce waves. These waves can be detected by a laser interferometer, whose configuration is such that the two separated lights annihilate each other on a screen. When a GW passes by, the interferometer can detect two types of waves depending on their polarization. One of them is called the plus-polarized GW and the other is the cross-polarized GW. This makes one

of the arms of the interferometer slightly shorter and the other slightly longer. When this happens, light appears on the screen and its intensity oscillate. Of course, we left many details but the main idea is very simple.

In the ring-down phase, i.e., the two massive objects had combined, the wave died down so quickly into complete silence if the final object is a BH. On the other hand, if the final object is a UCO, it has been calculated that the silence will be followed by a series of echoes. As an illustration of how massive these UCOs are, they are much heavier and their size is smaller than an NS but still lighter than a BH. The compactness  $C = GM/R$  of an NS is  $\sim 0.2$  but for a black-hole  $C = 1/2$ , so there is a large gap between NS and BH. In general, massive objects are categorized by compactness as follows [2]:

- if  $2C > 1/3$ , then it is a compact object,
- if  $2C > 2/3$ , then it is an ultra-compact object (UCO),
- if  $2C > 8/9$ , then it violates the Buchdhal limit
- if  $2C > 1/(1 + 0.019)$ , it is a clean-photon sphere objects (ClePhO), and
- if  $2C > 1/(1 + 10^{-40})$ , then it is a near-horizon quantum structure.

The compact object criteria are fulfilled if the spherical object has an innermost stable circular orbit (ISCO) at  $r = 6GM$ . The UCO criteria are fulfilled if the spherical object has an unstable light ring (or photon sphere) at  $r = 3GM$ . The Buchdhal limit  $C = 4/9$  is the limit of GR as a prediction of any horizonless massive object. This came from the Buchdhal theorem, which roughly says that the pressure at the center goes to infinity if the system satisfies the following conditions:

<sup>14</sup>

1. GR is the correct theory of gravity,
2. the solution is spherically symmetric,
3. the matter is described by a single perfect fluid,
4. the fluid is isotropic or mildly anisotropic  $p_r \geq p_t$ ,
5. the radial pressure and the energy density are both nonnegative ( $p_r \geq 0, \rho \geq 0$ ), and
- <sup>8</sup> 6. from the center to the surface of the star, the energy density decreases  $\rho'(r) < 0$ .

The ClePho has the following unique signature, i.e., its gravitational wave behavior is identical to black holes at early times but display unique signatures of their surface at late

times. The near-horizon quantum structure came from looking at the tidal Love number  $k_2$ , which is estimated to be  $k_2 \sim 1/|\log \epsilon| \sim \mathcal{O}(10^{-3} - 10^{-2})$ , where  $\epsilon = 1/2C - 1$ . As a comparison, this number is very small compared to a typical neutron star who has  $k_2 \sim 200$ .

For the echo to exists, the final object from the coalesce should at least have compactness  $C > 1/3$ . This is because the effective potential  $V_{eff}$  that produces the GW echo has a spherical barrier located at the so-called unstable photon sphere at  $r = 3GM$  [53]. (The unstable term is due to both  $V'_{eff}(3GM) = 0$  and  $V''_{eff}(3GM) < 0$ .) The photon sphere's existence can be derived from the geodesic of massless particles in the space-time with Schwarzschild metric, but it does not imply that GW echo can be produced. The GW came from the TT-tensor (transverse traceless) part of metric perturbation. From the perturbation calculation, we can obtain the effective potential  $V_{eff}$ .

The GW echo frequency  $f_{echo}$  can be calculated using the object's compactness by the proper time delay [54]

$$\tau_{echo}^{(num)} = \int_0^{3GM} \sqrt{-\frac{g_{rr}}{g_{tt}}} dr. \quad (3.1)$$

This formula needs the complete information of the interior of the object. The integration from  $r = 0$  to  $r = 3GM$  means that the waves are trapped at a region between  $r = 3GM$  and  $r = 0$ , assuming that the gravitational wave penetrates the UCO. When the wave cannot penetrate and being reflected by the object's surface, integrating Eq. (3.1) from  $r = R$  rather than  $r = 0$  will produce [2]

$$\tau_{echo}^{(approx)} \sim 4M|\log \epsilon|, \quad (3.2)$$

with  $\epsilon = 1/2C - 1$  and  $f_{echo} = \pi/\tau_{echo}$ . Eq. (3.2) is sufficient to estimate the order of magnitude of the frequency.

The existence of such echo had been observed. The GW170817 event, a merger of two neutron stars that produce a BH remnant with mass around  $2.6\text{-}2.7 M_\odot$  and dimensionless spin around 0.84-0.87, produced an echo which had been calculated in Ref. [55] and the result is  $f_{echo} \simeq 72$  Hz. This was predicted in Ref. [56] to be compatible with a toy model of an incompressible star with a mass of around  $2\text{-}3 M_\odot$ .

Many UCO proposals are compiled in a review by Cardoso and Pani [2]. One of them is called gravastars [3, 4]. Inside the surface of the gravastar lies another de-Sitter space connected to the Schwarzschild space-time by a thin shell of ultrarelativistic matter. Carballo-Rubio [5] utilized the theory of semi-classical gravity to obtain a different type of TOV-like equation and the result has many similar features with gravastar. In the next chapter, we shall present our analysis on the Carballo-Rubio model [5].

This page intentionally left blank

## CHAPTER 4

# NEUTRON STARS

### 4.1 Neutron Stars

In this section, we shall review some features of neutron stars (NSs). Our discussion will be very short and basic. For comprehensive discussions, readers are referred to Glendenning [48].

Chadwick in 1932 discovered the neutron particle. One year later, Baade and Zwicky investigate supernovae and they conceived the notion of NS. When the presupernova star's core became heavier by the production of iron from nuclear fusion, the mass increases until the gravitational force wins over the pressure from the matter, hence the core collapse. But then the collapse is stopped by neutrons in the core of the star, the matter bounces off the hard iron core, making the supernova explosion. So the type II supernova explosion release so much debris due to the highly compact object formed in the center of the presupernova star called NS. (Type Ia supernova is the result of mergers of two white dwarfs, so its process is different and it happens very rarely.)

NSs are partially supported by neutron degeneracy pressure, an effect caused by the Pauli exclusion principle (similar to electron degeneracy pressure in white dwarfs). This pressure is only able to negate the gravitational pull if the mass is no more than  $0.7M_{\odot}$ . Beyond this, repulsive nuclear forces are needed. This mechanism gives the so-called the Tolman-Oppenheimer-Volkoff (TOV) limit  $M \lesssim 2.0M_{\odot}$ . Beyond this, the matter collapses into a more dense star, e.g., quark star, or black-hole. (In the case of the white dwarf, the Chandrasekhar limit  $M \lesssim 1.4M_{\odot}$  is the boundary between the white dwarf and neutron star.)

How about protons? It is common to assume neutral net charge distribution for massive objects. So the pre-collapsed star should have the net charge from electrons equal to the net charge of the protons. If the mass exceeds the Chandrasekhar limit, the electron degeneracy pressure is losing against the gravitation, so the electrons, protons, and neutrons are packed together. Then due to the inverse beta decay process, protons and electrons combined producing neutrons and electron neutrinos. Even though the neutrons are unstable due to the beta decay, the inverse beta decay stabilizes it so the neutrons dominate the matter.

The TOV limit, if the strong forces are included, is actually in the range of  $1.5 - 3M_{\odot}$ . This large uncertainty exists because the EoS for extremely dense matter is unknown. So

to make the range narrower.<sup>27</sup> people use observations. The empirical lower bound on the TOV limit is usually taken from the mass of PSR J0348+0432, which is  $2.01 \pm 0.04 M_{\odot}$ . On the other hand, NS radius is somehow more difficult to know for different masses of NSs. Usually, the radius is obtained from canonical NS with mass  $1.4 M_{\odot}$ . There are calculations by Landry et al [57] and Jiang et al [58] whose result is  $R_{1.4} = 12.32^{+1.09}_{-1.47}$  km and  $R_{1.4} = 12.1^{+1.2}_{-0.8}$  km, respectively. The most stringent one is calculated by Capano et al [59] whose result is  $R_{1.4} = 11.0^{+0.9}_{-0.6}$  km.

The pre-supernova star is generally rotating, so the NS produced should also rotate faster since the radius is smaller. An NS cannot have a period of (uniform) rotation such that its frequency is more than the so-called Kepler frequency [48]

$$\Omega_K \approx 0.625 \sqrt{M/R^3}. \quad (4.1)$$

The Kepler frequency is the absolute limit of rotation, where beyond the matter will fall apart due to centripetal force. Although this result is Newtonian, it was justified by GR since it is accurate to better than 10%. This absolute limit gives the lowest possible period, called the Kepler period

$$P_K = \frac{2\pi}{\Omega_K} \approx 0.0276 \sqrt{\frac{(R/\text{km})^3}{M/M_{\odot}}} \text{ ms}. \quad (4.2)$$

This period is also called the mass-shedding limit. The result is shown in Fig. 7.2 in Ref. [48]. There the NS with  $1.442 M_{\odot}$  cannot have a rotational period less than 0.33 ms. The region forbidden by GR is denoted by the following constraint:

$$P > 0.167 \frac{M}{M_{\odot}} \text{ ms}, \quad (4.3)$$

<sup>8</sup> assuming that  $GM/R < 4/9$ . For a star with mass equal to that of PSR 1931+16, i.e.,  $M = 1.441 M_{\odot}$ , it yields  $P > 0.24$  ms.

There are at least two stability conditions for NS. The first one is  $dM/d\rho_c > 0$ , i.e., the mass increases as one increases the central energy density. The maximum mass is usually located at the point where  $dM/d\rho_c = 0$ . The other criteria are from radial perturbation analysis. By this method, one can see the possibility of the star will expand or contract if it is perturbed along the radial direction. If it tends to either expand or contract after a little nudge, then it is unstable.

## 4.2 The $\sim 2.6M_{\odot}$ NS from GW190814 event

The most recent known problem in compact object is the nature of  $2.50 - 2.67M_{\odot}$  massive secondary object detected in the gravitational wave (GW) by LIGO and Virgo collaboration in their GW190814 event [6]. This object has no measurable signature of tidal deformation, and also there is no electromagnetic counterpart on the gravitational wavefront. Much discussions had been published about this object, such as, whether it is a lightest black hole (BH) [6, 8, 9, 10], a fast rotating neutron star (NS) [6, 11, 12, 13, 14], a quark star [15, 16, 17, 18, 19, 20, 21] or a hybrid star [22, 23]. However, one could not exclude the possibility that the secondary object of GW190814 as a super-massive static or at least a slow rotating NS [8, 60, 61]. The latter possibility trigger of other discussions about the appropriate type of equation of state (EoS) of the super-massive NS that satisfy observational constraints [62, 63, 64, 65, 60, 61]. Furthermore, we note that the anisotropic pressure to calculate mass upper limit [66, 67, 68], the possibility of studying primordial black hole [69], the indication of a dark matter candidate called mirror world [70], and the use of modified gravity to explain the GW event [24, 25, 26, 27].

Here we mention some developments on the properties of NS by observations. The maximum mass of NS around  $2.0 M_{\odot}$  came from accurate measurements of massive pulsars such as PSR J0348+0432, PSR J0740+6620, and J6114-2230 [71, 72, 73, 7, 74]. NICER [75] measured the X-ray emissions from the hot spots on the surface of NS, which provide simultaneous pieces of information about the mass and radius of some pulsars. The recent NICER investigations report the mass and radius constraints for PSR J0030+0451 [76, 77, 78]. On the other hand, GW analysis by LIGO and Virgo collaboration from the remnant of two NSs had measured the tidal deformability of the NSs. This analysis can survey a wide range of NS masses and its corresponding central density [79, 80, 81, 6]. The two GW events from the coalescence of two NSs, i.e., GW170817 [79, 80] and GW190425 [6], have been reported. The analysis from these events can provide a stricter constraint to mass and radius of canonical NS (i.e., with a mass around  $1.4M_{\odot}$ ) and thus also restrict the EoS of NS.

Moreover, other studies have been performed to extract accurate information on the properties of the EoS of NSs [57, 58, 82, 83, 84, 85]. These studies are done by systematically examine NS observable measurements and other observable measurements, e.g., NS inertia moment or and nuclear properties. We need to note that to describe NS matter, some use non-relativistic models while others use relativistic models. Several models of NS matter are already proposed, e.g., the relativistic mean-field (RMF) models. Dutra *et al.* [86] had reported that they found only 34 from 263 RMF parameter sets that satisfy constraints from nuclear matter. Furthermore, only 15 out of 35 parameter sets in isotropic NS without hyperons that predict maximum mass around  $2.0 M_{\odot}$ . However,

none of them satisfy the later constraint if the model includes hyperons and other exotic particles. (For details, please see Ref. [87] and the references therein.) This is known as the “hyperons puzzle”.

We need to emphasize that the tension between nuclear physics persists. Some results from NS observations imply that the models of NS EoS should be relatively stiff so that they can produce NS with a maximum mass around  $2.0 M_{\odot}$ . On the other hand, the recent result on the radius of NS with canonical mass, like the one predicted by GW170817, is more in favor of a softer EoS. This issue turns out can be resolved by introducing anisotropic pressure [88]. However, the tension will remain tight if the secondary object in another GW event, i.e., GW190814, is a static or slow rotating NS.

## CHAPTER 5

### RELATIVISTIC MEAN FIELD

#### 5.1 Relativistic Mean Field

Since the second part of our work relies on EoS from Relativistic Mean Field (RMF) with G3 parameter, in this chapter we shall briefly revisit RMF to illustrate the main algorithm on how to obtain the needed EoS. The EoS is usually extracted as two columns of data: energy density and pressure. This data will then be the input in the code that calculates the TOV equation in form of the following. The data is fitted as a polynomial function of pressure and the fitting result is used as input in the TOV solver.

As a disclaimer, this chapter is by no means comprehensive. Interested readers are referred to other more comprehensive literature such as Ref. [48]. For more pedagogical ones, we refer to Refs. [89, 90].

In this work we actually use the Lagrangian from Ref. [91]. But to make this chapter as simple as possible, we consider the most simple model in RMF called the  $\sigma - \omega$  model, whose Lagrangian is

$$\mathcal{L} = \mathcal{L}_B^{\text{free}} + \mathcal{L}_M^{\text{free}} + \mathcal{L}_{BM}^{\text{lin}}. \quad (5.1)$$

This Lagrangian describes baryons interacting with each other through  $\sigma$  and  $\omega$  mesons and the mesons also are not self-interacting. The baryons considered here are the proton and neutron  $B = p, n$ . The free baryon term is

$$\mathcal{L}_B^{\text{free}} = \sum_{B=p,n} \bar{\psi}_B [i\gamma^\mu \partial_\mu - M_B] \psi_B. \quad (5.2)$$

The free meson term is

$$\mathcal{L}_M^{\text{free}} = \frac{1}{2} (\partial^\mu \sigma \partial_\mu \sigma - m_\sigma^2 \sigma^2) - \frac{1}{4} \omega^{\mu\nu} \omega_{\mu\nu} + \frac{1}{2} m_\omega^2 \omega^\mu \omega_\mu \quad (5.3)$$

The linear baryon-meson interaction term is

$$\mathcal{L}_{BM}^{\text{lin}} = \sum_B \bar{\psi}_B [g_{\sigma B} \sigma - \gamma_\mu g_{\omega B} \omega^\mu] \psi_B. \quad (5.4)$$

This Lagrangian will produce equations of motions that are too complicated to solve since they are partial differential equations. The RMF approximation uses the fact that the system is in the ground state and the following four assumptions are used in the system:

(1) translation invariance, (2) rotation invariance, (3) staticity, and (4) definite spin and parity. These conditions imply that the mesons all behave like constants:

$$\begin{aligned}\sigma(x) &\longrightarrow \langle\sigma(x)\rangle = \sigma_0, \\ \omega^\mu(x) &\longrightarrow \langle\omega^\mu(x)\rangle = \omega^\mu.\end{aligned}$$

Using the Euler-Lagrange equation on the Lagrangian and employing the RMF approximation, we obtain one equation of motion and three constraints

$$[i\gamma^\mu\partial_\mu - M_B + g_{\sigma B}\sigma_0 - \gamma_\mu g_{\omega B}\omega^\mu] \psi_B = 0, \quad (5.5)$$

$$-m_\sigma^2\sigma_0 + \sum_B g_{\sigma B} \langle \bar{\psi}_B \psi_B \rangle = 0, \quad (5.6)$$

$$m_\omega^2\omega_0 - \sum_B g_{\omega B} \langle \psi_B^\dagger \psi_B \rangle = 0, \quad (5.7)$$

$$m_\omega^2\omega_i - \sum_B g_{\omega B} \langle \bar{\psi}_B \gamma_i \psi_B \rangle = 0. \quad (5.8)$$

We also need the pressure  $p$  and energy density  $\epsilon$  using the canonical definition of the stress-energy tensor

$$T_\nu^\mu = \frac{\partial \mathcal{L}}{\partial(\partial_\mu \phi_a)} \partial_\nu \phi_a - \delta_\nu^\mu \mathcal{L}. \quad (5.9)$$

The energy density and the pressure are from  $\rho = T_0^0$  and  $p\delta_j^i = -T_j^i$ , respectively. Since we use the RMF approximation, the fields  $\phi_a$  are just  $\psi_B$  so we obtain

$$\epsilon = \sum_B \langle \bar{\psi}_B \gamma_0 e_B(\vec{k}) \psi_B \rangle - \langle \mathcal{L} \rangle, \quad (5.10)$$

$$p = \frac{1}{3} \sum_B \langle \bar{\psi}_B \vec{\gamma} \cdot \vec{k} \psi_B \rangle + \langle \mathcal{L} \rangle, \quad (5.11)$$

with

$$\langle \mathcal{L} \rangle = -\frac{1}{2} m_\sigma^2 \sigma_0^2 + \frac{1}{2} m_\sigma^2 (\omega_0^2 - \omega_i^2). \quad (5.12)$$

Since the mean field approximation makes the nucleon has no  $x$  dependent term, we have  $\psi$  in the form of

$$\psi_B(x) = \psi_B(k) e^{i\vec{k} \cdot \vec{x} - ie_B(\vec{k})t}. \quad (5.13)$$

Substitute this into Eq. (5.5) we obtain

$$[\gamma_0 e_B(\vec{k}) - \gamma_0 g_{\omega B} \omega_0] = [\vec{\gamma} \cdot (\vec{k} + g_{\omega B} \vec{\omega}) + M_B - g_{\sigma B} \sigma_0] \quad (5.14)$$

Multiplying this with  $\gamma_0$  from left and squaring both terms we have

$$e_B(\vec{k}) = g_{\omega B}\omega_0 \pm \sqrt{\left(\vec{k} + g_{\omega B}\vec{\omega}\right)^2 + (M_B - g_{\sigma B}\sigma_0)^2}. \quad (5.15)$$

We shall only use the positive sign in  $e_B(\vec{k})$  since we consider the system consists of particles only, excluding the anti-particles.

Now the three constraints Eqs. (5.6)-(5.8), energy density and pressure needs the explicit expressions for their expectation value terms. This can be done using a method deviced by Glendenning in Ref. [48], using

$$\langle \bar{\psi}_B \Gamma \psi_B \rangle = \sum_s \int \frac{d\vec{k}}{(2\pi)^3} (\bar{\psi}_B \Gamma \psi_B)_{\vec{k},s} \Theta[\mu_B - e_B(\vec{k})]. \quad (5.16)$$

$s$  is the (iso)-spin index,  $(\bar{\psi}_B \Gamma \psi_B)_{\vec{k},s}$  is the expectation value of its single-particle state,  $\mu_s$  is the Fermi energy or chemical potential, and  $\Theta$  is the step function. The operator  $\Gamma$  can be obtained by manipulation the so-called Dirac Hamiltonian

$$H_D = i\partial_0 = \gamma_0 \vec{\gamma} \cdot \left( \vec{k} + g_{\omega B}\vec{\omega} \right) + \gamma_0(M_B - g_{\sigma B}\sigma_0) + g_{\omega B}\omega_0. \quad (5.17)$$

Now it is clear that

$$(\bar{\psi}_B H_D \psi_B)_{\vec{k},B} = e_B(\vec{k}). \quad (5.18)$$

By convention,  $(\psi_B^\dagger \psi_B)_{\vec{k},B} = 1$ , so if  $\zeta$  is an arbitrary variable then

$$\frac{\partial}{\partial \zeta} (\psi_B^\dagger H_D \psi_B)_{\vec{k},B} = \left( \psi_B^\dagger \frac{\partial H_D}{\partial \zeta} \psi_B \right)_{\vec{k},B} = \frac{\partial e_B(\vec{k})}{\partial \zeta}. \quad (5.19)$$

So if  $\Gamma = \gamma_0 \gamma_i$  then we use  $\zeta = k^i$  so we have

$$\begin{aligned} \langle \psi_B^\dagger \gamma_0 \gamma_i \psi_B \rangle &= \sum_s \int \frac{dk^i dk^j dk^k}{(2\pi)^3} \frac{\partial}{\partial k^i} e_B(\vec{k}) \Theta[\mu_B - e_B(\vec{k})] \\ &= 2 \int \frac{dk^j dk^k}{(2\pi)^3} \int de_B(\vec{k}) = 0. \end{aligned} \quad (5.20)$$

This vanishes because  $e_B$  are constant anywhere on the boundary of the region where the integration is evaluated. This implies  $\omega_i = 0$ , so in the RMF approximation, we can use  $\omega^\mu(x) \rightarrow \langle \omega^\mu(x) \rangle = \omega_0 \eta^{0\mu}$  from the start, with  $\eta^{\mu\nu} = \text{diag}(1, -1, -1, -1)$ . The others

can be find to be

$$\rho_B = \langle \psi_B^\dagger \psi_B \rangle = 2 \int_0^{k_{FB}} \frac{d\vec{k}}{(2\pi)^3} = 2 \int_0^{k_{FB}} \frac{k^2 dk}{2\pi^2} = \frac{k_{FB}^3}{3\pi^2}, \quad (5.21)$$

$$\langle \bar{\psi}_B \psi_B \rangle = 2 \int_0^{k_{FB}} \frac{k^2 dk}{2\pi^2} \frac{m^*}{\sqrt{k^2 + m^{*2}}}, \quad (5.22)$$

which can be substituted to Eqs. (5.6)-(5.7), and, in the energy density and pressure,

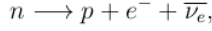
$$\langle \bar{\psi}_B \gamma_0 e_B(\vec{k}) \psi_B \rangle = g_{\omega B} \omega_0 \rho_B + 2 \int_0^{k_{FB}} \frac{k^2 dk}{2\pi^2} \sqrt{k^2 + m^{*2}}, \quad (5.23)$$

$$\langle \bar{\psi}_B \vec{\gamma} \cdot \vec{k} \psi_B \rangle = 2 \int_0^{k_{FB}} \frac{k^2 dk}{2\pi^2} \frac{k^2}{\sqrt{k^2 + m^{*2}}}. \quad (5.24)$$

The baryon density  $\rho$  is defined as

$$\rho = \rho_n + \rho_p. \quad (5.25)$$

Three stability conditions are necessary for massive bodies such as NS. It is known that there is the beta decay process



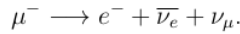
but since the large density of a nucleus can trigger another reaction, namely



These two reaction compete each other creating the so-called beta-stability condition

$$\mu_n = \mu_p + \mu_e, \quad (5.26)$$

with  $\mu_x = \partial \epsilon / \partial \rho_x$  and  $\rho_x = k_x^3 / (3\pi^2)$ . For ultra-dense matter, electrons can have ultra-relativistic energies reaching the mass of muon, changing the electrons into muons by



So the other condition is

$$\mu_\mu = \mu_e. \quad (5.27)$$

The last condition came from the fact that massive bodies is electrically neutral, so

$$\rho_\mu + \rho_e = \rho_p. \quad (5.28)$$

One can numerically obtain the pressure and the energy density, which will be used as the EoS. They also satisfy the relation from thermodynamics

$$p = \rho^2 \frac{\partial}{\partial \rho} \frac{\epsilon}{\rho}. \quad (5.29)$$

Various quantities can be calculated from these equations. But here we only mention the most popular ones. The first one is the symmetry energy coefficient

$$E_{\text{sym}} = \frac{1}{2} \frac{\partial^2}{\partial \delta^2} \left. \frac{\epsilon}{\rho} \right|_{\delta=0}, \quad (5.30)$$

where  $\delta = (\rho_n - \rho_p)/\rho$  is measuring the deviation from the assumed isospin symmetry. In the semi-empirical mass formula,  $E_{\text{sym}} = a_4$  which accompany the  $(N - Z)^2/A^2$  term. To evaluate this, usually one use these relations:

$$\rho_n = \rho \frac{1 + \delta}{2}, \quad (5.31)$$

$$\rho_p = \rho \frac{1 - \delta}{2}. \quad (5.32)$$

The second quantity is the compressibility

$$K = 9\rho_s^2 \frac{\partial^2}{\partial \rho^2} \left. \frac{\epsilon}{\rho} \right|_{\rho=\rho_0}, \quad (5.33)$$

where  $\rho_0$  is the so-called saturation density. The origin of  $\rho_0$  is as follows. Since nuclear matter is a saturated system, we know that the strong force keep the nucleons clump together opposing the Coulomb force. This strong force is attractive at radius  $> 0.4$  fm but become repulsive at radius  $\leq 0.4$  fm. Thus the density has a maximum value and this is called saturation density. The value of  $\rho_0$  differ from a literature to the other, depending on the underlying theories and experiments:  $\rho_0 = 0.148 \text{ fm}^{-2}$  from Ref. [90],  $\rho_0 = 0.153 \text{ fm}^{-2}$  from Ref. [48], and  $\rho_0 = 0.16 \text{ fm}^{-2}$  from Ref. [49].

The last quantity is the binding energy, defined as [49]

$$\frac{E}{A} = \frac{1}{\rho} \left( \epsilon - \sum_B M_B \rho_B \right). \quad (5.34)$$

By comparing with data from observations, one usually shows both the calculation results and the observation data in a plot where  $E/A$  and  $\rho/\rho_0$  are the  $y$  and  $x$ -axis, respectively.

20

## 5.2 The Neutron Star Matter's Equation of State

The following is taken from our second draft paper which is still in process of submission.

Here, we discuss a summary of the RMF model that we use in Chapter 7. We also discuss the nuclear and NS matter predictions, which corresponds to the RMF model after a parameter set is used. Specifically, we show the reason why we use the G3 RMF parameter set to describe the core region of NSs.

We start by using the RMF Lagrangian density from Ref. [92]. The Lagrangian density includes  $\sigma$ ,  $\omega$ , and  $\rho$  as the non-strange mesons,  $\phi$  as the strange meson,  $e^-$  and  $\mu^-$  as the leptons,  $p$  and  $n$  as the nucleons, and  $\Lambda$ ,  $\Sigma$ ,  $\Xi$  as the hyperons. The tensors  $\omega^{\mu\nu} = \partial^\mu\omega^\nu - \partial^\nu\omega^\mu$ ,  $\phi^{\mu\nu} = \partial^\mu\phi^\nu - \partial^\nu\phi^\mu$  and  $\rho^{\mu\nu} = \partial^\mu\rho^\nu - \partial^\nu\rho^\mu$  corresponds to  $\omega$ ,  $\phi$  and  $\rho$  mesons, respectively. The explicit expressions is as follows:

$$\mathcal{L} = \mathcal{L}_B + \mathcal{L}_{BM} + \mathcal{L}_M + \mathcal{L}_L, \quad (5.35)$$

where the free lepton term with lepton mass  $M_L$  ( $L = e^-, \mu^-$ ) is

$$\mathcal{L}_L = \sum_L \bar{\Psi}_L [i\gamma^\mu \partial_\mu - M_L] \Psi_L, \quad (5.36)$$

the free baryon term with baryon mass  $M_B$  ( $B = N, \Lambda, \Sigma, \Xi$  with  $N = p, n$ ) is

$$\mathcal{L}_B = \sum_B \bar{\Psi}_B [i\gamma^\mu \partial_\mu - M_B] \Psi_B, \quad (5.37)$$

the meson-baryon coupling terms are

$$\begin{aligned} \mathcal{L}_{BM} &= \sum_B \bar{\Psi}_B [g_{\sigma B} \sigma - \gamma_\mu g_{\omega B} \omega^\mu \\ &\quad - \frac{1}{2} \gamma_\mu g_{\rho B} \boldsymbol{\tau}_B \cdot \boldsymbol{\rho}^\mu - \gamma_\mu g_{\phi B} \phi^\mu] \Psi_B, \end{aligned} \quad (5.38)$$

the free and self interaction meson Lagrangian density

$$\begin{aligned} \mathcal{L}_M &= \frac{1}{2} (\partial_\mu \sigma \partial^\mu \sigma - m_\sigma^2 \sigma^2) + \frac{1}{2} (\partial_\mu \sigma^* \partial^\mu \sigma^* - m_{\sigma^*}^2 \sigma^{*2}) \\ &\quad - \frac{1}{4} \omega_{\mu\nu} \omega^{\mu\nu} + \frac{1}{2} m_\omega^2 \omega_\mu \omega^\mu - \frac{1}{4} \phi_{\mu\nu} \phi^{\mu\nu} + \frac{1}{2} m_\phi^2 \phi_\mu \phi^\mu \\ &\quad - \frac{1}{4} \boldsymbol{\rho}_{\mu\nu} \cdot \boldsymbol{\rho}^{\mu\nu} + \frac{1}{2} m_\rho^2 \boldsymbol{\rho}_\mu \cdot \boldsymbol{\rho}^\mu + \mathcal{L}_M^{NL}, \end{aligned} \quad (5.39)$$

with the nonlinear terms the contain meson self interactions are

$$\begin{aligned}
 \mathcal{L}_M^{NL} = & -\frac{\kappa_3 g_{\sigma N} m_\sigma^2}{6m_N} \sigma^3 - \frac{\kappa_4 g_{\sigma N}^2 m_\sigma^2}{24m_N^2} \sigma^4 + \frac{\zeta_0 g_{\omega N}^2}{24} (\omega_\mu \omega^\mu)^2 \\
 & + \frac{\eta_1 g_{\sigma N} m_\omega^2}{2m_N} \sigma \omega_\mu \omega^\mu + \frac{\eta_2 g_{\sigma N}^2 m_\omega^2}{4m_N^2} \sigma^2 \omega_\mu \omega^\mu \\
 & + \frac{\eta_\rho g_{\sigma N} m_\rho^2}{2m_N} \sigma \boldsymbol{\rho}_\mu \cdot \boldsymbol{\rho}^\mu + \frac{\eta_{1\rho} g_{\sigma N}^2 m_\rho^2}{4m_N^2} \sigma^2 \boldsymbol{\rho}_\mu \cdot \boldsymbol{\rho}^\mu \\
 & + \frac{\eta_{2\rho} g_{\omega N}^2 m_\rho^2}{4m_N^2} \omega_\mu \omega^\mu \boldsymbol{\rho}_\nu \cdot \boldsymbol{\rho}^\nu.
 \end{aligned} \tag{5.40}$$

The mesons are coupled to baryons in Eq. (5.38) and coupled to themselves in Eq. (5.39). In Eq. (5.40), it includes the RMF nonlinear  $\sigma$  and  $\omega$  mesons self-interaction and cross interactions between  $\sigma$ ,  $\omega$ , and  $\rho$  mesons. In the RMF models,  $g_{\sigma B}$ ,  $\kappa_3$ ,  $\eta_1$ , etc. are coupling constants and parameters of the model. They are determined numerically by fitting the model's predictions to experimental data from nuclear matter and finite nuclei. The obtained values from the fitting process depend on the observables and their weights. The RMF parameter sets are sets of these explicit values. In this work, we use the RMF parameter sets whose values can be seen in Refs.[34, 92, 93, 94].

The investigations regarding the contribution of the nucleon sector in EoS are well-established because, in this sector, the RMF parameter constraints are relatively tight. The binding energies and EoS, i.e., pressure as a function of the ratio of nucleon density over saturation density, in the cases of symmetric nuclear matter (SNM) and pure neutron matter (PNM) are shown in Figs. 5.1 and 5.2. These are from employing parameters sets called G3 [34], BSP [88, 92, 91], TM1e [93], and FSUH [94]. The curves from these parameter sets are compared to the results from experimental data [95, 96] and the predictions from the chiral effective field theory [97, 98]. In general, all parameter sets are quite compatible with the experimental data, but we note that the results at low densities from G3 are more compatible with the chiral effective field theory calculations than other parameter sets. Hence in this work, we use the G3 parameter set to study the NS properties.

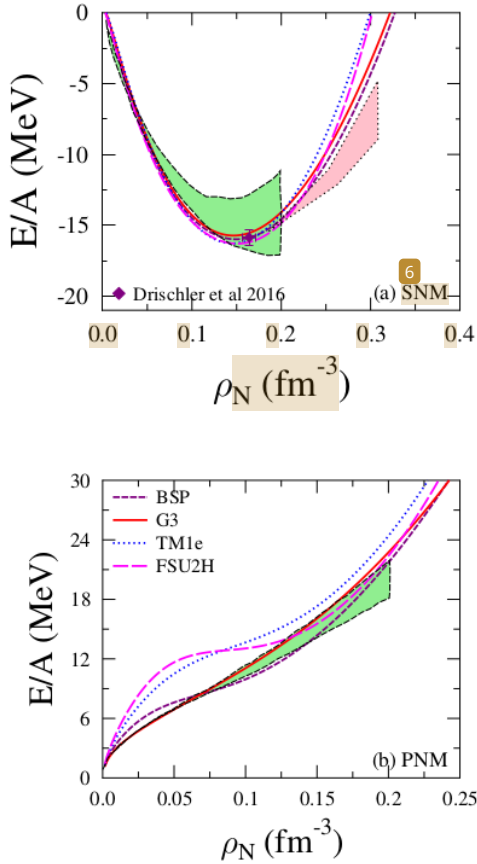


**Figure 5.1:** Here, we show the binding energy on SNM (a) and PNM (b) cases from G3, BSP, TM1e, and FSU2H MF parameter sets. The light green shaded area is from chiral effective theory [97], while the pink shaded area is a constraint imposed by the SNM binding energy, which is extracted from FOPI experimental data [95]. In addition, the SNM binding energy at saturation value from Refs. [97] is also shown with a purple diamond.

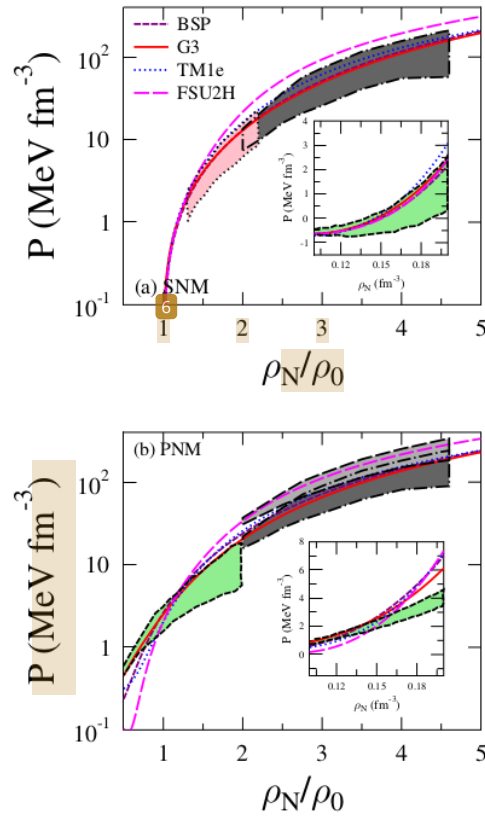


**Figure 5.2:** Here, the EoS is shown as the pressure as a function of the ratio nucleon density to saturation density ( $\rho_N/\rho_0$ ) in the cases of SNM and PNM, which are shown in panels (a) and (b) respectively. The curves are calculated using G3, BSP, TM1e, and FSU2H parameter sets. The gray shaded areas are extracted from the heavy-ion experimental data [96]. The pink shaded area in (a) is extracted from the FOPI [95] experimental data [95]. The green shaded areas in panels (a) and (b) are the theoretical binding energy at low densities in the case of PNM, which is obtained from the chiral effective field theory calculations [97, 98].

It is a known fact that the hyperons and other exotic particles' coupling constants are experimentally difficult to constrain. Therefore, the contribution of the hyperons sector in the EoS is uncertain. On the other hand, when hyperons and other exotic particles are included, they tend to soften the EoS in the NS core. Hence, the corresponding maximum mass is always smaller than the one obtained without hyperons and other exotics. (For the related discussions on hyperon puzzle, please see, e.g, Ref. [94] and the references

therein.) Here, following Ref. [94], we take SU(3) prescription and potential depths' experimental value at the saturation density to determine the hyperon coupling constants, while neglecting the contribution from other exotics. Why we do this is that SU(3) prescription produces a stiffer EoS relative to the one from SU(6) [88].

We use the inner and outer crust EoSs based on the Hartree-Fock Thomas-Fermi model following Miyatsu *et al.* [99] to describe the NS's crusts. The drawback of this method is that there is an uncertainty that should be paid attention to. (For the detailed discussion about it, please see Ref. [88] and the references therein.)

The  $\beta$ -stability is assumed to happen in the NS matter. Hence, the charge neutrality from lepton and baryon charges, the baryon density conservation, and the potential chemical balancing can be used to determine the compositions of the mesons, baryons, and leptons in an NS. Here, to generate the EoSs, we also use another constrain from restricting the speed of sound at high densities  $v_s \leq c/\sqrt{3}$ , with  $c$  is the speed of light. (To see the recent progress of speed of sound constraints on NS discussions, please see Ref. [100] and the references therein.)

In Fig. 5.3, we show the EoSs and their speed of sound from matter without hyperon (G3 WoutH), with hyperon (G3 WH), and with the constraint for the speed of sound (G3 WoutHSS and G3 WHSS). In correspond to that, in Fig. 5.4, we show the mass-radius (M-R) curves from TOV GR. From Fig. 5.3, we observe that G3 WoutH is more compatible with the recent EoS constraints [80, 57, 58], and the stiffness of the corresponding EoSs is increased by the speed of sound's restriction. However, the effect for all G3 WoutHSS, WHSS, WoutH, and WH are insufficient to reach the constraint from GW170817 at high densities.

In Fig. 5.4, we can see the impacts of the hyperons and the speed of sound's constraint on M-R curves within TOV GR. All maximum masses from each EoS are in agreement with radius constraints for their NS with canonical mass ( $1.4 M_\odot$ ) from Refs [57, 58]. However, hyperons' contribution on G3 WH EoS lowers the NS maximum mass significantly below the mass constraint of  $2.0 M_\odot$ . It can be seen that using the speed of sound requirement (G3 WHSS) increases the NS maximum mass. However, it is still less than the mass constraints from  $2.0 M_\odot$  pulsars.

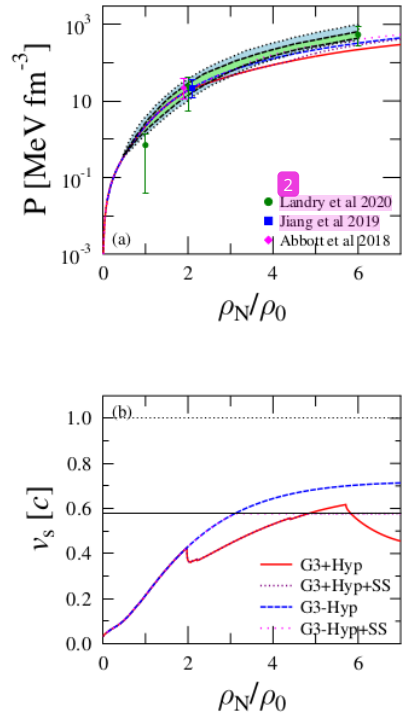


**Figure 5.3:** These EoSs are calculated using the G3 parameter set. The EoS without and with hyperon is denoted here by G3-Hyp and G3+Hyp, respectively. “+SS” denotes the use of the speed of sound’s constraint ( $v_s \leq c/\sqrt{3}$ ). In panel (a), pressure is shown as a function of the ratio of  $\rho_N$  to  $\rho_0$ . In panel (b), the speed of sound is shown as the function of  $\rho_N$  to  $\rho_0$ . For comparison, some data are given as follow: the light blue and light green shaded area are from GW170817 [80], the data points for particular densities are taken from GW170817 [80], a recent non-parametric analysis [57], and the joint of PSR J0030+0451, GW170817, and the nuclear data analysis [58].

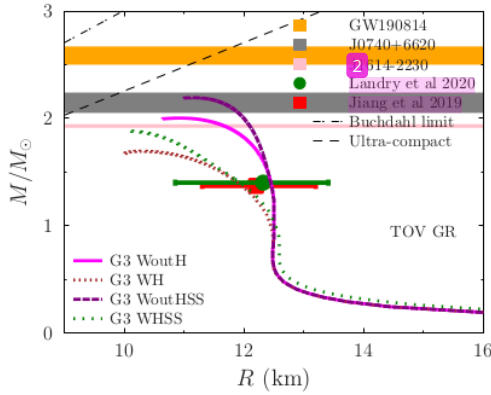


**Figure 5.4:** The M-R curves are calculated using the TOV GR framework. These are from using the G3 parameter set without hyperon (WoutH), with hyperon (WH), and the ones with additional speed of sound constraint (WoutHSS and WHSS). They are compared with the data from the GW190814 event [6], Landry *et al.* 2020 [57], and Jiang *et al.* 2019 [58]. We also show the results PSR J1614-2230 analysis [71, 72, 73] and PSR J0740+6620 analysis [73, 7]. The ultra-compact limit and Buchdahl limit lines are also shown.

Now, if the  $2.6 M_\odot$  secondary object detected in GW190814 is a non-rotating NS, then, at least in GR theory, it has another EoS than ours here. This is because all the maximum masses predicted by all EoSs used in this work are less than  $2.6 M_\odot$ . Recent investigations [8, 61] shown that the  $2.6 M_\odot$  constraint and the canonical  $1.4 M_\odot$  NS radius constraints can be simultaneously satisfied using particular Big Apple RMF EoS if the hyperons are excluded in the NS matter. This Big Apple EoS is also compatible with finite nuclei and nuclear matter constraints, but it is not compatible with ones from heavy-ion collision constraints [96]. Hence, the author of Ref. [8] concluded that the  $2.6 M_\odot$  secondary object is unlikely to be an NS within GR.

To this end, it is worth mentioning that EiBI, with acceptable EoS, can have NS maximum larger than  $2 M_\odot$  without reaching the Buchdahl limit [33]. However, the radius also increases. Therefore in Chapter 7, we will systematically investigate, within the EiBI theory, the tension between the relatively small recent radius and the considerably high maximum mass constraints.

## CHAPTER 6

### ULTRA-COMPACT OBJECT FROM SEMI-CLASSICAL GRAVITY

In this chapter, we present the first part of our work. The following passage is from our paper published in Ref. [101].

#### 6.1 A Short Introduction to The Semi-classical Gravity

Semi-classical gravity is one of the earliest investigations to reconcile quantum field theory and GR. It began with the discovery of the BH entropy, BH temperature, and Unruh effect (see monograph [45] and [46]). In this theory, the vacuum in a general space-time is generally different from the usual one in Minkowski space-time. It is caused by the Bogolyubov transformation, which says that a vacuum state in the coordinate system  $X^\mu$  is different from another vacuum state in another coordinate system  $x^\mu$  though the two coordinate systems are related by a coordinate transformation  $x^\mu \rightarrow X^\mu(x^\alpha)$ . This problem can be solved because it turns out that the stress tensor is indifferent to one's choice of coordinate system. Even though there are infinities inside the components of the stress tensor, people had identified which physical infinities, whose result is the Hadamard vacuum state. The Hadamard vacuum is a quantum state whose infinities in the two-point function are the same as the infinities from the one in Minkowskian space-time. Another state exists, e.g., the Unruh vacuum, which describes the vacuum around a Schwarzschild BH. This is the reason why people usually use the Unruh state to study the formation of a BH. The studies of  $n$ -point functions are related to regularization of these infinities in the stress tensor's expectation value ( $\langle \hat{T}_{\mu\nu} \rangle$ ). Hence, the matter part in the EFE is quantum but the geometrical part is still classic

$$G_{\mu\nu} = 8\pi G \langle \hat{T}_{\mu\nu} \rangle.$$

For it to be physical, the stress tensor's expectation value should satisfy Wald's renormalization axioms (see page 89 of [47]).

It is known that the renormalization methods can only be applied in some specific cases [102]. In conformal field theory, these methods give rise to an anomaly called the trace anomaly [45]. This anomaly is still unsolvable. The role of the cosmological constant is also nontrivial [103], hence in this theory, one cannot treat this constant as a

free parameter.

Since we shall investigate the Boulware vacuum in the next sections, we shall briefly discuss this and compare it to the Unruh vacuum. The Boulware vacuum is a quantum state of the exterior of any massive body and it is singular at the horizon. The Unruh vacuum is the quantum state of a gravitational collapse and at large distances, it features Hawking radiation [104, 105]. In general, these two vacuums are inequivalent. A detailed discussion about the relationship between both vacuums can be seen in Ref. [106]. A study had investigated the dynamical evolution of a collapsed star within semi-classical gravity [107]. It found that in some cases, the trapping horizon is not formed and new collapsed horizonless objects could exist. Since these objects have no horizon, there is no confrontation between the information paradox and the run-away endpoint problem. It also found that both vacuums can locally describe the same exterior region as long as there is no horizon. If the horizon exists, then the Boulware vacuum is no longer valid and the Unruh vacuum is used instead. Please see the technical details of this matter in Ref. [107]. Another study by Ho and Matsuo [108] has shown that if a compact object has no singularity nor horizons, then its exterior can be described by the Boulware vacuum as long as it is in a stationary state. Furthermore, Ho and Matsuo have shown by nonperturbative analysis of the semiclassical Einstein equation in another paper [109] that it is possible to consider the Boulware vacuum for any compact object. These results [108, 109] is in contrast to the common view that Boulware vacuum becomes unphysical if the compact object's radius is smaller than the Schwarzschild radius since the stress tensor is divergent at the Schwarzschild radius. In this work, we study the horizonless compact object in semi-classical gravity and its radius is larger than the Schwarzschild radius. Therefore, choosing a Boulware vacuum is relatively safe.

Recently, Carballo-Rubio [5] proposed a new type of TOV-like equation from semi-classical gravity theory. The solutions obey the usual boundary conditions, i.e., zero pressure at the surface of the star. They arise from one of two possible pressure equations  $p'(r)$ . One of them has a negative sign which corresponds to the usual TOV equation at a weak limit and the other has a positive sign which is identified as a nontrivial combination of the black stars and gravastars. This calculation is done by defining a relation between pressure  $p$ , mass  $m$ , and energy density  $\rho$  by a constant  $\lambda > 1$ . This trick makes the EoS unique. The pressure equation  $p'$  with the negative sign had been analyzed by Ho and Matsuo [108]. They show that by using constant energy density and without making the pressure goes to infinity, the Buchdahl limit can be violated.

In this work, we study much further the pressure equation  $p'$  with the negative sign. The writing is organized as follows. In Section 6.2, we revisit the models (Refs. [5] and [108]) briefly, while the numerical schemes is discussed in length in Appendix A.

This is crucial to justify our results in the following sections since both Refs. [5] and [108] use integration from surface to center (denoted as backward integration), whereas we do the opposite (denoted as forward integration). In Section 6.3, we study the model given the assumption of non-negative pressure and energy density, and we employ a simple linear EoS. We then look at the deviation from the case of TOV in GR. In Section 6.4 part B, the numerical results are discussed. Finally in Section 6.6, our work is summarized.

## 6.2 Theory of a Compact Star in Semi-classical Gravity

In this section, we follow Ref. [5]. We start by using the renormalized stress-energy tensor (RSET) in the following modified EFE

$$G_{\mu\nu} = \frac{8\pi G}{c^4} T_{\mu\nu} + 96\pi^2 l_p^2 \langle \hat{T}_{\mu\nu} \rangle, \quad (6.1)$$

where the constant  $l_p$  is the *renormalized Planck length* describing the quantum vacuum polarization of  $N \gg 1$  matter fields. This constant is related to the Planck length  $L_{\text{Pl}} = \sqrt{\hbar G/c^3}$  by the following relation:

$$l_p = \sqrt{\frac{N}{12\pi}} L_{\text{Pl}}.$$

From now, we shall use the natural units convention ( $c = 1$ ) and the constant  $l_p$  is treated as an arbitrarily adjustable constant.

To explain where the new term came from, we see the modified EFE above in its original form

$$G^{\mu\nu} = \frac{8\pi G}{c^4} \left( T_{\mu\nu} + \hbar c N \langle \hat{T}_{\mu\nu} \rangle \right) + \mathcal{H}_{\mu\nu}.$$

These new terms came from two possible theories, i.e.,

1. from  $\mathcal{O}(1/N)$  contributions with respect to the term proportional to  $\hbar N \langle \hat{T}_{\mu\nu} \rangle$ , which might be related to more loops in the Feynman diagrams, or
2. from adding  $\hbar^{n-1} G^{n-2} \mathcal{R}^n (n \geq 2)$  in the Einstein-Hilbert Lagrangian, where  $\mathcal{R}$  some kind of curvature scalars, e.g.,  $R_{\mu\nu} g^{\mu\nu}$ ,  $R_{\mu\nu} R^{\mu\nu}$ , and  $R_{\mu\nu\alpha\beta} R^{\mu\nu\alpha\beta}$ .

This is valid if the curvature remains small enough. We also ignore  $\mathcal{H}_{\mu\nu}$  because we think the leading term  $\langle T_{\mu\nu} \rangle$  is already small and thus  $\mathcal{H}_{\mu\nu}$  should be smaller. Carballo-Rubio had proven that  $\mathcal{H}_{\mu\nu} = 0$  is justified.

Next we use a similar scheme to derive the usual TOV equation, starting with the static

and spherically symmetric space-time

$$ds^2 = g_{\mu\nu} dx^\mu dx^\nu = ds_{(2)}^2 + r^2(d\theta^2 + \sin^2\theta d\varphi^2), \quad (6.2)$$

$$ds_{(2)}^2 = -e^{\nu(r)}dt^2 + \frac{dr^2}{1 - 2Gm(r)/r}. \quad (6.3)$$

This metric has a time symmetry so it has a timelike Killing vector  $\xi^\mu = \delta_t^\mu$ . Next, we use a perfect fluid with isotropic pressure as the stress tensor

$$T^{\mu\nu} = \boxed{13} (\rho + p)u^\mu u^\nu + pg^{\mu\nu}, \quad (6.4)$$

with  $u^\mu$  is the normalized and timelike 4-velocity of the fluid ( $u^\mu u_\mu = -1$ ). It is usual to choose the fluid to be standing still, i.e., only  $u^0$  is nonzero.  $g^{\mu\nu}$  is the inverse of the metric. The RSET is calculated using the  $s$ -wave Polyakov approximation (see Ref. [110] page 216)

$$\langle \hat{T}_{\mu\nu} \rangle = \frac{\delta_\mu^a \delta_\nu^b}{4\pi r^2} \langle \hat{T}_{ab}^{(2)} \rangle. \quad (6.5)$$

The  $a$  and  $b$  indices denote the coordinates in  $ds_{(2)}^2$ . The other tensor  $\langle \hat{T}_{ab}^{(2)} \rangle = \langle 0 | \hat{T}_{ab}^{(2)} | 0 \rangle$  is calculated in a space-time with metric  $ds_{(2)}^2$ . In this model, we use the Boulware vacuum state  $|0\rangle$ , which is associated with the Killing vector mentioned before. The Killing covector is then just  $\xi_\mu = -e^\nu \delta_{\mu t}$ .

To obtain  $\langle \hat{T}_{ab}^{(2)} \rangle$ , people use null coordinate  $(u, r)$ , calculate  $\langle \hat{T}_{ab}^{(2)} \rangle$ , and then transform back to  $(t, r)$  coordinate. On the other hand, it was shown in Ref. [111] that we can use a shortcut, which is still equivalent to the usual method. This shortcut is

$$\langle \hat{T}_{ab}^{(2)} \rangle = \frac{1}{48\pi} \left( R^{(2)} g_{ab} + A_{ab} - \frac{1}{2} g_{ab} A \right), \quad (6.6)$$

<sup>26</sup> where  $R^{(2)}$  is the Ricci scalar from metric  $ds_{(2)}^2$ , and

$$A_{ab} = \frac{4}{|\xi|} \nabla_a \nabla_b |\xi|, \quad (6.7)$$

with  $|\xi| = e^{\nu/2}$ . Then from  $\nabla_\mu T^{\mu\nu} = 0$  and Eq. (6.1), one obtain (with  $f' = df/dr$ )

$$-p' - \frac{(p + \rho)}{2}\nu' = 0, \quad (6.8)$$

$$\frac{\nu'}{r} - \frac{2Gm}{r^3(1 - 2Gm/r)} = \frac{8\pi Gp}{1 - 2Gm/r} - \frac{l_p^2}{4} \left(\frac{\nu'}{r}\right)^2, \quad (6.9)$$

$$\begin{aligned} \frac{2Gm'}{r^2} &= 8\pi G\rho + \frac{l_p^2}{r^2} \left[ \left(1 - \frac{2Gm}{r}\right) (\nu'' + (\nu')^2) \right. \\ &\quad \left. - \left(\frac{Gm'}{r} - \frac{Gm}{r^2}\right) \nu' - \frac{3}{4} \left(1 - \frac{2Gm}{r}\right) (\nu')^2 \right]. \end{aligned} \quad (6.10)$$

Equation  $\nabla_\mu T^{\mu\nu} = 0$  is valid because according to the Wald's axioms (see Ref. [47]), one of the axioms is the contracted Bianchi identity  $\nabla_\mu \langle \hat{T}^{\mu\nu} \rangle = 0$ . One can prove that this axiom is satisfied by directly substituting the RSET with its explicit components.

The reason why  $\nabla_\mu \langle T^{\mu\nu} \rangle = 0$  should be satisfied is due to the mathematical consequence of Eq. (6.1), i.e.,

$$\nabla_\mu G^{\mu\nu} = \frac{8\pi G}{c^4} \left( \nabla_\mu T^{\mu\nu} + \hbar c N \nabla_\mu \langle \hat{T}^{\mu\nu} \rangle \right).$$

The left-hand side goes to zero because of the contracted Bianchi identity. The right-hand side should also be zero. It is also common practice to use conservation equation  $\nabla_\mu T^{\mu\nu} = 0$  so the rest should be zero.

From Eq. (6.9), there are two roots:

$$\nu' = -\frac{2r}{l_p^2} \left( 1 \pm \sqrt{1 + \frac{l_p^2}{r^2} \frac{2Gm}{r} \frac{(1 + 4\pi r^3 p/m)}{(1 - 2Gm/r)}} \right). \quad (6.11)$$

These roots lead to two different expressions for both  $p'$  and  $m'$ . The negative (positive, resp.) signs on the right-hand side will be named as *negative (positive)* branches. In  $l_p \rightarrow 0$  limit, the negative branch becomes the TOV equation in GR while the positive branch does not. Next, we focus on this negative branch in the rest of this chapter.

### 6.3 Analysing the Negative Branch

The following passage is our argument why we choose the negative branch. We study the negative branch from the model given the non-negative pressure  $p$  and energy density  $\rho$  assumption. Here we define

$$X = \frac{2Gm}{r} \frac{(1 + 4\pi r^3 p/m)}{(1 - 2Gm/r)}, \quad (6.12)$$

for simplicity. Then, we have

$$p' = \frac{(p + \rho)r}{l_P^2} \left( 1 + k \sqrt{1 + \frac{l_p^2}{r^2} X} \right) \quad (6.13)$$

where  $k = \pm 1$  is used to contain the positive-negative sign. We investigate this equation in three cases: (a)  $\frac{l_p^2}{r^2} X < 1$ , (b)  $\frac{l_p^2}{r^2} X > 1$  and (c)  $\frac{l_p^2}{r^2} X = 1$ . Notice that  $X > 0$  because  $2Gm/r < 1$ .

Consider the case (a). Using binomial expansion with respect to small  $\frac{l_p^2}{r^2} X$ , and calculating to only the first leading order, we obtain

$$p' = \begin{cases} \frac{\rho+p}{8r^2} \left( \frac{4r}{l_p^2 X} + \frac{X}{r} \right), & k = +1, \\ -\frac{\rho+p}{2} \frac{X}{r}, & k = -1. \end{cases} \quad (6.14)$$

Because of the nonzero pressure at the star's center and the pressure goes to zero at the surface at  $r = R$ , we need  $p' < 0$ , at least in some parts in the domain  $0 < r < R$ . This is satisfied by  $k = -1$  but not by  $k = +1$ . Notice that when  $k = -1$ , it is just the TOV equation. Next consider the case (b). Using binomial expansion again, this leads to

$$p' = k \frac{(\rho + p)\sqrt{X}}{l_p}. \quad (6.15)$$

The condition  $p' < 0$  then eliminates  $k = +1$ . Lastly, consider the case (c). The binomial expansion then leads us to

$$p' = \frac{(p + \rho)r}{l_P^2} \left( 1 + k\sqrt{2} \right). \quad (6.16)$$

Again from the condition  $p' < 0$ , we should choose  $k = -1$ . Hence from all the three cases above, we only use the negative branch so that the boundary conditions  $p(0) = p_c > 0$  and  $p(R) = 0$  are satisfied.

Now we investigate Eq. (6.10). It is clear that  $m'$  is located on both left and right hand side. Our choice

$$p' = \frac{(p + \rho)r}{l_P^2} \left( 1 - \sqrt{1 + \frac{l_p^2}{r^2} X} \right), \quad (6.17)$$

then gives us the following

$$m' = 4\pi\rho r^2 \left( \frac{1 + \sum_{i=1}^7 A_i}{1 + \sum_{i=1}^4 B_i} \right). \quad (6.18)$$

The terms in the numerator inside the round bracket are

$$A_1 = \frac{3l_p^2 p}{\rho r^2 \sqrt{1 + \frac{l_p^2}{r^2} X}}, \quad (6.19)$$

$$A_2 = -\frac{3l_p^2 m(1 + 4\pi r^3 p/m)}{4\pi \rho r^5 \sqrt{1 + \frac{l_p^2}{r^2} X}}, \quad (6.20)$$

$$A_3 = -\frac{Gl_p^2 m^2 (1 + 4\pi r^3 p/m)}{2\pi \rho r^6 (1 - 2Gm/r) \sqrt{1 + \frac{l_p^2}{r^2} X}}, \quad (6.21)$$

$$A_4 = -\frac{m \left( 1 - \sqrt{1 + \frac{l_p^2}{r^2} X} \right)}{4\pi \rho r^3}, \quad (6.22)$$

$$A_5 = -\frac{(1 - 2Gm/r) \left( 1 - \sqrt{1 + \frac{l_p^2}{r^2} X} \right)}{4\pi G \rho r^2}, \quad (6.23)$$

$$A_6 = \frac{(1 - 2Gm/r) \left( 1 - \sqrt{1 + \frac{l_p^2}{r^2} X} \right)^2}{8\pi G \rho l_p^2}, \quad (6.24)$$

$$A_7 = \frac{l_p^2}{\rho r \sqrt{1 + \frac{l_p^2}{r^2} X}} p'. \quad (6.25)$$

The terms in the denominator inside the round bracket are

$$B_1 = \frac{4\pi l_p^2 p r}{m \sqrt{1 + \frac{l_p^2}{r^2} X}}, \quad (6.26)$$

$$B_2 = -\frac{l_p^2 (1 + 4\pi r^3 p/m)}{r^2 \sqrt{1 + \frac{l_p^2}{r^2} X}}, \quad (6.27)$$

$$B_3 = -\frac{2Gl_p^2 m (1 + 4\pi r^3 p/m)}{r^3 (1 - 2Gm/r) \sqrt{1 + \frac{l_p^2}{r^2} X}}, \quad (6.28)$$

$$B_4 = -\left( 1 - \sqrt{1 + \frac{l_p^2}{r^2} X} \right). \quad (6.29)$$

$m'$  is lengthy and complicated. But it is common to use the boundary conditions  $m(0) = 0$  and  $m(R) = M > 0$ , so that  $m' > 0$ . Hence, we need to be careful on fixing the constants and the data of both pressure and mass near the center.

Before integrating numerically, let us investigate both  $p'$  and  $m'$  at the limit  $l_p \rightarrow 0$ . If

Universitas Indonesia

we Taylor expand  $p'$  with respect to small  $l_p$ , we obtain

$$p' = -\frac{G(m + 4\pi r^3 p)(\rho + p)}{r(r - 2Gm)} + \frac{G^2 l_p^2 (m + 4\pi r^3 p)^2 (\rho + p)}{2r^3 (r - 2Gm)^2} + \mathcal{O}(l_p^3). \quad (6.30)$$

If we Taylor expand  $A_i$  and  $B_i$  with respect to small  $l_p$ , we obtain

$$A_1 = \frac{l_p^2 3p}{r^2 \rho} + \mathcal{O}(l_p^3) > 0, \quad (6.31)$$

$$A_2 = -\frac{l_p^2 3m(1 + 4\pi r^3 p/m)}{r^2 4\pi r^3 \rho} + \mathcal{O}(l_p^3) < 0, \quad (6.32)$$

$$A_3 = -\frac{l_p^2 Gm^2 (1 + 4\pi r^3 p/m)}{r^2 2\pi r^4 \rho (1 - 2Gm/r)} + \mathcal{O}(l_p^3) < 0, \quad (6.33)$$

$$A_4 = \frac{l_p^2 Gm^2 (1 + 4\pi r^3 p/m)}{r^2 4\pi r^4 \rho (1 - 2Gm/r)} + \mathcal{O}(l_p^3) > 0, \quad (6.34)$$

$$A_5 = \frac{l_p^2 m (1 + 4\pi r^3 p/m)}{r^2 4\pi r^3 \rho} + \mathcal{O}(l_p^3) > 0, \quad (6.35)$$

$$A_6 = \frac{l_p^2 Gm^2 (1 + 4\pi r^3 p/m)^2}{r^2 8\pi r^4 \rho (1 - 2Gm/r)} + \mathcal{O}(l_p^3) > 0, \quad (6.36)$$

$$A_7 = -\frac{l_p^2 Gm(1 + p/\rho)(1 + 4\pi r^3 p/m)}{r(1 - 2Gm/r)} + \mathcal{O}(l_p^3) < 0, \quad (6.37)$$

and

$$B_1 = \frac{l_p^2 4\pi r^3 p}{r^2 m} + \mathcal{O}(l_p^3) > 0, \quad (6.38)$$

$$B_2 = -\frac{l_p^2}{r^2} \left(1 + \frac{4\pi r^3 p}{m}\right) + \mathcal{O}(l_p^3) < 0, \quad (6.39)$$

$$B_3 = -\frac{l_p^2 2Gm (1 + 4\pi r^3 p/m)}{r(1 - 2Gm/r)} + \mathcal{O}(l_p^3) < 0, \quad (6.40)$$

$$B_4 = \frac{l_p^2 Gm (1 + 4\pi r^3 p/m)}{r(1 - 2Gm/r)} + \mathcal{O}(l_p^3) > 0. \quad (6.41)$$

Since all  $(Gm/r) \sim 0$ ,  $(r^3 p/m) \sim 0$ ,  $(r^3 \rho/m) \sim 0$ , and  $(p/\rho) \neq \infty$  as  $r \rightarrow 0$ , no singularity occur on each  $A_i$  and  $B_i$  at  $r = r_c \sim 0$  as long as  $r_c > l_p$ . Substituting all  $A_i$

and  $B_i$  into  $m'$ , we obtain

$$\begin{aligned} \sum_{i=1}^7 A_i &= \frac{l_p^2}{r^2} \left[ \frac{3p}{\rho} - 2 \frac{m(1+4\pi r^3 p/m)}{4\pi r^3 \rho} - \frac{Gm^2(1+4\pi r^3 p/m)}{4\pi r^4 \rho(1-2Gm/r)} \right. \\ &\quad \left. + \frac{Gm^2(1+4\pi r^3 p/m)^2}{8\pi r^4 \rho(1-2Gm/r)} - \frac{Gm(1+p/\rho)(1+4\pi r^3 p/m)}{r(1-2Gm/r)} \right] + \mathcal{O}(l_p^3), \end{aligned} \quad (6.42)$$

$$\sum_{i=1}^4 B_i = \frac{l_p^2}{r^2} \left[ -1 - \frac{Gm(1+4\pi r^3 p/m)}{r(1-2Gm/r)} \right] + \mathcal{O}(l_p^3). \quad (6.43)$$

The conditions on the surface of the object are  $p = 0$ ,  $\rho = \rho_0$ ,  $r = R$  and  $m = M$ . So at the surface, we have

$$p'(R) = -\frac{GM\rho_0}{R^2(1-2GM/R)} + \frac{G^2 l_p^2 M^2 \rho_0}{2R^5(1-2GM/R)^2} + \mathcal{O}(l_p^3) \quad (6.44)$$

and

$$\begin{aligned} \sum_{i=1}^7 A_i &= \frac{l_p^2}{R^2} \left[ -2 \frac{M}{4\pi R^3 \rho_0} - \frac{GM^2}{4\pi R^4 \rho_0 (1-2GM/R)} \right. \\ &\quad \left. + \frac{GM^2}{8\pi R^4 \rho_0 (1-2GM/R)} - \frac{GM}{R(1-2GM/R)} \right] + \mathcal{O}(l_p^3), \end{aligned} \quad (6.45)$$

$$\sum_{i=1}^4 B_i = \frac{l_p^2}{R^2} \left[ -1 - \frac{GM}{R(1-2GM/R)} \right] + \mathcal{O}(l_p^3). \quad (6.46)$$

It is easy to see that  $m'(R)$  is finite if  $\rho_0 \neq 0$ , although in the case of TOV GR,  $\rho_0 = 0$  corresponds to no solution. It seems that the changes of both  $R$  and  $M$  might be significant if the value of  $\rho_0$  goes to zero.

Now we investigate the region near the center. The subscript  $c$  will denote the value at the center. At  $r = r_c \sim 0$ , we have

$$\begin{aligned} \sum_{i=1}^7 A_i &= \frac{l_p^2}{r_c^2} \left[ \frac{3p_c}{\rho_c} - 2 \frac{(1+3p_c/\rho_c)}{3} - \frac{Gm_c^2(1+3p_c/\rho_c)}{4\pi r_c^4 \rho_c (1-2Gm_c/r_c)} \right. \\ &\quad \left. + \frac{Gm_c^2(1+3p_c/\rho_c)^2}{8\pi r_c^4 \rho_c (1-2Gm_c/r_c)} - \frac{Gm_c(1+p_c/\rho_c)(1+3p_c/\rho_c)}{r_c(1-2Gm_c/r_c)} \right] + \mathcal{O}(l_p^3) \\ &= \frac{l_p^2}{r_c^2} \left[ \frac{p_c}{\rho_c} - \frac{2}{3} \right] + \mathcal{O}(r_c^2), \end{aligned} \quad (6.47)$$

$$\sum_{i=1}^4 B_i = \frac{l_p^2}{r_c^2} \left[ -1 - \frac{Gm_c(1+3p_c/\rho_c)}{r_c(1-2Gm_c/r_c)} \right] + \mathcal{O}(l_p^3) = -\frac{l_p^2}{r_c^2} + \mathcal{O}(r_c^2). \quad (6.48)$$

We use the usual expression for mass  $m_c = (4/3)\pi\rho_c r_c^3$  in the second equality. After substituting into  $p'$  and  $m'$ , we have

$$p'(r_c) \sim -\frac{4}{3}\pi G r_c (\rho_c + p_c)(\rho_c + 3p_c) + \frac{8}{9}\pi^2 G^2 l_p^2 r_c (\rho_c + p_c)(\rho_c + 3p_c)^2 \quad (6.49)$$

and

$$m'(r_c) \sim 4\pi r_c^2 \rho_c \left( \frac{1 + (l_p/r_c)^2 (3p_c/\rho_c - 2/3)}{1 - (l_p/r_c)^2} \right). \quad (6.50)$$

From the above expressions,  $m'(r_c)$  is singular at  $r_c = l_p$ .

For now, let us set  $r_c = \alpha l_p$  where  $\alpha > 0$  and  $\alpha \neq 1$ . Then, Eq. (6.49) can be reexpressed as follows

$$p'(r_c) \simeq -\frac{4}{3}\pi G \rho_c^2 \left( 1 + \frac{p_c}{\rho_c} \right) \left( 1 + 3\frac{p_c}{\rho_c} \right) \alpha l_p \left[ 1 - \frac{2}{3}\pi G \rho_c \left( 1 + 3\frac{p_c}{\rho_c} \right) l_p^2 \right]. \quad (6.51)$$

In the square bracket, if  $\alpha l_p^3$  is sufficiently larger than  $\alpha l_p$ , the second term can be more dominant than the first term. Hence,  $p'(r) < 0$  needs sufficiently small  $\alpha l_p^3$ . Looking at Eq. (6.51), we may see the pattern in the higher-order terms to be  $\mathcal{O}(\alpha l_p^{2n+1})$ , with  $n$  an integer. This means that first we hold  $l_p$  then adjust  $\alpha$  such that the first term still dominates the second term in Eq. (6.51), whose consequence is

$$l_p < \sqrt{\frac{3}{2\pi G(\rho_c + 3p_c)}}, \text{ or equivalently, } N < \frac{18}{L_{\text{Pl}}^2 G(\rho_c + 3p_c)}. \quad (6.52)$$

Hence, both  $p_c$  and the EoS affect the upper bound of  $l_p$  and the strong energy condition should be satisfied due to the square root in Eq. (6.52).

Now we look at  $m'$ . Using the same approximation as for  $p'$ , Eq. (6.50) becomes

$$m'(r_c) \sim 4\pi r_c^2 \rho_c \left[ 1 - \frac{3p_c/\rho_c + 1/3}{1 - \alpha^2} \right]. \quad (6.53)$$

Since in the limit of TOV GR, the mass should grow from center to surface ( $m' > 0$ ). In the case of  $\alpha > 1$ ,  $m'(r_c) > 0$  is trivially satisfied. On the other hand in the case of  $\alpha < 1$  and if the second term inside the square bracket is less than unity,  $m'(r_c) > 0$  can happen. This implies

$$3p_c < (2/3 - \alpha^2)\rho_c. \quad (6.54)$$

In the case of  $\alpha = \sqrt{2/3}$ , then  $p_c < 0$ . This is in contradiction to our assumptions that  $p > 0$  and  $\rho > 0$  inside the star. In the case of  $\alpha > \sqrt{2/3}$ , then

$$\rho_c < -\left( \frac{3p_c}{\alpha^2 - 2/3} \right) < 0. \quad (6.55)$$

This expression is also in contradiction to our assumptions. Lastly, in the case of  $\alpha < \sqrt{2/3}$ , then

$$\rho_c > \left( \frac{3p_c}{2/3 - \alpha^2} \right) > 4.5p_c, \quad (6.56)$$

which implies  $dp/d\rho = w < 2/9$ , which means that the squared speed of sound is lower than the upper bound from both QCD ( $w \leq 1/3$ ) and causality ( $w \leq 1$ ) [112]. This, in consequence, leads to lower compactness, according to Ref. [53], which stated that by a linear equation of state (EoS)  $\rho = p/w + \rho_0$  and using TOV GR, the produced maximum compactness is

$$\left( \frac{2GM}{R} \right)_{\max} \sim \frac{8}{9 \left( \frac{0.51w+0.77}{w(w+4.18)} + 1 \right)}. \quad (6.57)$$

The expression on the right-hand side is a monotonically increasing function of  $w$ , but the compactness  $2GM/R$  cannot go beyond the Buchdahl limit  $2GM/R = 8/9$ . Also notice that this condition of  $m'(r)$  applies only at  $r = r_c$ , so it may not be true for  $r > r_c$ . But, since the equation of state is unchanging from any regions of  $r$ , this condition should hold even when  $r \gg r_c$ .

For now consider negative  $m_c$ , which is possible according to Ref [113], so that the case of  $\alpha < 1$  can be investigated. Then, we can see from Eq. (6.43) that  $m'(r)$  at  $\alpha = 1$  has no singularity anymore. If we demand  $\sum_i B_i > 0$  then we can obtain

$$m_c < \frac{\rho_c r_c}{G\rho_c - 3Gp_c} \equiv m_{c,\max}. \quad (6.58)$$

From assumption  $m_c < 0$ , we can obtain another restriction for the EoS, i.e.,

$$w > 1/3. \quad (6.59)$$

Notice that  $m_{c,\max} \rightarrow 0$  if  $r_c$  is sufficiently small, so we can use the limit from negative value  $m_c \rightarrow 0^-$ . In this limit, Eq. (6.30) becomes  $p'(r_c) < 0$ , thus the pressure decreases from  $p_c$ . Eq. (6.42) becomes

$$\sum_i A_i \sim \alpha^{-2} \left[ \frac{p_c}{\rho_c} - \frac{2}{3} \right]. \quad (6.60)$$

Since we want  $\sum_i B_i > 0$  and  $m'(r) > 0$ , then

$$w > 2/3. \quad (6.61)$$

Recall that these came from considering the limit of  $m_c \rightarrow 0^-$ . On the other hand, in the

limit of  $m_c \rightarrow -\infty$ , from Eq. (6.30) we have

$$0 > m_c > -4\pi r_c^3 p_c \equiv m_{c,min}, \quad (6.62)$$

which set the minimum value of  $m_c$ . Again, if  $r_c$  is sufficiently small,  $m_{c,min} \rightarrow 0$ . Hence, for the case of  $m_c < 0$ , we obtain  $w > 2/3$  and  $m_{c,min} < m_c < m_{c,max}$  that restricts  $w$  and  $m_c$ .

Since the restriction of  $m_c < 0$  is tight if  $r_c$  very small, we do not use the  $m_c < 0$  case in the following sections and rather use  $m_c = 4\pi r_c^3 \rho_c/3$ .

## 6.4 Numerical Results

The following linear EoS

$$\rho(p) = p/w + \rho_0 \quad (6.63)$$

is used in this study. The constant  $\rho_0$  define the energy density at the surface that act like a surface tension.  $\rho_0 \neq 0$  because no solution exists for  $\rho_0 = 0$ . Also,  $\rho_0$  cannot be negative, or it will violate weak energy condition [53]. The constant  $w$ , defined as  $w = dp/d\rho$ , is the speed of sound squared from thermodynamics and Newtonian mechanics.  $w$  is restricted to at least two conditions [112]:

1.  $0 < w \leq 1$  from causality, and
2.  $0 < w \leq 1/3$  from QCD.

Hence, we shall choose  $1/3 \leq w \leq 1$  and  $\alpha > 1$  because we want the largest compactness possible from the model.

We need to fix suitable value for  $l_p$ ,  $\alpha$ ,  $\rho_0$ , and  $p_c$  carefully such that all boundary conditions are satisfied before integrating  $p'$  and  $m'$  numerically. The units we use here follows Ref. [89], which is called ‘NS’ units. In this units,  $r$  is in metres, both  $p$  and  $\rho$  are in MeV/fm<sup>3</sup>, and  $m$  is in the solar mass  $M_\odot$ , which has unit MeV m<sup>3</sup>/fm<sup>3</sup>. Here we use the compactness defined as  $C = GM/R$  and  $\rho_0$  related to the MIT bag constant  $B$  by  $\rho_0 = 4B$  [54].

The upper bound of  $l_p$  can now be estimated. Since it is usual to have  $p_c$  and  $\rho_0$  around  $\sim 10^3$  MeV/fm<sup>3</sup>, then by Eq. (6.52), we obtain  $l_p \lesssim 10$  km, which is trivial since neutron stars usually has  $R \sim 10$  km. This is equivalent to  $N < 10^{79}$ . By this, the absolute value of RSET should satisfy

$$|\langle T_{\mu\nu} \rangle| < \frac{|T_{\mu\nu}|}{3.162 \times 10^{52} \text{ kg m}^3 \text{ s}^{-2}}. \quad (6.64)$$

This is in SI units, where  $\hbar c = 3.162 \times 10^{-27} \text{ kg m}^3 \text{ s}^{-2}$ .

It is also interesting to see that by

$$p' = -\frac{(p + \rho)X}{r \left(1 + \sqrt{1 + (l_p/r)^2 X}\right)}, \quad (6.65)$$

which is equivalent to Eq. (6.17), the numerical calculation is much more smooth. This is because the smallness of  $l_p$  often make computers cannot detect the second term in the square root of Eq. (6.17), which then make  $p' = 0$  in some regions of  $r$ . We can evade this problem if we use Eq. (6.65).

In the following numerical results, we shall show that the contribution of  $l_p$  does not affect the maximum mass significantly. This can be seen in Fig. 6.1, which are profiles from variation of  $w$ . There  $w$  does increase the mass and the radius, but this can also be obtained from the standard TOV equation in GR.

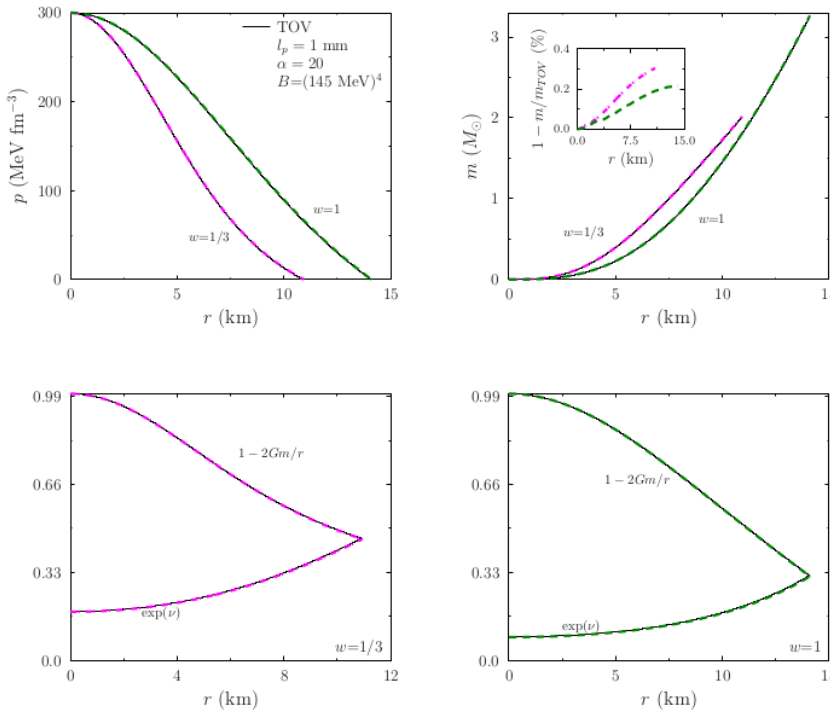


**Figure 6.1:** These are some profiles of  $p$  and  $m$  in the upper panels from setting  $l_p = 1 \text{ mm}$  and  $\alpha = 20$ . Here we vary  $w$ .  $\exp(\nu)$  and  $1 - 2Gm/r$  are shown in the lower panels.

Similar profiles also arise from varying  $B$ ,  $\alpha$  and  $l_p$ . In Figs. 6.2, 6.3, 6.4 and 6.5,

Universitas Indonesia

variations of  $w$ ,  $B$ ,  $\alpha$  and  $l_p$ , respectively, are used to produce the M-R curves. It is clear that the semi-classical correction does not affect the M-R relation compared to TOV GR.

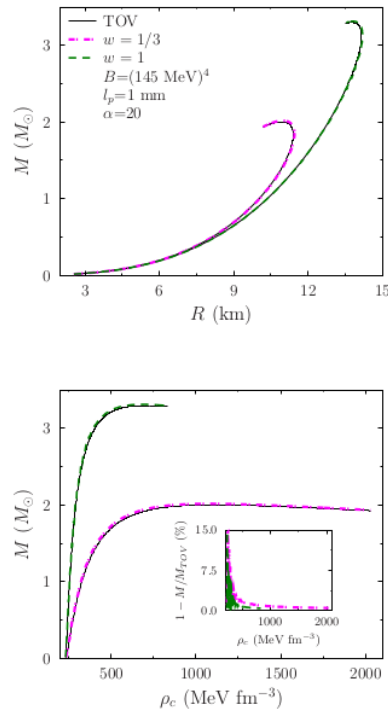


**Figure 6.2:** Here are the M-R curves from variations of  $w$ .

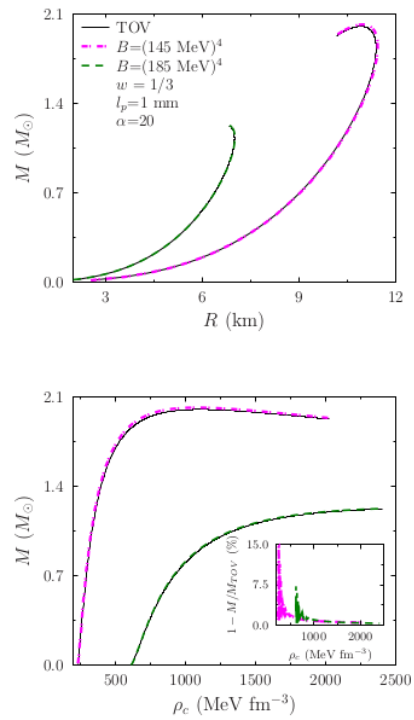


**Figure 6.3:** Here are the M-R curves from variations of  $B$ . If  $B$  is decreased, it produces higher mass and larger radius.

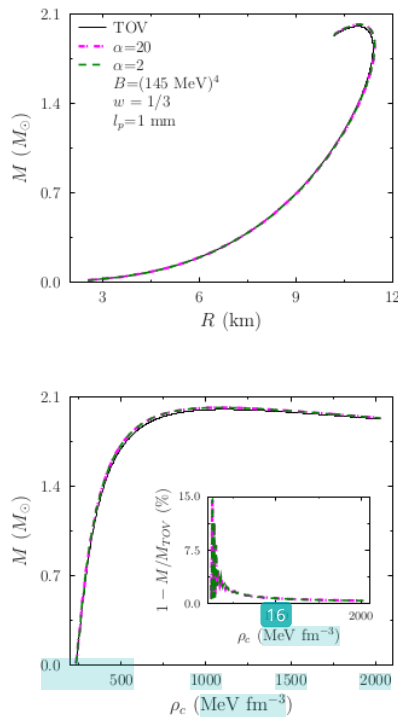


**Figure 6.4:** Here are the M-R curves from variations of  $\alpha$ .

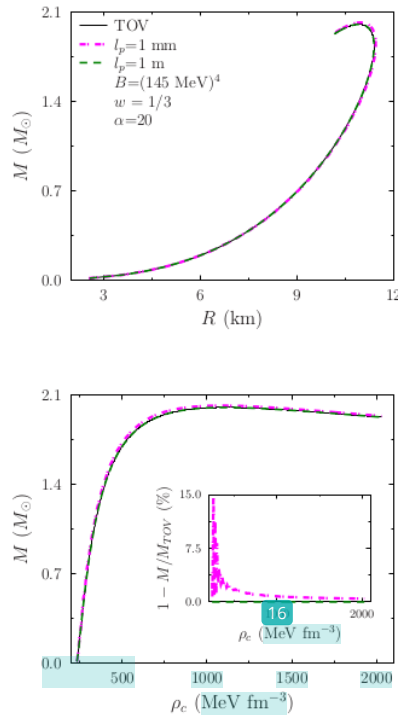


**Figure 6.5:** Here are the M-R curves from variations of  $l_p$ .

We tried using  $\alpha < 1$ , but we failed to find any numerical solution that satisfies the boundary conditions on both the center and the surface. Even though the mass profile increases a little in the beginning, the mass always goes to a negative value later on. It is intriguing that for the similar case in Ref. [108] (they use constant energy density) their integration method breaks down at  $r = l_p$ . They integrate the equations from the surface to the center, which we show in Appendix A to be consistent if we integrate from the center to the surface.

Moreover, although we have a similar aspect compared to Ref. [108], our results are different from theirs since they use  $m_c < 0$  while we use  $m_c = 0$ . This negative  $m_c$ , because they integrate from the surface to the center, is not an input anymore. Our  $m_c = 0$  case here gives only slightly larger compactness than the Buchdahl bound, but their results from negative  $m_c$  can give compactness very near the black hole limit. For details about this, see the following section.

## 6.5 Numerical Verification

This passage is a part of our first work which had been published in PRD (Ref. [101]). As a disclaimer, all the calculations are done using *Mathematica 10.0* in this chapter. On the other hand, our calculations in Chapter 7 uses *FORTRAN77*.

Here, we explain the integration schemes used in this chapter. We call the schemes used here as <sup>8</sup>*forward* integration and *backward* integration, respectively, to denote the integration from the center of the star to its surface and vice versa. One can do either forward integration or backward integration for the standard TOV equation and the result will be the same. Yet, it is not true anymore for the positive branch we discussed before, which does not become the standard TOV equation in the limit  $l_p \rightarrow 0$ .

We shall discuss in detail both schemes in reproducing the solutions, by numerical calculation, in

1. the negative branch obtained previously by Ho and Matsuo [108] in the case of constant energy density  $\rho$ , and
2. the positive branch obtained previously by Carballo-Rubio [5] using constant  $\lambda$  trick.

We emphasize these schemes because we use forward integration in the previous sections, but both Refs. [5] and [108] use backward integration. We shall show that we get consistent results from both schemes for the negative branch, but inconsistent for the positive branch.

### 6.5.1 Numerical solutions from negative branch

Suppose we use the tortoise coordinate  $r_*$ , rather than  $r$ , hence  $g_{rr}$  is redefined by

$$g_{rr} = C(r)/F^2(r), \quad (6.66)$$

$$C(r) = e^{\nu(r)}, \quad (6.67)$$

and the constants are renamed by  $\alpha = l_p^2$  and  $\kappa = 8\pi G$ . These definitions are going to be used only in this subsection. Then the Eqs. (6.9) and (6.10) become

$$\begin{aligned} 0 &= -\frac{1}{8r^2C(r)^2} \left[ -3\alpha F(r)^2 C'(r)^2 + 4rC(r)^2 F(r)F'(r) \right. \\ &\quad \left. + 2C(r)F(r) (\alpha C'(r)F'(r)) + F(r) (\alpha C''(r) - 2rC'(r))) \right. \\ &\quad \left. + 2\kappa r^2 C(r)^3 (p + \rho) \right], \end{aligned} \quad (6.68)$$

$$\begin{aligned} 0 &= \frac{1}{4r^2C(r)^2} \left[ \alpha F(r)^2 C'(r)^2 - \alpha C(r)F(r) (F(r)C''(r) + C'(r)F'(r)) \right. \\ &\quad \left. - 2C(r)^2 F(r) (rF'(r) + F(r)) + C(r)^3 (2 - \kappa r^2(\rho - p)) \right]. \end{aligned} \quad (6.69)$$

These are equivalent to Eqs. (5.7) and (5.8) in Ref. [108]. To avoid confusion, we use  $\rho$  and  $\nu$  to denote energy density and metric function, respectively, and  $m$  is still used as the mass function. (In Ref. [108] the authors use  $m$  and  $\rho$  to denote energy density and metric function, respectively.)

Choosing the energy density to be constant  $\rho = \rho_0$ , then from Eq. (6.8), we obtain

$$p(r) = -\rho_0 + p_0 e^{-\nu(r)/2}. \quad (6.70)$$

Here  $p_0 = \rho_0 \sqrt{1 - 2GM/R}$  (with  $M = m(R)$ ) to satisfy  $p(R) = 0$ .

The equations above are still evaluated in terms of  $r$ . Since we want to integrate these equations in terms of the tortoise radius  $\eta_*$ , we define

$$\eta_* = \int \frac{dr}{F(r)}. \quad (6.71)$$

Then Eqs. (6.68) and (6.69) become differential equations for  $r(r_*)$  and  $\nu(r_*)$ , respectively,

$$\begin{aligned} 0 &= -\frac{1}{8r(r_*)^2} \left[ 2 \{ \alpha \nu''(r_*) - 2r(r_*) \nu'(r_*) r'(r_*) \} \right. \\ &\quad \left. + 4r(r_*) r''(r_*) + 2\kappa r(r_*)^2 p_0 e^{\nu(r_*)/2} - \alpha [\nu'(r_*)]^2 \right], \end{aligned} \quad (6.72)$$

$$\begin{aligned} 0 &= \frac{1}{4r(r_*)^2} \left[ -\alpha \nu''(r_*) - 2(r(r_*) r''(r_*) + [r'(r_*)]^2) \right. \\ &\quad \left. + e^{\nu(r_*)} [2 - \kappa r(r_*)^2 (2\rho_0 - p_0 e^{-\nu(r_*)/2})] \right]. \end{aligned} \quad (6.73)$$

If Eq. (6.72) is substracted by Eq. (6.73), the result is a quadratic equation for  $\eta'(r_*)$ . Its roots correspond to the negative and positive branch. Because, in this subsection, we focus only on the negative branch we choose one of the two roots, i.e.,

$$\nu'(r_*) = -\frac{2}{\alpha} \left( r(r_*) r'(r_*) - \sqrt{Y} \right), \quad (6.74)$$

with

$$\text{15} \quad Y = r(r_*)^2 \left( \alpha \kappa p_0 e^{\frac{\nu(r_*)}{2}} + r'(r_*)^2 - \alpha \kappa \rho_0 e^{\nu(r_*)} \right) + \alpha \left( e^{\nu(r_*)} - r'(r_*)^2 \right). \quad (6.75)$$

This form becomes the standard TOV equation in the limit  $\alpha \rightarrow 0$ . This choice then give us  $\nu''(r_*)$ , which implies

$$\begin{aligned} r''(r_*) &= \frac{1}{4(\alpha - r(r_*)^2)r'(r_*)} \left[ \kappa r(r_*)^2 e^{\frac{\nu(r_*)}{2}} \left( 2\rho_0 e^{\frac{\nu(r_*)}{2}} - p_0 \right) \right. \\ &\quad \times \left( 2\sqrt{Y} - \alpha \nu'(r_*) \right) - \left( 2\sqrt{Y} - \alpha \nu'(r_*) \right) 2e^{\nu(r_*)} \\ &\quad \left. + 4r(r_*)r'(r_*) \left( \alpha \kappa p_0 e^{\frac{\nu(r_*)}{2}} + r'(r_*)^2 - \alpha \kappa \rho_0 e^{\nu(r_*)} \right) \right]. \end{aligned} \quad (6.76)$$

This came from adding Eq. (6.72) and Eq. (6.73).

Thus, we have  $\nu(r_*)$  as a first order ordinary differential equation (ODE) while  $r(r_*)$  is a second order ODE. These ODEs have parameters:  $M$ ,  $R_* = r_*(R)$ ,  $\rho_0$ , and two coupling constants:  $\alpha$  and  $\kappa$ . Because we do the backward integration, the initial conditions at  $r_* = R_*$  are as follows:

$$R_* = R + 2GM \ln(R/2GM - 1), \quad (6.77)$$

$$\nu(R_*) = \ln(\sqrt{1 - 2GM/R}), \quad (6.78)$$

$$r(R_*) = R, \quad (6.79)$$

$$r'(R_*) = 1 - 2GM/R. \quad (6.80)$$

We follow the recipe in Ref. [108] to fix the three input parameters  $R$ ,  $M$ , and  $\rho_0$ : (1) fix  $M$  first, then (2) fix  $R$  such that  $R > 2GM$ , lastly (3) explore the values of  $\rho_0$ .

For every  $\rho_0$  value, we have different value of shooting parameter  $k = 2GM/R$ , with  $0 < k < 1$ .  $k$  is carefully chosen so that at the center the slope of  $p(r_*)$  is not steep ( $|p'(r_* \rightarrow -\infty)| < \infty$ ). These steps are done due to the following reason. When we integrate the equation in the opposite direction (forward integration), we can get the same curves as the TOV equation in the limit of zero  $\alpha$ . This can be done if  $|p'(r_*)| < \infty$  because by doing so, the pressure does not increase or decrease too rapidly. Second, in the TOV GR system,  $p'(r = 0) \sim 0$  so the negative branch, for sufficiently small  $\alpha$ , should also has this property. We assume that  $r_*$  is linear to  $r$  in the region near  $r = 0$  so that  $p'(r_* = 0) \sim 0$ , which implies  $|p'(r \rightarrow 0)| < \infty$ . [Of course, this assumption is generally not true, as was shown in Ref. [108]. But, this assumption is true in the case of regular geometry discussed in Ref. [108]. See subsection 6.5.3 for more details.]

Now we calculate the ODEs by backward integration and recalculate using forward integration. The results from comparing these two schemes are shown in Fig. 6.6. We see

that the results from forward integration and backward integration are the same. Indeed in the limit of  $r_* \rightarrow -\infty$ , the pressure does not go to the Planck scale for the macroscopic size of  $R$ .

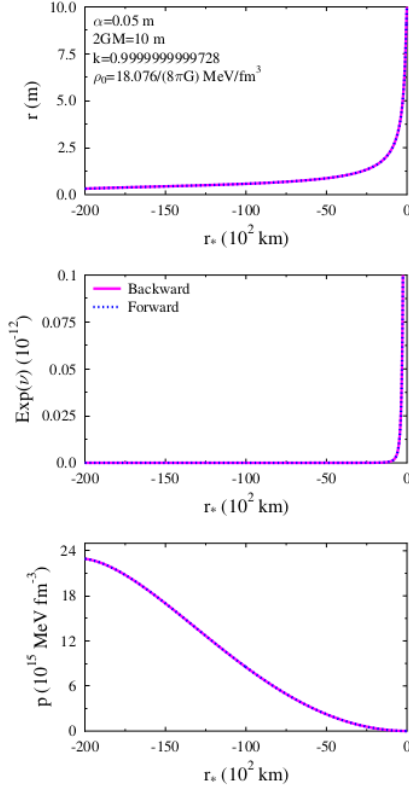


**Figure 6.6:** Here are the backward and forward integration results on the negative branch. Here  $k = 2GM/R$  is the shooting parameter which is chosen so that  $p'(r_* = 0) \sim 0$ .  $\text{Exp}(\nu)$  goes really close to zero but never reach zero as  $r_* \rightarrow -\infty$ .

### 6.5.2 Forward and backward integration solutions from positive branch

Carballo-Rubio, in Ref. [5], had shown that the positive branch has exact solutions. These solutions behaves very similar to a mixture of gravastars and black stars. While energy density is still positive valued

$$\rho(r) = \frac{1 + \mathcal{O}(l_p^2/r^2)}{8\pi Gr^2 R^2} \left[ R^2 + r^2 e^{\frac{(\lambda+1)(r^2-R^2)}{l_p^2}} \right], \quad (6.81)$$

with  $\lambda > 1$  a constant, the pressure is negative

$$p = \frac{-1 + \mathcal{O}(l_p^2/r^2)}{8\pi G r^2 R^2} \left[ R^2 - r^2 e^{\frac{(\lambda+1)(r^2-R^2)}{l_p^2}} \right]. \quad (6.82)$$

Moreover, they satisfy weak, dominant, and null energy conditions, while violating the strong energy condition. This last condition is assumed unnecessary since it is violated by the Casimir energy phenomenon.

The important trick to derive Eqs. (6.82)-(6.81) is the introduction of  $\lambda > 1$ , which is a constant and defined as

$$\lambda \equiv \sqrt{1 + \frac{l_p^2}{r^2} \frac{2Gm}{r} \frac{(1 + 4\pi r^3 p/m)}{(1 - 2Gm/r)}}. \quad (6.83)$$

This constant implies a fixed form of EoS and mass profile

$$\rho = -p + \frac{l_p^2}{(\lambda+1)r} p', \quad (6.84)$$

$$m = \frac{r^3 (-8\pi G l_p^2 p + \lambda^2 - 1)}{2G (l_p^2 + (\lambda^2 - 1) r^2)}. \quad (6.85)$$

Since  $p(r=R)=0$ , we have the compactness

$$2C = \frac{2GM}{R} = \frac{1}{(l_p^2 / [R^2 (\lambda^2 - 1)] + 1)}, \quad (6.86)$$

with  $M = m(R)$ . The solution for the metric function is

$$\nu(r) = \nu(R) + \frac{(\lambda+1)(R^2 - r^2)}{l_p^2}, \quad (6.87)$$

with  $\nu(R) = \ln(1 - 2GM/R + \mathcal{O}(l_p^2/R^2))$ . Arbitrary compactness can be reached since it depends on  $\lambda$ . The system is also stable by curvature and boundary conditions arguments.

To reproduce the analytic solutions by numerical schemes, we need the equation for

**Universitas Indonesia**

the pressure. After some algebra, we obtain

$$p'(r) = g(r) + p(r)h(r), \quad (6.88)$$

$$g(r) = \frac{(\lambda + 1)^2 (l_p^4 + (\lambda - 2)l_p^2 r^2 - (\lambda^2 - 1)r^4)}{4\pi G l_p^2 r (l_p^2 - (\lambda + 1)r^2) (l_p^2 + (\lambda^2 - 1)r^2)}, \quad (6.89)$$

$$h(r) = \frac{2(\lambda + 1)r ((2\lambda + 1)l_p^4 + (\lambda^3 + \lambda^2 - 2\lambda - 2)l_p^2 r^2 - (\lambda - 1)(\lambda + 1)^2 r^4)}{l_p^2 (l_p^2 - (\lambda + 1)r^2) (l_p^2 + (\lambda^2 - 1)r^2)}. \quad (6.90)$$

We integrate this equation by backward integration starting from  $r = R$  and  $p(R) = 0$ . Since this is a first-order ODE,  $R$  is related to  $M$ . Hence, unlike in the previous subsection, there is no shooting parameter  $k$ . Notice that  $g(r)$  has singularity at  $r = 0$ , so we expect uncontrolled behavior of  $p$  near  $r = 0$ . Then, from the result of backward integration, we numerically integrate it again by forward integration.

The result from backward integration is shown in top panel of Fig. 6.7. It is clear that it violates  $|p'(r \rightarrow 0)| < \infty$  as  $r \rightarrow 0$ . The numerical result from backward integration perfectly fits the analytic solution Eq. (6.82)

Then, for the forward integration, we tried to use the smallest possible  $r = r_c \sim 0$  as the initial position and its corresponding  $p(r_c)$  from the data from backward integration. The resulting curve is shown in the middle panel, while the comparison in Log plot is in the bottom panel. The results from backward and forward integration are different. The real and imaginary words in the legends denote the real and imaginary part of  $\log(p/p_c)$ . The pressure  $p/p_c$  from forward integration suddenly goes to zero at  $r = r_f$  much earlier than  $R$  from the backward integration. It is easily seen using the Log plot since when  $p/p_c < 0$ ,  $\log(p/p_c) \in \mathbb{C}$ . In Fig. 6.7, we obtain that  $r_f \sim 5$  m while  $R = 10$  km. We do not know how to remedy this yet.

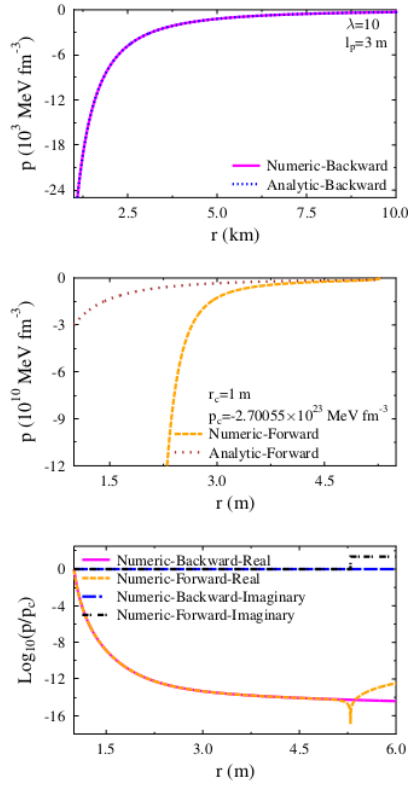


**Figure 6.7:** These are the profiles of pressure in the positive branch from backward integration (top panel), forward integration (middle panel), and the comparison between them (bottom panel). We calculate first by backward integration, then the result is used for forward integration. In the most bottom panel, we show the real and imaginary part of  $\log(p/p_c)$  since, for the forward integration,  $p/p_c = 0$  at  $r = r_f \sim 5$  m is much smaller than  $R = 10$  km. It is easier to see since  $\log(p/p_c) \in \mathbb{C}$  when  $p/p_c < 0$ .

### 6.5.3 Comparison of our numerical results with the density for regular geometry part of Ho-Matsuo model

In this subsubsection, we discuss the validity of our numerical calculation by comparing the result of section 6.1.3, density for regular geometry in Ref. [108] with the same constant energy density EoS but calculated by our code. We numerically calculate them using backward and forward integrations to check the consistency of the numerical calculation from both our equations and the equations in Ref. [108] restricted only in the interior of the star, which means that the geometry is regular for  $0 \leq r \leq R$ , and pressure is both finite and positive valued. As a disclaimer, we do not investigate the cases of too small density and too large density from the Ho-Matsuo model. This is because in the cases of too small density and too large density,  $r_*(r)$  is not a bijective map, i.e., when  $r$  is

increased,  $r_*$  is not monotonically increasing.

We had reproduced some relatively similar plots compared with Fig. 14 and Fig. 15 of Ref. [108]. These are shown in Fig. 6.6. The trend of the plots satisfies the condition discussed in section 6.1.3 of Ref. [108]. However, we are unable to reproduce exactly the quantitative result as shown in Fig. 14 and Fig. 15 of Ref. [108], because the authors of Ref. [108] did not specify the units they are using. We only guess the initial data until we obtain similar behavior for both  $r(r_*)$  and  $\nu(r_*)$ , i.e., both  $R$  and  $\rho_0$  are suitably chosen (with  $2GM$  fixed) such that  $p(r_*)$  decreases monotonically as  $r_*$  increases. It turns out that this method gives us  $r$  that is increasing monotonically as  $r_*$  increases. This aspect is similar to the ones in Ref. [108], so in principle, we can replace  $r$  with  $r_*$  and vice versa. All functions of  $r_*$  in Fig. 6.6 are shown as functions of  $r$  in Fig. 6.8. There, the numerical calculation result by integrating the equations (6.74)-(6.76) from center to surface are shown. We compare it with the usual TOV equation in GR. Note that  $p$  becomes very steep as  $r$  goes to zero since  $r$ , as a function of  $r_*$ , drops really quick in that area ( $r$  near zero). Also, note that  $m_c$  (mass near the center) is both large in magnitude and negative valued. We suspect that this negative and large magnitude  $m_c$  may be the reason why the compactness can be very close to the black hole limit ( $2GM/R = 1$ ). However, this value is outside the range from our lower and upper bound ( $m_{c,min}$  and  $m_{c,max}$ ) from Eq. (6.62) and Eq. (6.58), which is  $-10^{-3}M_\odot \lesssim m_c \lesssim -10^{-7}M_\odot$ . Therefore, it seems that our analytical estimation for the upper and lower bound of negative  $m_c$  may not be justified for constant energy density EoS.

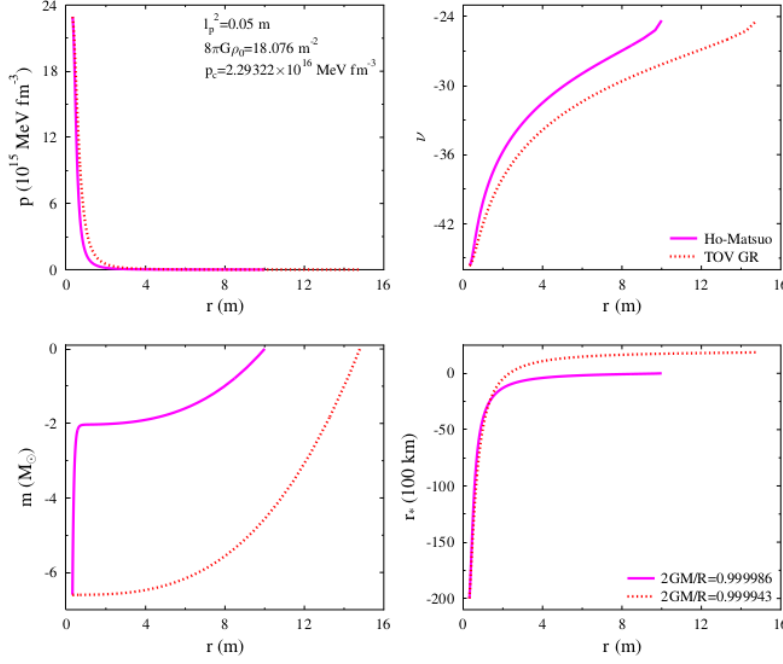


**Figure 6.8:** In these plots, the dashed line is from the TOV GR system, but the solid line is the same as in Fig. 6.6. Both results are integrated from center to surface. Because in SCGrav system  $r$  is restricted to  $r > l_p$ ,  $p$  then will never go to infinity. But in TOV GR,  $r$  can be arbitrarily close to zero, so  $p$  will eventually go to infinity. Notice also that the mass at the center ( $m_c$ ) is negative.

We also observe that the system should have very large density  $\rho_0$  and central pressure  $p_c$  to obtain large compactness. We estimate that, in our units,  $\rho_0 \sim 10^{12} \text{ MeV fm}^{-3}$ , which is about nine orders of magnitude larger than the bag constants  $B$  that we used in the previous section. From Fig. 6.8, notice that  $p_c \sim 10^{16} \text{ MeV fm}^{-3}$ , which is larger than the energy density. If we input  $\rho_0$  and  $p_c$  around this estimation, but now with  $m_c = 0$ , into our equations (6.18)-(6.29) and integrate them from  $r = \alpha l_p$  to  $r = R$ , then the compactness is less than when  $m_c < 0$ . It is shown in Fig. 6.9, where the compactness is slightly above the Buchdahl limit (BL)  $2GM/R = 8/9$ . Note that  $r_*$  is also monotonically increasing as  $r$  increases.

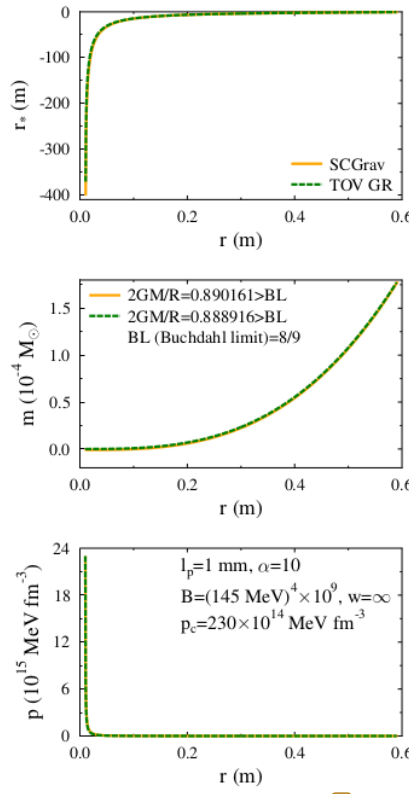


**Figure 6.9:** Here we use linear EoS with  $1/w = 0$ ,  $B \sim 10^{12} \text{ MeV fm}^{-3}$ , and  $p_c \sim 10^{16} \text{ MeV fm}^{-3}$  and  $m_c = 0$ . The compactness is less than black hole limit, unlike Fig. 6.8, although slightly larger than Buchdahl limit (BL). 6

From our previous results, we hypothesize that a very high uniform density and central pressure can give us a star with compactness beyond BL. To test this, we vary  $w$ ,  $B$ , and  $p_c$  and calculate similar profiles as Fig. 6.9. The results are compiled in Table 6.1. The variations are blue-colored, and if the resulting compactness violates BL, it is red-colored. We vary  $w$ ,  $p_c$ , and  $B$  in the top, middle, and bottom three rows, respectively. We can see that if  $w$  increases, then the compactness is increased. To obtain compactness over BL, however,  $B$  and  $p_c$  should be increased up to at least eight and thirteen orders of magnitude larger, respectively, than  $B$  and  $p_c$  in the upper three rows. [The entries with bold fonts are from Fig. 6.9.] We compare the resulting compactness from SCGrav with the result from TOV GR and find that the compactness is quite close to SCGrav. Of course, the results from TOV GR will have infinite pressure as  $r \rightarrow 0$ , if the compactness violates the Buchdahl limit. This is not the case for the SCGrav model since  $r$  is restricted to  $r > l_p > 0$ .

**Table 6.1:** Here we show the effect from variations of  $w$ ,  $B$ , and  $p_c$ , with  $m_c = 0$ , into compactness in our semiclassical model (SCGrav) using constant density EoS. The resulting compactness is compared to the TOV GR system counterparts.

$l_p(\text{m})$	$\alpha$	$p_c(\text{MeV fm}^{-3})$	$w$	$B(\text{MeV}^4)$	$2GM/R(\text{SCGrav})$	$2GM/R(\text{TOV GR})$
0.001	10	230	1/3	$(145)^4$	0.531671 < BL	0.528683 < BL
0.001	10	230	1	$(145)^4$	0.662569 < BL	0.658682 < BL
0.001	10	230	$\infty$	$(145)^4$	0.754262 < BL	0.74993 < BL
0.001	10	$230 \times 10^{12}$	$\infty$	$(145)^4 \times 10^9$	0.888742 < BL	0.888769 < BL
0.001	10	$230 \times 10^{13}$	$\infty$	$(145)^4 \times 10^9$	0.888961 > BL	0.888902 > BL
<b>0.001</b>	<b>10</b>	<b><math>230 \times 10^{14}</math></b>	$\infty$	$(145)^4 \times 10^9$	<b>0.890161 &gt; BL</b>	<b>0.888916 &gt; BL</b>
0.001	10	$230 \times 10^{14}$	$\infty$	$(145)^4 \times 10^8$	0.889297 > BL	0.888892 > BL
0.001	10	$230 \times 10^{14}$	$\infty$	$(145)^4 \times 10^7$	0.889019 > BL	0.888889 = BL
0.001	10	$230 \times 10^{14}$	$\infty$	$(145)^4 \times 10^6$	0.88893 > BL	0.888889 = BL

## 6.6 Conclusions

In this first part of our work, we investigate the semi-classical gravity proposed in Ref. [5]. Characterized by the positive-negative sign in  $p'$ , the model has two different sets of equations. This happened because the EFE for metric solution  $\nu'$  ((6.11)) has two roots and  $p'$  is related to  $\nu'$  by Eq. (6.8). Each is called as negative branch and positive branch. The positive branch and the negative branch, respectively, were discussed by [5] and by Ref. [108]. Here, we further investigate the negative branch by employing linear EoS  $\rho = p/w + \rho_0$  with  $w = 1/3$  and  $w = 1$ , respectively.

Here, we find that the choice of  $r_c$  affects the range of  $l_p$ . The reason is as follows. Because  $m'(r)$  is a lot more complicated than the usual TOV equation (see Eqs.(6.18)-(6.29)),  $m'(r)$  has terms that can make  $m'(r) < 0$ , which may imply negative  $m(r \gg r_c)$  if at the center  $m(r_c) = m_c \sim 0$ . Both  $l_p$  and  $r_c$  affect these terms in  $m'(r)$ , because  $m'(r_c)$  is singular when  $l_p = r_c$ .

To analyze  $m'(r)$  around  $l_p = r_c$ , we fix  $r_c = \alpha l_p$  with  $\alpha \neq 1$ . We also demand  $m'(r) > 0$  for  $0 < r < R$  because it is usual to expect the increase of mass as  $r$  increases, at least in TOV GR case. We found, with some approximations, that  $0 < \alpha < \sqrt{2/3}$ . This result demands a restricted set of EoS because the speed of sound squared  $w = dP/d\rho$  should satisfy  $w < 2/9$ . This implies less compactness  $GM/R$  than the results from  $w = 1/3$  and  $w = 1$ . Thus, we are not discussing the case of  $w < 2/9$ . For the case of  $\sqrt{2/3} \leq \alpha < 1$ , this implies either  $p_c < 0$  or  $\rho_c < 0$ . This contradicts our nonnegative pressure and energy density. For the case of  $\alpha > 1$ , we can use any EoS. Hence, our results does agree with Ref. [108], i.e., their integration breaks down at  $r = l_p$ .

The parameter  $l_p$  has an upper bound dependent on the central pressure  $p_c$ . By doing some approximations, we found that  $l_p < 10$  km from the dimensional analysis. This upper bound is in the same order of magnitude as the radius of known NSs. This upper bound also us  $N < 10^{79}$ , which implies that  $l_p$  can be huge compared to the Planck length.

Using variations of  $w$ ,  $B$ ,  $\alpha$ , and  $l_p$ , our numerical results show that the M-R relations are indistinguishable if compared to TOV GR. Thus, the parameter  $l_p$  has no significant effect compared to TOV GR, even though  $l_p$  is not in the limit  $l_p \rightarrow L_{\text{Pl}}$ .

The compactness can reach the ultra-compact range if we adjust both  $w$  and  $B$  suitably. But, this can also be achieved in TOV GR. Moreover, the Buchdahl limit could be violated using constant energy density (or  $w = \infty$ ), according to the authors in Ref. [108]. Thus, to see the significance of the semi-classical correction, it seems that we need to reach higher compactness larger than the Buchdahl limit. We still do not know how to do this exactly. We guess that we either decrease  $B$  to near zero or increase  $w$  such that  $w > 1$ . The drawback of choosing  $w > 1$  is that it violates causality, so we need other arguments to justify this choice.

This page intentionally left blank

## CHAPTER 7

### MOMENT OF INERTIA AND TIDAL DEFORMATION IN EDDINGTON-INSPIRED BORN INFELD THEORY OF GRAVITY

In this chapter, we present the second part of our work. The following passage are from our paper [114].

#### 7.1 Introduction

In this section, we explain the reasons why we investigate the predictions for NS properties using the EiBI gravity theory.

The Eddington-inspired Born-Infeld (EiBI) gravity is an interesting theory because of its features compared to those of General Relativity (GR) [28, 29, 30, 31, 115, 32, 116, 117, 118]. The EiBI theory, proposed by Banados and Ferreira [29], is a combination of Palatini formalism and a gravitational version of the Born-Infeld electrodynamic theory. The reviews of the EiBI gravity and its applications can be found in Refs. [119, 120]. From the astrophysical point of view, the EiBI gravity is interesting because it can increase the maximum mass of a nonrotating compact object by increasing its nonlinearity parameter  $\kappa$  [33, 121, 122]. The other parameter in EiBI gravity,  $\lambda$ , corresponds to the cosmological constant  $\Lambda_c$  by  $\lambda = \kappa\Lambda_c + 1$ . People usually set  $\lambda = 1$  in most cases. However, the problem with  $\lambda = 1$  is that the radius also increases when the mass increases, and vice versa.

We need to note that, in the case of  $\lambda = 1$ , the moment of inertia of a type of compact star, whose matter is described by FPS EoS, was discussed in Ref. [31]. Furthermore, the authors of Ref. [31] showed that, if  $\kappa > 0$ , there always exists regular solution for compact stars and the corresponding maximum compactness is  $GM/R \sim 0.3$ , which is quite independent from  $\kappa$ . Also, there exists the collapse constraint, i.e., if the requirement  $\kappa\Delta < 0$  is satisfied, with  $\Delta$  is given as

$$\Delta = (p_c\kappa - 3\kappa\rho_c - 4)(1 + \kappa\rho_c) - \kappa(1 - \kappa p_c)(p_c + \rho_c) \frac{d\rho(p_c)}{dp_c},$$

then the compact stars exist. Here,  $p_c$  and  $\rho_c$  are, respectively, the star's central pressure and central density. This expression means that if the EoS obeys the thermodynamic relation, which implies  $\rho = \rho(p)$ , then the onset region of the star's stability in EiBI theory depends only on  $P_c$  and  $\kappa$ .

Concerned with the star's stability in EiBI theory with  $\lambda = 1$ , the authors of Ref. [123] shown that the standard results of stellar stability in GR also hold in EiBI, only up to the fundamental mode frequency. This means that for a sequence of stars with the same EoS, the fundamental mode  $\omega^2$  passes through zero at central density, whose value corresponds to the maximum-mass configuration. For higher-order, though, they depend on  $\kappa$ . This in turn implies that the stellar models with central densities less than the corresponding critical points are stable.

For the case of  $\kappa < 0$ , the EiBI theory shows singularities in the EoS and the Ricci scalar from the physical metric associated with the phase transition matter [124]. This happens because the discontinuity in energy density appears around the transition region. Furthermore, authors in Refs. [125, 126, 127, 128] had discussed the appearance of curvature singularities at the surface of compact stars with polytropic EoS in EiBI theory. However, as far as we know, there is no discussion regarding tidal deformation within EiBI theory in the literature up to now. Concerned with some recent NS observational results, we think that comparing the NS in EiBI theory with the recent NS constraints [57, 58, 82, 83, 84, 85] has not yet been done.

We also expect that setting  $\lambda$  away from unity might increase (or decrease) the maximum mass while also decrease (or increase) its radius. Thus, it can achieve relatively larger compactness, given suitable values of  $\kappa$  and  $\lambda$ . Since the cosmological constant  $\Lambda_c$  is related to  $\lambda$  by  $\lambda = \kappa\Lambda_c + 1$ , therefore, in the next sections, we investigate the role of  $\kappa$  and  $\Lambda_c$  to the mass, the radius, the moment of inertia, and the tidal deformation of NS in EiBI theory in more detail. Moreover, we relate our results with the question of the tension between nuclear physics and the prediction of NS properties. This includes the possibility of whether the second object with mass  $2.6M_\odot$  in the GW190814 event is static or slowly rotating NS. Here we use a quite recent G3 RMF parameter set from Ref. [34]. The representations of the EoS will also include contributions from hyperons and restriction to the speed of sound at high densities.

The reason why we use EiBI theory is that it has a nice property that the exterior solution (for a spherically symmetric system without electric nor magnetic source) is the same as general relativity (GR).

## 7.2 The Eddington-inspired Born-Infeld Theory of Gravity

Here, we review the EiBI theory and discuss the calculations of its moment of inertia and the tidal deformation. We start by reviewing the equations following Refs. [32, 33]. The

EiBI theory has the following equations of motions:

$$q^{\mu\nu} = \tau (\lambda g^{\mu\nu} - 8\pi G\kappa T^{\mu\nu}(\mathbf{g})), \quad (7.1)$$

$$q_{\mu\nu} = g_{\mu\nu} + \kappa R_{\mu\nu}(\mathbf{q}), \quad (7.2)$$

where  $\tau = \sqrt{g}/\sqrt{q}$ ,  $q = -\det(q_{\mu\nu})$ ,  $g = -\det(g_{\mu\nu})$ . It is common to use  $\tau = \sqrt{\det(g_{\sigma\nu})\det(q^{\mu\sigma})} = [\det(\lambda\delta_\nu^\mu - 8\pi G\kappa T_\nu^\mu)]^{-1/2}$ , because  $1/q = \det(q^{\mu\nu})$ . The constants  $\lambda$  and  $\kappa$  are the parameters of EiBI. Note that these are different from functions  $\bar{\lambda}(r)$  and  $\bar{\kappa}(r)$  which we shall define later. Also note that  $\kappa$  has dimension (length)<sup>2</sup> and  $\lambda$  is dimensionless. The cosmological constant  $\Lambda_c$  is related to  $\lambda$  by this relation:

$$\lambda = \kappa\Lambda_c + 1. \quad (7.3)$$

The arguments in  $R_{\mu\nu}$  and  $T^{\mu\nu}$  are different since to raise or lower the tensor indices, each tensor uses a different metric. The apparent metric  $q_{\mu\nu}$  is used by  $R_{\mu\nu}$  while the physical metric  $g_{\mu\nu}$  is used by  $T_{\mu\nu}$ . Those equations came from the EiBI action

$$S = \frac{1}{8\pi G\kappa} \int_{(\mathcal{M}, \mathbf{g})} d^4x \left[ \sqrt{-\det(g_{\mu\nu} + \kappa R_{\mu\nu}(\Gamma))} - \lambda \sqrt{-\det(g_{\mu\nu})} \right], \quad (7.4)$$

where Palatini formalism has been used to the Ricci tensor  $R_{\mu\nu}$ . The formalism means that the Ricci tensor is dependent on a connection  $\Gamma_{\beta\gamma}^\alpha(\mathbf{q})$ , but this connection is dependent on the apparent metric, i.e.,

$$\Gamma_{\beta\gamma}^\alpha = \frac{1}{2} q^{\alpha\sigma} (\partial_\gamma q_{\beta\sigma} + \partial_\beta q_{\gamma\sigma} - \partial_\sigma q_{\beta\gamma}). \quad (7.5)$$

One can rearrange these equation into the form similar to the usual Einstein field equation (EFE), which became

$$R_\nu^\mu(\mathbf{q}) - \frac{1}{2} R_\sigma^\sigma \delta_\nu^\mu(\mathbf{q}) = 8\pi G T_{\text{eff}\,\nu}^\mu(\mathbf{g}), \quad (7.6)$$

$$T_{\text{eff}\,\nu}^\mu(\mathbf{g}) = \tau T_\nu^\mu(\mathbf{g}) - \left[ \frac{\tau T_\sigma^\sigma(\mathbf{g})}{2} + \frac{1-\tau\lambda}{8\pi G\kappa} \right] \delta_\nu^\mu. \quad (7.7)$$

From knowing this and for brevity, we will write the Ricci tensor  $R_{\mu\nu}$  dan the stress tensor  $T_{\mu\nu}$  without their arguments.

### 7.2.1 Vacuum solution

Now we will discuss the effect of nonzero cosmological constant  $\Lambda_c$  to the compact stars in EiBI theory. First, the vacuum solution needs to be mentioned. This will be crucial

for our metric ansatz in the presence of ideal isotropic fluid so that we can obtain suitable equations of motion and boundary conditions. Suppose that we use static and spherically symmetric metric on both metrics

$$\mathbf{q} = q_{\mu\nu} dx^\mu dx^\nu = -C^2(r) dt^2 + D^2(r) dr^2 + r^2 [d\theta^2 + \sin^2 \theta d\varphi^2], \quad (7.8)$$

$$\mathbf{g} = g_{\mu\nu} dx^\mu dx^\nu = -A^2(r) dt^2 + B^2(r) dr^2 + F^2(r) [d\theta^2 + \sin^2 \theta d\varphi^2], \quad (7.9)$$

given no matter present  $T_\nu^\mu = 0$ . From Eq. (7.1) we have these metric relations

$$F^2 = r^2/\lambda, \quad (7.10)$$

$$A^2 = C^2/\lambda, \quad (7.11)$$

$$B^2 = D^2/\lambda. \quad (7.12)$$

Substituting these into Eq. (7.2), then we can obtain

$$C'' = \frac{DC - D^3C + rCD' + rDC' + r^2D'C'}{r^2D}, \quad (7.13)$$

$$\frac{C'}{C} = -\frac{1}{r} + \left( \frac{1}{r} - \frac{r}{\kappa} + \frac{r}{\kappa\lambda} \right) D^2 + \frac{D'}{D}, \quad (7.14)$$

$$\frac{D'}{D} = \frac{1}{2r} + \left( -\frac{1}{2r} + \frac{r}{2\kappa} - \frac{r}{2\kappa\lambda} \right) D^2, \quad (7.15)$$

where  $f' = df/dr$ . The solutions from these equations are

$$C^2 = D^{-2} = 1 - \frac{2GM}{r} - \frac{\Lambda_c r^2}{3\lambda}. \quad (7.16)$$

We can see that the apparent metric in the presence of no matter indicates an de-Sitter space with an “apparent” cosmological constant  $\Lambda_c/\lambda$ .

## 7.2.2 <sup>12</sup> Moment of Inertia

Now, to calculate the moment of inertia, we follow the Hartle-Thorne method. We start by setting the apparent and physical metric in these forms:

$$\mathbf{q} = q_{\mu\nu} dx^\mu dx^\nu = -e^{\beta(r)} dt^2 + e^{\alpha(r)} dr^2 + r^2 [d\theta^2 + \sin^2 \theta (d\varphi - \omega(r)dt)^2] + \mathcal{O}(\Omega^2), \quad (7.17)$$

$$\mathbf{g} = g_{\mu\nu} dx^\mu dx^\nu = -e^{\nu(r)} dt^2 + e^{\bar{\lambda}(r)} dr^2 + d(r) [d\theta^2 + \sin^2 \theta (d\varphi - v(r)dt)^2] + \mathcal{O}(\Omega^2). \quad (7.18)$$

The apparent metric follows the Hartle-Thorne metric [129] and its generalization is used in the physical metric. Both describe a spherically symmetric massive body with radius  $R$  with apparent (physical, resp.) angular velocity  $\omega$  ( $v$ ) goes to  $\Omega$  ( $\Omega_{\text{phy}}$ ) as  $r \rightarrow R$ . Here we use slow rotating approximation, i.e., if  $\Omega_k$  is defined as Kepler angular velocity, which the mass-shedding limit of any massive star, it is assumed that  $\Omega/\Omega_k \ll 1$  and  $\Omega_{\text{phy}}/\Omega_k \ll 1$ . From the vacuum solution, we see that the physical metric has its 2-sphere with radius  $\sqrt{d(r)}$ , which coincides with  $r$  at the exterior region  $r \geq R$ .

The massive body is modeled by an ideal fluid with isotropic pressure

$$T_\nu^\mu = [\epsilon + p] u^\mu u_\nu + p \delta_\nu^\mu, \quad (7.19)$$

$$u^t = [-(g_{tt} + 2\Omega_{\text{phy}} g_{t\varphi} + \Omega_{\text{phy}}^2 g_{\varphi\varphi})]^{-1/2}, \quad (7.20)$$

$$u^\varphi = \Omega_{\text{phy}} u^t, \quad u^r = u^\theta = 0. \quad (7.21)$$

The explicit expression of the components of the physical stress tensor are

$$T_t^t = -\epsilon, \quad T_r^r = T_\theta^\theta = T_\varphi^\varphi = p, \quad (7.22)$$

$$T_\varphi^t = (\epsilon + p)(\Omega_{\text{phy}} - v)e^{-\nu} d \sin^2 \theta, \quad (7.23)$$

$$T_t^\varphi = -(\epsilon + p)\Omega_{\text{phy}}. \quad (7.24)$$

These are obtained after neglecting  $\mathcal{O}(\Omega_{\text{phy}})$ . From these, then  $\tau$  is

$$\tau = 1/(ab^3), \quad (7.25)$$

$$a = \sqrt{\lambda + 8\pi G\kappa\epsilon}, \quad (7.26)$$

$$b = \sqrt{\lambda - 8\pi G\kappa p}. \quad (7.27)$$

From Eq. (7.1), we have these relations

$$e^\nu = e^\beta a/b^3, \quad e^{\bar{\lambda}} = e^\alpha/(ab), \quad d = r^2/(ab). \quad (7.28)$$

Now, we assume that the effective stress tensor also has similar form as the physical stress tensor, but to differentiate with the previous stress tensor, we add additional subscript “eff”. Their nonzero components are

$$T_{\text{eff } t}^t = -\epsilon_{\text{eff}}, \quad (7.29)$$

$$T_{\text{eff } r}^r = p_{\text{eff}} = T_{\text{eff } \theta}^\theta = T_{\text{eff } \varphi}^\varphi, \quad (7.30)$$

$$T_{\text{eff } \varphi}^t = (\epsilon_{\text{eff}} + p_{\text{eff}})(\Omega - \omega)e^{-\beta(r)}r^2 \sin^2 \theta. \quad (7.31)$$

Then we obtain these relations from the equations above,  $T_{\text{eff } \varphi}^t = T_\varphi^t/ab^3$ , and  $T_{\text{eff } t}^t =$

$T_t^\varphi/abc^2$ :

$$\epsilon_{\text{eff}} = \frac{a^2 - 3b^2 + 2ab^3}{16\pi G\kappa ab^3}, \quad (7.32)$$

$$p_{\text{eff}} = \frac{a^2 + b^2 - 2ab^3}{16\pi G\kappa ab^3}, \quad (7.33)$$

$$(\Omega - \omega) = (\Omega_{\text{phy}} - v) \frac{b^2}{a^2}, \quad (7.34)$$

$$\Omega = \Omega_{\text{phy}}. \quad (7.35)$$

The last equation is in agreement with the boundary condition, i.e.,  $(\Omega - \omega) \sim (\Omega_{\text{phy}} - v)$  at  $r \rightarrow R$ .

The nonzero components of the Ricci tensor  $R_{\mu\nu}(q)$  can be obtained straightforwardly. If we define the mass  $m(r)$  inside one of the metric function by

$$e^{-\alpha} = 1 - \frac{2Gm(r)}{r} - \frac{\Lambda_c r^2}{3\lambda}, \quad (7.36)$$

then with some algebraic calculations one can obtain

$$m'(r) = \frac{r^2}{4G\kappa} \left( \frac{2}{\lambda} - \frac{3}{ab} + \frac{a}{b^3} \right), \quad (7.37)$$

$$\beta'(r) = -2p'(r) \left[ 2\pi G\kappa \left( \frac{3}{b^2} + \frac{1}{a^2} \frac{d\epsilon}{dp} \right) + \frac{1}{\epsilon + p} \right], \quad (7.38)$$

$$\begin{aligned} p'(r) &= -\frac{1}{4\pi G\kappa} \left[ \frac{r}{2\kappa} \left( \frac{1}{ab} + \frac{a}{b^3} - 2 \right) + \frac{2Gm}{r^2} + \frac{\Lambda_c r}{3\lambda} \right] \\ &\times \left( \frac{4}{a^2 - b^2} + \frac{3}{b^2} + \frac{1}{a^2} \frac{d\epsilon}{dp} \right)^{-1} \left( 1 - \frac{2Gm(r)}{r} - \frac{\Lambda_c r^2}{3\lambda} \right)^{-1}. \end{aligned} \quad (7.39)$$

Eqs. (7.37) and (7.38) are from  $tt$  and  $rr$  components of the EFE, respectively. Eq. (7.39) came from the Bianchi identity  $\nabla_\mu T_{\text{eff}}^\mu_r = 0$ . The boundary conditions are  $m(0) = 0, m(R) = M, p(R) = 0, \beta(R) = \ln(1 - 2GM/R - \Lambda_c R^2/(3\lambda))$ . One can see that the equation of motions are invariant to  $\beta \rightarrow \beta + k$  ( $k$  a constant), so we can obtain the correct  $\beta(r)$  from arbitrary starting value of  $\beta(0) = \beta_{0,\text{old}}$ . The after running the code, we obtain  $\beta_R = \beta(R)$ . This can be used to obtain the correct initial value  $\beta(0)$  by

$$\beta_{0,\text{new}} = \beta_{0,\text{old}} - [\beta_R - \ln(1 - 2GM/R - \Lambda_c R^2/(3\lambda))]. \quad (7.40)$$

Then by running the program again, the correct  $\beta(r)$  will be obtained.

To obtain the moment of inertia, we need the equation of motion for  $\omega$ . It is in principle

can be derived from the  $t\varphi$  component of the EFE. We use the following formula [129]

$$R_\varphi^t = \frac{1}{\sqrt{-\det(q_{\alpha\beta})}} \partial_\mu \left( \sqrt{-\det(q_{\alpha\beta})} \Gamma_{\nu\varphi}^\mu q^{t\nu} \right), \quad (7.41)$$

to calculate the geometry part. From Eq. (7.41) and ignoring  $\mathcal{O}(\omega^2)$  terms, one obtains this component explicitly:

$$R_\varphi^t = -\frac{e^{-(\beta+\alpha)/2}}{2r^2 \sin \theta} \partial_r \left( e^{-(\beta+\alpha)/2} r^4 \sin^3 \theta \partial_r \omega \right). \quad (7.42)$$

From before, we have  $T_{\text{eff}\varphi}^t = (\epsilon_{\text{eff}} + p_{\text{eff}})(\Omega - \omega)e^{-\beta(r)}r^2 \sin^2 \theta$ . Defining  $\tilde{\omega} = (\Omega - \omega)/\Omega$ , then  $R_\varphi^t/(8\pi G) = T_{\text{eff}\varphi}^t$  becomes

$$\partial_r \left( e^{-(\beta+\alpha)/2} r^4 \partial_r \tilde{\omega} \right) = 16\pi G r^4 (\epsilon_{\text{eff}} + p_{\text{eff}}) e^{(\alpha-\beta)/2} \tilde{\omega}. \quad (7.43)$$

The boundary condition to calculate moment of inertia  $I$  is as follows. The right hand side in the equation above will vanish in the exterior region  $r \geq R$ , thus

$$\tilde{\omega}(r \geq R) = 1 - \frac{2GI}{r^3}, \quad (7.44)$$

Then by rearranging Eq. (7.43), one arrives at

$$\tilde{\omega}'(r) = \frac{6e^{\beta/2}}{r^4(1 - 2Gm/r - \Lambda_c r^2/(3\lambda))^{1/2}} \tilde{\kappa}, \quad (7.45)$$

$$\tilde{\kappa}'(r) = \frac{8\pi Gr^4}{3} \frac{(\epsilon_{\text{eff}} + p_{\text{eff}}) e^{-\beta/2}}{(1 - 2Gm/r - \Lambda_c r^2/(3\lambda))^{1/2}} \tilde{\omega}, \quad (7.46)$$

This form is neat because the boundary conditions are  $\tilde{\omega}(R) = 1 - 2GI/R^3$ ,  $\tilde{\kappa}(R) = GI$ . Since the boundary condition at the center is unknown, let us pay attention that Eqs. (7.45) and (7.46) are invariant from  $\tilde{\omega}(r) \rightarrow \zeta \tilde{\omega}(r)$  and  $\tilde{\kappa}(r) \rightarrow \zeta \tilde{\kappa}(r)$ . Suppose that we run the code from initial values  $\tilde{\omega}(0) = \tilde{\omega}_0$  and  $\tilde{\kappa}(0) = \tilde{\kappa}_0$ . Then the result can be written as  $\tilde{\omega}(R) = (1 - 2GI/R^3)/\zeta$  and  $\tilde{\kappa}(R) = GI/\zeta$ , with  $\zeta$  a constant. To satisfy the boundary conditions, we rename the previous initial values by a new ones, i.e.,  $\tilde{\omega}(0) = \tilde{\omega}_0 \zeta$  and  $\tilde{\kappa}(0) = \tilde{\kappa}_0 \zeta$  with

$$\zeta = \frac{1}{\tilde{\omega}(R) + 2\tilde{\kappa}(R)/R^3}. \quad (7.47)$$

since we already obtain the moment of inertia  $I$  from  $\tilde{\kappa}(R)$  by  $I = \tilde{\kappa}(R)\zeta/G$ , recalculating from these new initial values is unnecessary, although to confirm that, one can check it by running the code again. Now, following the logic in Refs. [31, 30], from the boundary conditions, then we have  $v(R) = \omega(R) = 2I\Omega/R^2$ . Thus,  $I$  is the physical moment of

inertia.

Here, we briefly describe the numerical procedure for the moment of inertia  $I$  as follows. We use a *FORTRAN77* code with Runge-Kutta 4th order algorithm. First, we calculate all  $p'(r)$ ,  $m'(r)$  and  $\nu'(r)$  (Eqs. (7.37)-(7.39)). We run the code from the center  $r = r_c \sim 0$  up to  $r = R$  where the pressure become zero  $p(R) = 0$ . The initial data at the center are  $p(r_c) = p_c$ ,  $m(r_c) = 0$  and  $\beta(r_c) = 0$ . At this point, we obtain  $R$ ,  $m(R) = M$  and  $\beta(R) = \beta_R$ . Since in general,  $\beta(R) \neq \ln(1 - 2GM/R - \Lambda_c R^2/(3\lambda))$ , we recalculate the equations  $p'(r)$ ,  $m'(r)$  and  $\nu'(r)$  by replacing the initial value  $\beta(r_c) = \beta_{0,\text{new}}$  using Eq. (7.40). Second, we calculate all  $p'(r)$ ,  $m'(r)$ ,  $\nu'(r)$ ,  $\tilde{\omega}'(r)$  and  $\tilde{\kappa}'(r)$  from  $r = r_c$  to  $r = R$ . From inputs  $p(r_c) = p_c$ ,  $m(r_c) = 0$ ,  $\beta(r_c) = \beta(r_c)_{\text{new}}$  and  $\tilde{\omega}(r_c) = \tilde{\kappa}(r_c) = 0$ , we obtain  $\tilde{\omega}(R)$  and  $\tilde{\kappa}(R)$ . The moment of inertia  $I$  is then calculated by  $I = \tilde{\kappa}(R)\zeta/G$  with  $\zeta$  from Eq. (7.47).

### 7.2.3 Tidal Deformation

Here we describe the theory of tidal perturbation, only the electric type, in the EiBI gravity. We follow the method illustrated in Refs. [131, 132]. We start with the Regge-Wheeler metric [130]. The perturbed metrics are

$$g_{\mu\nu} = \eta_{\mu\nu} + h_{\mu\nu}, \quad (7.48)$$

$$q_{\mu\nu} = \zeta_{\mu\nu} + f_{\mu\nu}, \quad (7.49)$$

with

$$h_{\mu\nu} = \begin{pmatrix} -H_0 e^\nu & H_1 & 0 & 0 \\ H_1 & H_2 e^{\bar{\lambda}} & 0 & 0 \\ 0 & 0 & Kr^2 & 0 \\ 0 & 0 & 0 & Kr^2 \sin^2 \theta \end{pmatrix} Y_{lm}(\theta, \phi), \quad (7.50)$$

$$f_{\mu\nu} = \begin{pmatrix} -F_0 e^\nu & F_1 & 0 & 0 \\ F_1 & F_2 e^{\bar{\lambda}} & 0 & 0 \\ 0 & 0 & \bar{G}r^2 & 0 \\ 0 & 0 & 0 & \bar{G}r^2 \sin^2 \theta \end{pmatrix} Y_{lm}(\theta, \phi), \quad (7.51)$$

while the unperturbed part is

$$\eta_{\mu\nu} dx^\mu dx^\nu = -e^{\nu(r)} dt^2 + e^{\bar{\lambda}(r)} dr^2 + d(r) d\Omega^2, \quad (7.52)$$

$$\zeta_{\mu\nu} dx^\mu dx^\nu = -e^{\beta(r)} dt^2 + e^{\alpha(r)} dr^2 + r^2 d\Omega^2, \quad (7.53)$$

with  $d\Omega^2$  is the surface element of a 2-sphere. Here,  $H_0$ ,  $H_1$ ,  $H_2$ ,  $K$ ,  $F_0$ ,  $F_1$ ,  $F_2$ , and  $\bar{G}$  are functions of  $r$ .

### 7.2.3.1 The vacuum case

To determine the Love number, which is calculated at region far from the star, we investigate the vacuum case first ( $T_\nu^\mu = 0$ ). From Eq. (7.1), one obtains

$$d = r^2/\lambda, e^\nu = e^\beta/\lambda, e^{\bar{\lambda}} = e^\alpha/\lambda, \quad (7.54)$$

$$H_0 = -H_2 = H, F_0 = -F_2 = F, \quad (7.55)$$

$$H = F, K = \bar{G}/\lambda. \quad (7.56)$$

From evaluating Eq. (7.2) order by order through some algebra, one can obtain the following equations:

$$e^\beta = e^{-\alpha} = 1 - \frac{2GM}{r} - \frac{\Lambda_c r^2}{3\lambda}, \quad (7.57)$$

$$F_1 \propto e^{(\alpha-\beta)/2}, \quad (7.58)$$

$$H_1 = F_1 \left( \frac{1}{\lambda} - \frac{l(l+1)\kappa}{2r^2} \right), \quad (7.59)$$

$$\begin{aligned} F'' &+ 2e^\alpha \left( \frac{1}{r} - \frac{\Lambda_c r}{\lambda} \right) F' - 2 \left( \frac{1}{r^2} - e^\alpha \frac{\Lambda_c}{\lambda} \right) F + e^\alpha \frac{(l-1)(l+2)}{r^2} G \\ &= 0. \end{aligned} \quad (7.60)$$

Then after more algebraic manipulations, the last line above becomes

$$F'' + \left[ \frac{1}{r} + e^\alpha \left( \frac{1}{r} - \frac{\Lambda_c r}{\lambda} \right) \right] F' - \left[ e^\alpha \left( \frac{l(l+1)}{r^2} + \frac{2\Lambda_c}{\lambda} \right) + \beta'^2 \right] F = 0. \quad (7.61)$$

Now we come to the tricky part. To calculate the tidal deformation, the calculation is done at  $r \rightarrow \infty$ , which is not satisfied by de Sitter space-time. To remedy this shortcoming, we assume that  $|\Lambda_c|$  is sufficiently small such that  $|G^2 M^2 \Lambda_c / \lambda| < 1$  hence  $F$  can be expressed as

$$F(x) = \sum_{i=0}^{\infty} F_i(x) \varepsilon^i, \quad \varepsilon = \frac{G^2 M^2 \Lambda_c}{\lambda}, \quad x = \frac{r}{GM} - 1. \quad (7.62)$$

We assuming that the series converge rapidly, so consider the terms only up to the first order:

$$F(x) = F_0(x) + \varepsilon F_1(x). \quad (7.63)$$

From  $\Lambda_c = 0$  we have the usual solution is known to have the form including the associ-

ated Legendre polynomial of the second kind  $Q_l^2$  and the first kind  $P_l^2$ :

$$F_0(x) = C_{1,l}Q_l^2(x) + C_{2,l}P_l^2(x). \quad (7.64)$$

The constants  $C_{1,l}$  and  $C_{2,l}$  will be determined later. Substitute this into Eq. (7.61) we obtain the equations fo  $F_1$ :

$$(1-x^2) \left( \frac{d^2F_1(x)}{dx^2} + D(x) \right) - 2x \frac{dF_1(x)}{dx} + \left( l(l+1) - \frac{4}{1-x^2} \right) F_1(x) = 0, \quad (7.65)$$

with

$$D(x) = -\frac{1}{3} \left( \frac{x+1}{x-1} \right)^2 \left[ 2(x-2) \frac{dF_0(x)}{dx} + \left( l(l+1) - \frac{6x^2 - 20x + 22}{1-x^2} \right) F_0(x) \right]. \quad (7.66)$$

The next step is we solve this (with  $l = 2, 3, 4$ ) case by case. In general, we obtain that the solution has the following form:

$$F_1(x) = C_{3,l}Q_l^2(x) + C_{4,l}P_l^2(x) + C_{2,l}S_l^2(x) + C_{1,l}T_l^2(x) \quad (7.67)$$

with

$$S_l^2(x) = \frac{f_{1,l}(x)}{x^2-1} + (x^2-1)f_{2,l}(x), \quad (7.68)$$

$$T_l^2(x) = \frac{f_{3,l}(x)}{(x+1)(x-1)^2} + \frac{f_{4,l}(x)}{x+1} \ln(x-1) \quad (7.69)$$

$$+ f_{5,l}(x) \left( \frac{x+1}{x-1} \right) \ln(x+1) + (x^2-1)f_{6,l}(x).$$

For  $l = 2$ , we have

$$f_{1,2} = \frac{8x^6}{7} + 6x^5 - \frac{x^4}{7} - \frac{59x^3}{4} - \frac{46x^2}{7} + \frac{21x}{4} + 1, \quad (7.70)$$

$$f_{2,2} = \frac{3}{56} (113 \log(x-1) + 15 \log(x+1)), \quad (7.71)$$

$$f_{3,2} = -\frac{8x^6}{7} + \frac{389x^5}{56} + \frac{2057x^4}{168} - \frac{1987x^3}{84} - \frac{1469x^2}{84} + \frac{1357x}{56} + \frac{235}{56}, \quad (7.72)$$

$$f_{4,2} = -\frac{4x^5}{7} - \frac{25x^4}{7} - \frac{17x^3}{14} + \frac{171x^2}{14} + \frac{153x}{14} - \frac{25}{14}, \quad (7.73)$$

$$f_{5,2} = \frac{4x^4}{7} + \frac{13x^3}{7} - \frac{93x^2}{14} + \frac{34x}{7} - \frac{25}{14}, \quad (7.74)$$

$$f_{6,2} = \frac{1}{7}(-24) \left( 2\text{Li}_2\left(\frac{1-x}{2}\right) + \ln\left(\frac{x+1}{4}\right) \ln(x-1) \right). \quad (7.75)$$

For  $l = 3$ , we have

$$f_{1,3} = \frac{20x^7}{3} + 40x^6 - \frac{20x^5}{7} - \frac{375x^4}{4} - \frac{220x^3}{7} + \frac{185x^2}{4} + 20x, \quad (7.76)$$

$$f_{2,3} = \frac{25}{56}x(127\log(x-1) + \log(x+1)), \quad (7.77)$$

$$f_{3,3} = -\frac{20x^7}{3} + \frac{8195x^6}{168} + \frac{5225x^5}{72} - \frac{35845x^4}{252} - \frac{9977x^3}{84} + \frac{7305x^2}{56} + \frac{8941x}{168} - 32, \quad (7.78)$$

$$f_{4,3} = -\frac{10x^6}{3} - \frac{70x^5}{3} - \frac{925x^4}{42} + \frac{3425x^3}{42} + \frac{195x^2}{2} - \frac{845x}{42} - \frac{635}{21}, \quad (7.79)$$

$$f_{5,3} = \frac{10x^5}{3} + \frac{40x^4}{3} - \frac{1315x^3}{42} + \frac{20x^2}{7} + \frac{135x}{14} + \frac{5}{21}, \quad (7.80)$$

$$f_{6,3} = \frac{1}{7}(-200)x \left( 2\text{Li}_2\left(\frac{1-x}{2}\right) + \ln\left(\frac{x+1}{4}\right) \ln(x-1) \right). \quad (7.81)$$

For  $l = 4$ , we have

$$f_{1,4} = \frac{595x^8}{22} + 175x^7 - \frac{277315x^6}{4928} - \frac{14305x^5}{32} - \frac{202325x^4}{4928} + \frac{14405x^3}{48} + \frac{342515x^2}{4928} - \frac{1225x}{32} - \frac{615}{64}, \quad (7.82)$$

$$f_{2,4} = \frac{25(7x^2-1)(7613\log(x-1) + 67\log(x+1))}{4928}, \quad (7.83)$$

$$f_{3,4} = -\frac{595x^8}{22} + \frac{1159715x^7}{6336} + \frac{14823115x^6}{44352} - \frac{8024815x^5}{14784} - \frac{3123931x^4}{4928} + \frac{7841513x^3}{14784} + \frac{169207x^2}{448} - \frac{7430627x}{44352} - \frac{2160637}{44352}, \quad (7.84)$$

$$f_{4,4} = -\frac{595x^7}{44} - \frac{4445x^6}{44} - \frac{38235x^5}{308} + \frac{113875x^4}{308} + \frac{154025x^3}{308} - \frac{42865x^2}{308} - \frac{6715x}{28} - \frac{3735}{308}, \quad (7.85)$$

$$f_{5,4} = \frac{595x^6}{44} + \frac{665x^5}{11} - \frac{34285x^4}{308} - \frac{4540x^3}{77} + \frac{30455x^2}{308} + \frac{535x}{77} - \frac{3735}{308}, \quad (7.86)$$

$$f_{6,4} = \frac{1}{77}(-1500)(7x^2-1) \left( 2\text{Li}_2\left(\frac{1-x}{2}\right) + \ln\left(\frac{x+1}{4}\right) \ln(x-1) \right). \quad (7.87)$$

$\text{Li}_n(z)$  is the polylogarithm function.

Next we need to obtain  $C_{1,l}$ ,  $C_{2,l}$ ,  $C_{3,l}$ , and  $C_{4,l}$ . It turns out that the general results

have the following pattern

$$C_{1,l} = A_{1,l} + \lambda_l B_{1,l}, \quad (7.88)$$

$$C_{2,l} = A_{2,l} + \lambda_l B_{2,l}, \quad (7.89)$$

$$C_{3,l} = A_{3,l} + \lambda_l B_{3,l}, \quad (7.90)$$

$$C_{4,l} = A_{4,l} + \lambda_l B_{4,l}. \quad (7.91)$$

The constants  $A_{n,l}$  and  $B_{n,l}$  ( $n = 1, \dots, 4$ ) has the following pattern:  $A_{i,l} \propto \mathcal{E}_m(GM)^l$  and  $B_{i,l} \propto \mathcal{E}_m(GM)^{-l-1}$  ( $i = 1, 2, 3, 4$ ), where  $\mathcal{E}_m$  is related to the static external quadrupolar tidal field, which is produced by an external gravitational potential. If subjected to this gravitational potential, then the star is responding by its own quadrupole moment, which is recorded by  $\lambda_l$ . Then,  $\lambda_l$  is related to the Love number  $k_l$ .

To obtain  $\lambda_l$  and getting rid of  $\mathcal{E}_m$ , we define  $y(R) = RF'(R)/F(R)$  and  $C = GM/R$ . We substitute

$$F(x) = (C_{1,l} + \varepsilon C_{3,l})Q_l^2(x) + (C_{2,l} + \varepsilon C_{4,l})P_l^2(x) + \varepsilon C_{2,l}S_l^2(x) + \varepsilon C_{1,l}T_l^2(x) \quad (7.92)$$

into  $y$ , then through another long calculations, we obtain

$$\lambda_l = -\frac{(A_{1,l} + \varepsilon A_{3,l})Q^*(R) + (A_{2,l} + \varepsilon A_{4,l})P^*(R) + \varepsilon(A_{1,l}T^*(R) + A_{2,l}S^*(R))}{(B_{1,l} + \varepsilon B_{3,l})Q^*(R) + (B_{2,l} + \varepsilon B_{4,l})P^*(R) + \varepsilon(B_{1,l}T^*(R) + B_{2,l}S^*(R))}, \quad (7.93)$$

where

$$Q^*(R) = yQ_l^2(C) + C[dQ_l^2(C)/dC], \quad (7.94)$$

$$P^*(R) = yP_l^2(C) + C[dP_l^2(C)/dC], \quad (7.95)$$

$$T^*(R) = yT_l^2(C) + C[dT_l^2(C)/dC], \quad (7.96)$$

$$S^*(R) = yS_l^2(C) + C[dS_l^2(C)/dC]. \quad (7.97)$$

Then, we can obtain the Love number by this relation:

$$k_l = \frac{(2l-1)!!}{2R^{2l+1}}\lambda_l. \quad (7.98)$$

Notice that since  $\lambda_l \propto a_{i,l}/b_{i,l} \propto (GM)^{2l+1}$ , then  $\lambda_l R^{-2l-1} \propto C^{2l+1}$ , which then allows us to we redefine  $k_l$  with

$$k_l = -\frac{(2l-1)!!}{2} \frac{(a_{1,l} + \varepsilon a_{3,l})Q^*(R) + (a_{2,l} + \varepsilon a_{4,l})P^*(R) + \varepsilon(a_{1,l}T^*(R) + a_{2,l}S^*(R))}{(b_{1,l} + \varepsilon b_{3,l})Q^*(R) + (b_{2,l} + \varepsilon b_{4,l})P^*(R) + \varepsilon(b_{1,l}T^*(R) + b_{2,l}S^*(R))}, \quad (7.99)$$

with  $a_{i,l}$  and  $b_{i,l}$  as functions of  $C$ . Note that the reason we use Eq. (7.99) is because this form is more easy to write in the *FORTRAN77* code than Eq. (7.93). In their explicit form, the constants are shown below:

$$\boxed{a_{1,2}} = 0, \quad b_{1,2} = \frac{15}{8} \frac{1}{C^3}, \quad (7.100)$$

$$\boxed{a_{2,2}} = \frac{1}{3} C^2, \quad b_{2,2} = 0, \quad (7.101)$$

$$\boxed{a_{3,2}} = \frac{113}{84} C^2, \quad b_{3,2} = \frac{1787}{392} \frac{1}{C^3}, \quad (7.102)$$

$$\boxed{a_{4,2}} = \frac{13}{9} C^2, \quad b_{4,2} = -\left(\frac{5\pi^2}{7} + \frac{3305}{448} + \frac{15\ln^2(2)}{7}\right) \frac{1}{C^3}, \quad (7.103)$$

$$\boxed{a_{1,3}} = 0, \quad b_{1,3} = \frac{35}{8} \frac{1}{C^4}, \quad (7.104)$$

$$\boxed{a_{2,3}} = \frac{1}{45} C^3, \quad b_{2,3} = 0, \quad (7.105)$$

$$\boxed{a_{3,3}} = \frac{127}{756} C^3, \quad b_{3,3} = \frac{24805}{1512} \frac{1}{C^4}, \quad (7.106)$$

$$\boxed{a_{4,3}} = \frac{158}{945} C^3, \quad b_{4,3} = -\left(\frac{25\pi^2}{9} + \frac{13795}{576} + \frac{25\ln^2(2)}{3}\right) \frac{1}{C^4}, \quad (7.107)$$

$$\boxed{a_{1,4}} = 0, \quad b_{1,4} = \frac{735}{64} \frac{1}{C^5}, \quad (7.108)$$

$$\boxed{a_{2,4}} = \frac{1}{630} C^4, \quad b_{2,4} = 0, \quad (7.109)$$

$$\boxed{a_{3,4}} = \frac{7613}{465696} C^4, \quad b_{3,4} = \frac{469685}{5808} \frac{1}{C^5}, \quad (7.110)$$

$$\boxed{a_{4,4}} = \frac{200077}{10866240} C^4, \quad b_{4,4} = -\left(\frac{875\pi^2}{88} + \frac{14680085}{202752} + \frac{2625\ln^2(2)}{88}\right) \frac{1}{C^5}. \quad (7.111)$$

### 7.2.3.2 The Non-vacuum case

One can see that to obtain the Love number, Eq. (7.99) needs  $y(R)$ ,  $M = m(R)$ , and  $r = R$  as input. So we need the equations of  $y(r)$  in the interior. The metric is still the same but now we use ideal fluid in the stress tensor, rather than the empty space. We define the perturbed stress tensor as follows

$$T_\nu^\mu = T_0^\mu{}_\nu + \delta T_\nu^\mu, \quad (7.112)$$

with  $T_0^\mu{}_\nu$  is the usual ideal fluid and

$$\delta T_\nu^\mu = \text{diag} \left( -\frac{d\epsilon}{dp}, 1, 1, 1 \right) \delta p Y_{lm}(\theta, \phi). \quad (7.113)$$

Then, from Eq. 7.1, we obtain the relations between the metric functions:

$$d = r^2/(ab), \quad e^\nu = e^\beta a/b^3, \quad e^{\bar{\lambda}} = e^\alpha/(ab), \quad (7.114)$$

$$H_0 = H, \quad H_2 = -Ha^2/b^2, \quad F_0 = -F_2 = F. \quad (7.115)$$

One can evaluate Eq. (7.2) order by order and use mathematical identities of the spherical harmonics  $Y_{lm}(\theta, \phi)$ , which gives the following equations:

$$H = \frac{16\pi G\kappa\delta p}{b^2 - a^2}, \quad (7.116)$$

$$K = \frac{\bar{G}}{ab} + \frac{4\pi G\kappa}{ab} \left( \frac{1}{b^2} - \frac{1}{a^2} \frac{d\epsilon}{dp} \right) \delta p, \quad (7.117)$$

$$F = 4\pi G\kappa \left( \frac{4}{b^2 - a^2} - \frac{3}{b^2} - \frac{1}{a^2} \frac{d\epsilon}{dp} \right) \delta p \quad (7.118)$$

Eliminating  $\delta p$ , we have

$$H = \frac{4}{a^2 - b^2} \left( \frac{4}{a^2 - b^2} + \frac{3}{b^2} + \frac{1}{a^2} \frac{d\epsilon}{dp} \right)^{-1} F, \quad (7.119)$$

$$F_1 = Ce^{(\alpha-\beta)/2}, \quad (7.120)$$

$$H_1 = F_1 \left( \frac{a}{b^3} - \frac{l(l+1)\kappa}{2r^2} \right). \quad (7.121)$$

Lastly, after lots of calculations, we have

$$\begin{aligned} F'' &+ e^\alpha \left( \frac{2}{r} + \frac{r}{2\kappa} \left( -4 + \frac{a}{b^3} + \frac{3}{ab} \right) \right) F' - \left( \frac{2}{r^2} - \frac{e^\alpha}{\kappa} \left( 2 - \frac{3a}{b^3} + \frac{1}{ab} \right) \right) F \\ &+ e^\alpha \left( \frac{(l-1)(l+2)}{r^2} - \frac{2}{ab\kappa} \right) \bar{G} + K \left( \frac{2e^\alpha}{\kappa} \right) = 0. \end{aligned} \quad (7.122)$$

After some more algebraic manipulation, this becomes

$$F'' + f(r)F' + g(r)F = 0, \quad (7.123)$$

with

$$f(r) = \frac{re^{\alpha(r)}}{\kappa} \left( \frac{1}{ab} - 1 \right) + \frac{e^{\alpha(r)}}{r} + \frac{1}{r}, \quad (7.124)$$

$$\begin{aligned} g(r) &= \frac{2e^\alpha}{\kappa b^3} \left( 2 - \frac{4}{(a^2 - b^2)} \left( \frac{4}{a^2 - b^2} + \frac{1}{a^2} \frac{d\epsilon}{dp} + \frac{3}{b^2} \right)^{-1} \right) \\ &\quad - \left( \frac{l(l+1)e^\alpha}{r^2} + \frac{2e^\alpha}{\kappa} + \beta'(r)^2 \right). \end{aligned} \quad (7.125)$$

Defining  $y(r) = rF'(r)/F(r)$ , we thus obtain the first order equation

$$\overset{15}{y}'(r) = -f(r)y(r) - rg(r) - \frac{y(r)^2}{r} + \frac{y(r)}{r}. \quad (7.126)$$

The boundary condition is  $y(0) = l$ . Since  $|k_4| \ll |k_3| \ll |k_2|$ , it is also a usual practice to only evaluate  $k_2$  (using Eq. (7.99)) as the so-called dimensionless tidal deformability  $\Lambda$ :

$$\Lambda = \frac{2k_2}{3c^5}. \quad (7.127)$$

The numerical scheme for the tidal calculation is as follows. First, we calculate  $p'(r)$ ,  $m'(r)$  and  $y'(r)$  (resp., Eqs. (7.37), (7.39) and (7.126)) using the Runge-Kutta 4th order algorithm using our *FORTRAN77* code. We run the code from  $r = r_c \rightarrow 0$ , after inputting the initial values  $p(r_c) = p_c$ ,  $m(r_c) = 0$  and  $y(r_c) = l$ , to  $r = R$  where  $p(R) = 0$ . At this point, we obtain  $R$ ,  $m(R) = M$  and  $y(R)$ . These three numbers are substituted into Eq. (7.93) to calculate  $k_l$  using .

### <sup>12</sup> 7.3 Numerical Results and Discussions

In this section, we show the numerical results by employing the EoS calculated from RMF theory with the G3 parameter set. We include hyperons contribution and the speed of sound constrain in the EoS (denoted by WHSS). This speed of sound constrain is just forcing it to obey  $v_s \leq c/\sqrt{3}$  at high densities. Here, we mainly use WHSS because (1) we suspect that hyperon matter exists in heavy NSs with mass  $M \gtrsim 2.0M_\odot$ , and (2) the speed of sound constraint stiffens the matter and thus increases the maximum mass. We also sometimes compare the results with those from EoS without hyperon (WoutHSS). Furthermore, to restrict the range of  $\kappa$  and  $\Lambda_c$ , we compare the results with the known observational analysis data.

The role of  $\kappa$  to adjust the mass and radius of NS had been studied in Ref. [33]. However, in this work, we use different EoSs, which are also more refined, and more recent constraints of NS properties are also used. After that, we show the impact of  $\Lambda_c$  on

25  
the mass-radius (M-R) relation, the moment of inertia  $I$ , and the Love number  $\Lambda$  to see its tidal deformability.

First, we consider the standard case  $\Lambda_c = 0$  (or  $\lambda = 1$ ). In Fig. 7.1, we show the mass-radius relation. The results from G3 WHSS EoS and G3 WoutHSS EoS are presented in panel (a) and panel (b), respectively. From Fig. 7.1, we see that the  $M$  and  $R$  of NS increase simultaneously if we increase the  $\kappa$  value. This impact is significant independent of the type of EoS used. Observe that the  $2.1M_\odot$  mass constraint from PSR J0740+6620 (grey band) can be easily reached by the maximum mass while also still satisfy the radius constraint from NSs with a mass around  $1.4M_\odot$  [57, 58]. Observe also that, due to its softer EoS, G3 WHSS EoS needs a larger value of  $\kappa$  to reach  $2.6M_\odot$  mass constraint from GW190814 (orange band), which in turn does not satisfy the radius constraint (Refs. [57, 58]).

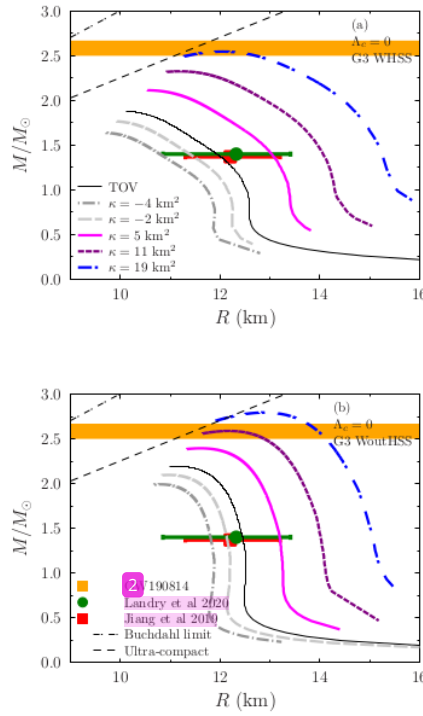


**Figure 7.1:** From varying  $\kappa$  with  $\Lambda_c = 0$ , the M-R relation result is shown here. We use G3 EoS with hyperon and sound of speed constraint (WHSS) in panel (a). On the other hand, we use no hyperon but still with the sound of speed constraint (WoutHSS) in panel (b). Observe that by increasing  $\kappa$ , both  $M$  and  $R$  will increase. We find that  $\kappa$  can have a negative value and the solutions exist if  $\kappa > -5 \text{ km}^2$ , which is similar to Ref. [33].

We include a realistic case of  $\Lambda_c = 2.08 \times 10^{-52} \text{ m}^{-2}$ , which came from the observed cosmological constant in Refs. [133, 134, 135, 136]

$$\rho_{\Lambda_c} = \frac{\Lambda_c}{8\pi G} \sim 10^{-8} \frac{\text{erg}}{\text{cm}^3}. \quad (7.128)$$

We use this value as the upper bound for  $\Lambda_c$  in this realistic case. This choice is safe from an unphysical phenomenon due to the following reason. Consider  $|\Lambda_c| \geq 10^{-22} \text{ m}^{-2}$ ,  $\lambda = 1$ ,  $M = 1M_\odot$  and  $r = 1 \text{ AU}$  in Eq. (7.36), then the term with  $\Lambda_c$  will dominate, hence Newtonian gravity breaks down in the solar system. We can see that the results are almost indistinguishable if compared to the results from  $\Lambda_c = 0$ , because of the smallness of the observed  $\Lambda_c$  value. In Figs. 7.2-7.4, we show the result from  $\kappa$  variations and show the resulting M-R relation, moment inertia, and tidal deformation. It is evident that our results, when  $\kappa$  is much larger than  $5 \text{ km}^2$ , are not in good agreement with observation data from canonical mass NSs ( $1.4M_\odot$ ). Due to our choice of EoS, it is evident that the  $2.1M_\odot$  mass constraint can be reached when  $\kappa \approx 5 \text{ km}^2$ . Hence, we conclude that the NS properties predicted by EiBI theory is compatible with the recent observational constraints from Refs. [57, 58, 73, 7, 82, 83] if we choose a physically save  $\Lambda_c$  value in the range of  $0 \leq \Lambda_c \leq 2.08 \times 10^{-52} \text{ m}^{-2}$  and  $\kappa \approx 5 \text{ km}^2$ . (In fact, this result is valid for  $|\Lambda_c| < 10^{-22} \text{ m}^{-2}$ , since  $\lambda$  is still very close to unity when  $\kappa \sim 10^8 \text{ m}^2$ .)

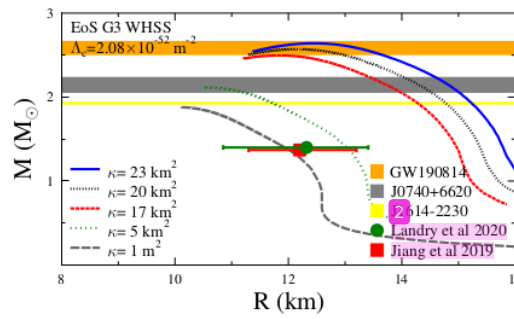


**Figure 7.2:** Here are the M-R relations from G3 WHSS EoS with  $\kappa$  variations and  $\Lambda_c = 2.08 \times 10^{-52} \text{ m}^{-2}$ . These are compared to the data from Landry et al 2020 [57], Jiang et al 2019 [58], the pulsar-binary systems (PSRs) J1614-2230 [71, 72, 73], J0740+6620 [73, 7], and the GW190814 data [6].

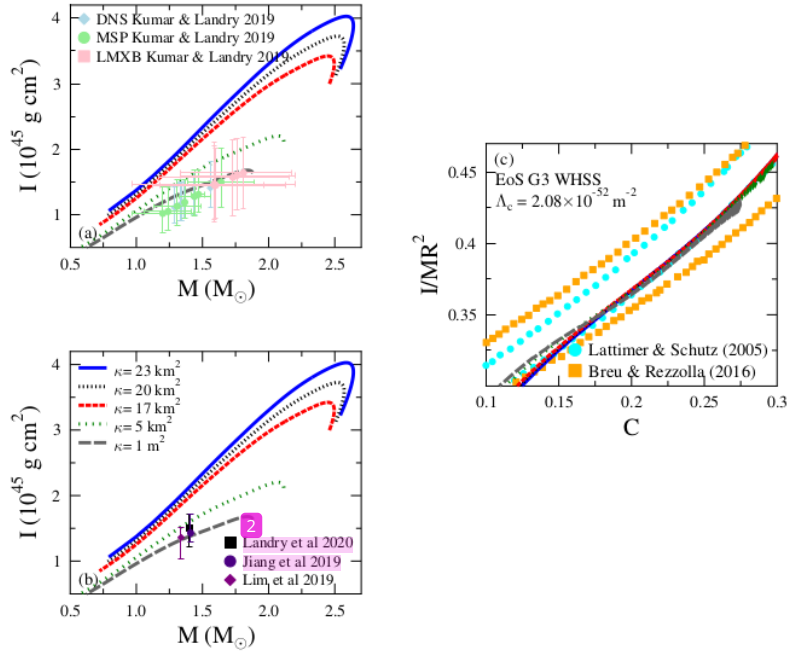


**Figure 7.3:** These are the moment of inertia  $I$  from G3 WHSS EoS with  $\kappa$  variations and  $\Lambda_c = 2.08 \times 10^{-52} \text{ m}^{-2}$ . In panel (a), we compare them with data from Kumar & Landry 2019 [82], where the specific method used there are labelled as DNS, MSP, and LMXB. In panel (b), we use data from Landry et al 2020 [57], Jiang et al 2019 [58], and Lim et al 2019 [83]. In panel (c), we compare  $I/MR^2$  with the upper and lower bound data from Lattimer & Schutz 2005 [84] and Breu & Rezzolla 2016 [85].

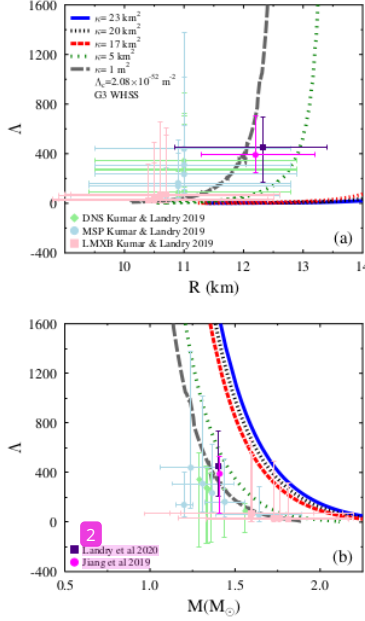


**Figure 7.4:** These are the calculated Love number  $A$  from G3 WHSS EoS with  $\kappa$  variations and  $\Lambda_c = 2.08 \times 10^{-52} \text{ m}^{-2}$ . In panel (a), 2 compare them with data from Kumar-Landry 2019 [82]. In panel (b), we compare them with data from Landry et al 2020 [57] and Jiang et al 2019 [58].

Looking at this, there is one tempting question for us: is it possible to reach maximum mass around  $2.6M_\odot$  while also keep the results still in agreement with the  $1.4M_\odot$  observation data? It turns out we can do this, but with the cost of the unphysical value of  $\Lambda_c$ , i.e., it is negative and its absolute value is much larger than the observed value ( $2.08 \times 10^{-22} \text{ m}^{-2}$ ). Hence, we name this case as an unrealistic case.

The reasons are as follows. Increasing the absolute value of  $\Lambda_c$  shifts the position of the 'tail' to the left (right, resp.), when  $\Lambda_c < 0$  ( $\Lambda_c > 0$ ). What we mean by the tail is the part of the M-R curve that corresponds to the smaller central pressure and, for the case of  $\Lambda_c = 0$ , the tail is positioned at the lower right. In Fig. 7.5, the results from variations of  $\Lambda_c$  are shown for the cases of different  $\kappa$  ( $\kappa = 1 \text{ m}^2$  and  $\kappa = 5 \text{ km}^2$ ) and different EoSs (WHSS and WoutHSS). It is clear that variations of  $\Lambda_c$  impacts the radius greater than from variations of  $\kappa$ , except for the neighborhood of the maximum mass. A positive (negative, resp.) value of  $\Lambda_c$  tends to increase (decrease) the radius.

We compare two different EoSs (G3 WHSS in the upper panels and G3 WoutHSS in the lower panels) in Fig. 7.5. When we increase  $\Lambda_c$ , both  $R$  and  $M$  increase, and vice-versa. From the plots, we can see that for  $\kappa = 1 \text{ m}^2$  and  $\kappa = 5 \text{ km}^2$ , the range of  $\Lambda_c$  can

be constrained with the  $2.0M_{\odot}$  mass constraint and  $1.4M_{\odot}$  mass and radius constraints from observations [57, 58, 71, 72, 73, 7]. The range fo  $\Lambda_c$  for  $\kappa = 1 \text{ m}^2$  is wider i.e.,  $-10^{-7} < \Lambda_c/(\text{m}^{-2}) < 10^{-8}$ , than that of  $\kappa = 5 \text{ km}^2$ , i.e.,  $-10^{-9} \leq \Lambda_c/(\text{m}^{-2}) \leq 10^{-10}$ . Then, by increasing  $\kappa$  value and decreasing  $\Lambda_c$  value, it is possible to have a relatively large maximum mass with relatively small radius. However, for the larger the  $\kappa$  value, the narrower the range of  $\Lambda_c$  value becomes.

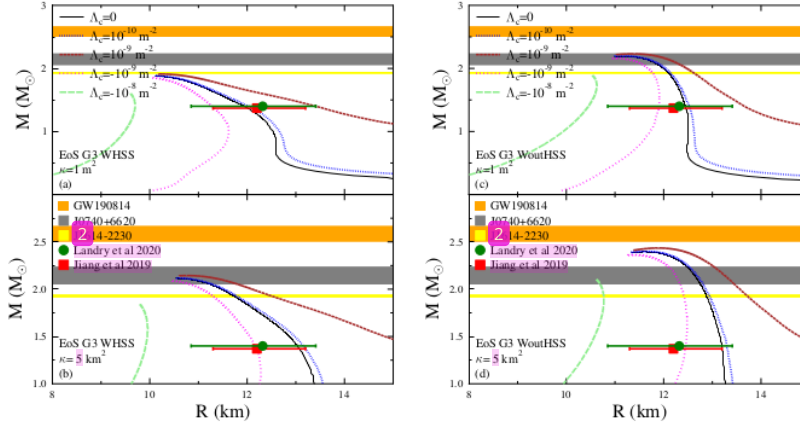


**Figure 7.5:** Here, we show the M-R relation by variations of  $\Lambda_c$ . We use small  $\kappa$  ( $\kappa = 1 \text{ m}^2$ ) and large  $\kappa$  ( $\kappa = 5 \text{ km}^2$ ), respectively, in panels (a) and (b). They are also from using G3 WHSS EoS. The panels (c) and (d) contain the same thing but differ in the EoS, which is WoutHSS.

Thus, we can obtain the M-R curves that satisfy both the  $2.6M_{\odot}$  mass constraint and the radius constraint for  $1.4M_{\odot}$  NS from observations simultaneously. For G3 WHSS and G3 WoutHSS EoSs, we set  $\kappa = 26 \text{ km}^2$  and  $\kappa = 13 \text{ km}^2$ , respectively, and use an unavoidably large and negative  $\Lambda_c$ . Yet, the range of  $\Lambda_c$  is narrow, i.e.,  $\Lambda_c = -(2.4 - 3.2) \times 10^{-9} \text{ m}^{-2}$ . These results are shown in Fig. 7.6. Note that when  $\Lambda_c \geq 0$ , both canonical mass radii and maximum mass constraints cannot be satisfied simultaneously. The results from G3 WHSS EoS yield more significant radius shifting by varying  $\Lambda_c$  than that of G3 WoutHSS EoS because usually, the equations used  $\lambda$  rather than  $\Lambda_c$ .

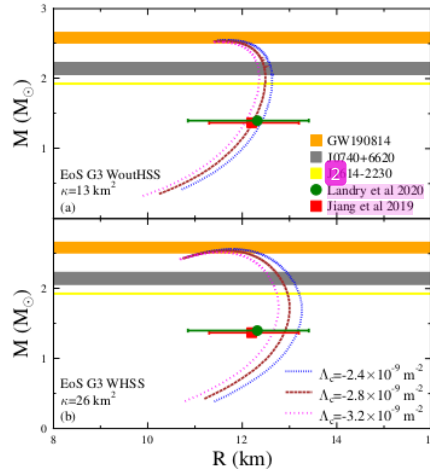


**Figure 7.6:** These are M-R curves from different EoSs [G3 WoutHSS in panel (a) and WHSS in panel (b)]. These curves satisfy both the data from Landry *et al.* and Jiang *et al.* and the mass constraint from the GW190814 data.

We show the sensitivity of  $\kappa$  and  $\Lambda_c$  variations in Fig. 7.7. There, the M-R curves satisfy both the radius constraint for canonical mass NSs from observations [57, 58] and the  $2.6M_\odot$  mass constraint from GW190814 [6]. The range of variations of both parameters is narrow. It is evident from the lower panel of Fig. 7.7 that in this region the radius is quite sensitive to  $\Lambda_c$  variation.

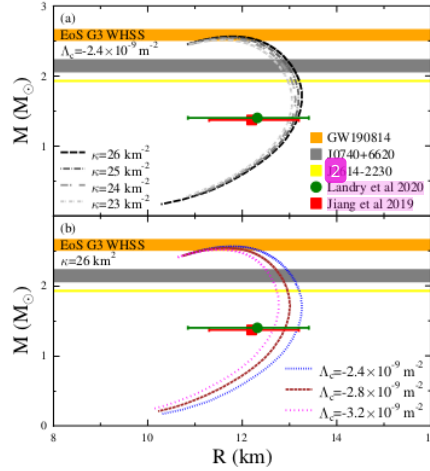


**Figure 7.7:** These are M-R relations from G3 WHSS with variations of  $\kappa$  in panel (a) and variation of  $\Lambda_c$  in panel (b). These parameters' values are chosen so that they satisfy the data from Landry *et al.* and Jiang *et al.*, while simultaneously maintain their maximum mass at the range provided by the GW190814 data.

10

For completeness, we show the impact of  $\kappa$  variation on the moment of inertia and the Love number in Figs. 7.8 and 7.9, respectively. We can see that moment of inertia and Love number are not too sensitive with variations of  $\kappa$  and the results are quite compatible with the NS's tidal deformability observations from Refs. [82, 57, 58, 79, 80, 6].

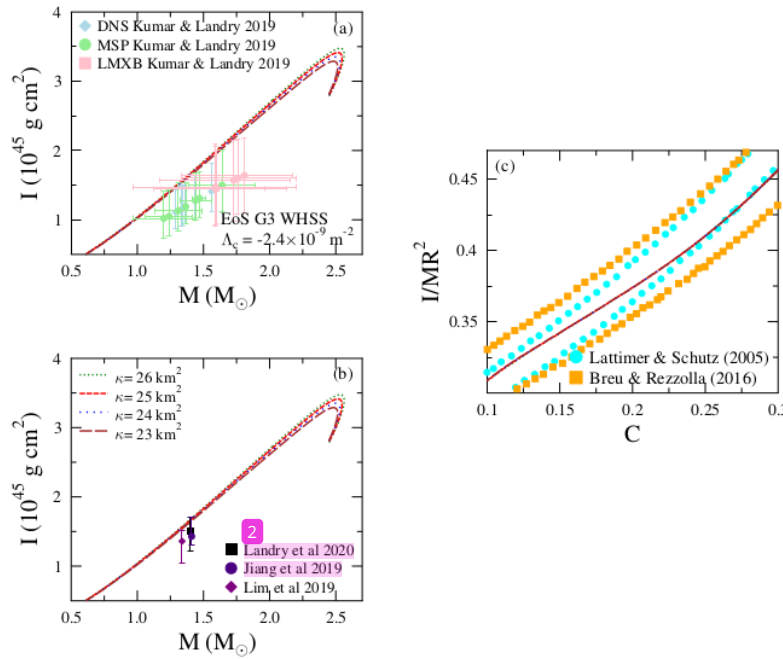


**Figure 7.8:** Moment of inertia within EiBI obtained from G3 WHSS EoS with variations of  $\kappa$  and very large and negative  $\Lambda_c$ .

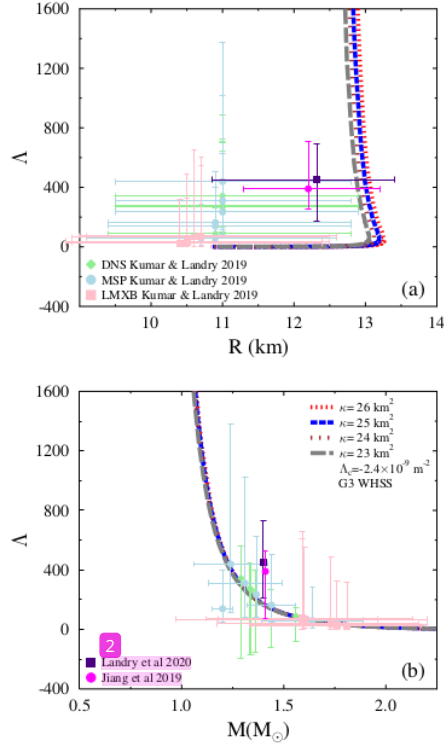


**Figure 7.9:** The tidal deformation with  $\kappa$  varied and negative with very large value of  $\Lambda_c$ .

To this end, we must consider the later results very carefully. The  $2.6M_\odot$  mass constraint and the canonical NS  $R_{1.4M_\odot}$  radius constraint, which is  $11 \text{ km} \lesssim R_{1.4M_\odot} \lesssim 13 \text{ km}$ , can only be satisfied by EiBI gravity if the cosmological constant satisfies: (1)  $\Lambda_c < 0$  and (2)  $|\Lambda_c|$  is unphysically large. We know, however, that our universe has a positive and tiny cosmological constant [133, 134, 135, 136]. Therefore, we conclude that the  $2.6M_\odot$  object observed in GW190814 event [6] is not likely an NS within the EiBI theory.

## 7.4 Conclusions

Motivated by the question of whether the  $2.6M_\odot$  mysterious object observed in the GW190814 event could be an NS or not, here we investigate the role of parameter  $\kappa$  and  $\Lambda_c$  from EiBI gravity on the mass-radius relation, the moment of inertia, and the tidal deformability of an NS. The EoS in the core of NS is calculated using the RMF model

using the G3 parameter set [34]. To determine the hyperon coupling constants, we use the SU(3) prescription and the hyperon potential depths [94]. In the inner and outer crusts, we use the EoS from Miyatsu *et al.* [99]. We also employ a constraint on the speed of sound in the NS matter such that to not exceed  $c/\sqrt{3}$  at high densities. The predictions from the G3 parameter set are shown to be compatible with the experimental nuclear matter data and the NS-related properties, including the nuclear matter EoS at intermediate density.

We have shown that the NS mass  $M$  depends significantly on the value of  $\kappa$ . For  $\kappa > 0$ , the NS maximum mass increases when the  $\kappa$  value increases. For  $\kappa < 0$ , the NS maximum mass decreases when  $|\kappa|$  value increases. On the other hand, the value of  $\Lambda_c$  affects the NS radius  $R$ . For  $\Lambda_c > 0$ , the NS radius tends to increase when  $\Lambda_c$  value increases. For  $\Lambda_c < 0$ , the NS radius tends to decrease when  $|\Lambda_c|$  value increases.

We have also found for G3 with hyperon and speed of sound treatment at high densities (G3 WHSS),  $\kappa \approx 5 \text{ km}^2$  and  $\Lambda_c$  value  $\leq 2.08 \times 10^{-52} \text{ m}^{-2}$ , which is the cosmological constant from observations, then the mass-radius relation satisfies both the NS  $M \sim 2.0M_\odot$  and canonical mass-radius observation constraints [57, 58, 71, 72, 73, 7]. If we use EoS without hyperons but still use the speed of sound constraint (G3 WoutHSS), then the constraints can be satisfied even with a much smaller  $\kappa$  value.

We have also found that the G3 WHSS and G3 WoutHSS EoSs can both satisfy the  $2.6M_\odot$  mass requirement and recent observation analysis [82, 57, 58, 79, 80, 6] simultaneously. However, the  $\kappa$  value will be relatively large and the  $\Lambda_c$  value is unphysically large and negative. This unphysical aspect means that at the range of the solar system, Newtonian gravity breaks down.

Hence, if the EiBI gravity is the description of our universe and the accepted value of the physical cosmological constant value is very small and positive, then the  $2.6M_\odot$  object observed in GW190814 event [6] is not likely an NS.

## CHAPTER 8

### CONCLUSIONS

In this chapter, we present our conclusions from the first and second parts of our work shown in chapters 6 and 7.

#### 8.1 First part

In this first part of our work, we discuss the SCGrav much further and conclude with the following.

In this work, we use linear EoS. Then the structure of the Eqs. (6.17)-(6.29) constraints the range of both  $\alpha$  and  $w$  at the center. It turns out that the results are not significantly different from the usual TOV GR system. Thus, it is similar to the conclusion in Ref. [53] which says that the ultra-compact objects (UCOs) from a linear equation of state in the semi-classical gravity's negative branch are unable to generate gravitational echoes if the speed of sound is  $c/\sqrt{3}$ . This speed of sound's upper bound came from QCD. Above this, i.e. the speed of sound is  $c$  which is from causality condition, a UCO can be produced, hence there is a gravitational echo from these objects. But then, these UCOs are not generated from adjusting the parameters from the semi-classical theory.

On the other hand, the positive branch is still open for more numerical analysis. We expect that, in this branch, the quantum effect from the semi-classical terms is significant for ECO.

The numerical verification is also discussed. Although most of it discusses the reproduction of the results from the literature, these are crucial since numerical treatment for the positive branch is not the same as the negative branch. We found that the equations from the negative branch can be integrated and give the same results regardless of the starting point of integration, i.e., one can integrate from the center of the star to its surface or from surface to center. The former is called forward integration and the latter is called backward integration. On the other hand, the equations from the positive branch can give a different result if we compare the results from forward integration and backward integration.

Another interesting aspect discussed in the numerical verification is that for the negative branch, choosing negative central mass  $m_c$  and  $\rho = \text{constant}$  can give compactness very near the black hole limit. This is larger than our results which from zero  $m_c$ , which only gives us compactness slightly larger than the Buchdahl bound, even though we also

set  $\rho = \text{constant}$ .

## 8.2 Second part

In the 7 second part of our work, we discussed the role of cosmological constant  $\Lambda_c$  in the EiBI gravity. The NS core EoS is calculated using the RMF model with the G3 parameter set [34] for both excluding and including hyperons contributions and the speed of sound is constrained to not exceeding  $c/\sqrt{3}$  at high densities, denoted by WoutHSS and WHSS.

We find that if we use the observed data  $\Lambda_c = 2.08 \times 10^{-52} \text{ m}^{-2}$  as an upper bound, then only  $2.1M_\odot$  constraint can be reached if  $\kappa \simeq 5 \text{ km}^2$  and G3 WHSS EoS is used. Using G3 WoutHSS EoS will give us a slightly higher maximum mass. The  $2.1M_\odot$  constraint from the GW190814 event cannot be reached if the radius constraint for canonical mass  $1.4M_{10}$  NSs from observations should also be satisfied. This radius constraint is crucial so that the moment of inertia and tidal deformation results are also in agreement with data from observations.

We also find that using  $|\Lambda_c|$  larger than this value can give us an interesting but unphysical result. The G3 WHSS (with hyperons) and G3 WoutHSS (without hyperons) EoSs can satisfy the  $2.6M_\odot$  constraint and the canonical mass-radius observation constraints, simultaneously, only if the  $\kappa$  value is relatively large ( $\kappa = 13 \text{ km}^2$  for G3 WoutHSS EoS and  $\kappa = 26 \text{ km}^2$  for G3 WHSS EoS) and the absolute  $\Lambda_c$  value is too large ( $|\Lambda_c| \lesssim 10^{-9} \text{ m}^{-2}$ ) while its sign is negative. From these choices, the moment of inertia and the tidal deformability predictions from them is still compatible with recent observation analysis results.

Since the accepted value of the cosmological constant is positive and very small ( $\Lambda_c = 2.08 \times 10^{-52} \text{ m}^{-2}$ ), we conclude that the second object with mass  $2.6M_\odot$  observed in GW190814 event [6] is not likely an NS.

# Ilham Prasetyo V9 dissertation

## ORIGINALITY REPORT



## PRIMARY SOURCES

- |   |   |      |
|---|---|------|
| 1 | N. Liliani, J. P. Diningrum, A. Sulaksono. "Tensor and Coulomb-exchange terms in the relativistic mean-field model with -meson and isoscalar-isovector coupling ", Physical Review C, 2021<br>Publication | 1 %  |
| 2 | Ishfaq Ahmad Rather, Anisul Ain Usmani, S K Patra. "Hadron-Quark phase transition in the context of GW190814", Journal of Physics G: Nuclear and Particle Physics, 2021<br>Publication                    | 1 %  |
| 3 | mafiadoc.com<br>Internet Source   | <1 % |
| 4 | Submitted to Universitas Negeri Jakarta<br>Student Paper  | <1 % |
| 5 | Pei-Ming Ho, Yoshinori Matsuo. "Static black hole and vacuum energy: thin shell and incompressible fluid", Journal of High Energy Physics, 2018<br>Publication  | <1 % |

- 6 R. Rizaldy, A. R. Alfarasyi, A. Sulaksono, T. Sumaryada. "Neutron-star deformation due to anisotropic momentum distribution of neutron-star matter", Physical Review C, 2019  
Publication <1 %
- 7 A. I. Qauli, M. Iqbal, A. Sulaksono, H. S. Ramadhan. "Hyperons in neutron stars within an Eddington-inspired Born-Infeld theory of gravity", Physical Review D, 2016  
Publication <1 %
- 8 inba.info Internet Source <1 %
- 9 Submitted to Fakultas Ekonomi Universitas Indonesia Student Paper <1 %
- 10 T. K. Chan, AtMa P. O. Chan, P. T. Leung. "Universality and stationarity of the I-Love relation for self-bound stars", Physical Review D, 2016  
Publication <1 %
- 11 M. L. Pattersons, A. Sulaksono. "Mass correction and deformation of slowly rotating anisotropic neutron stars based on Hartle-Thorne formalism", The European Physical Journal C, 2021  
Publication <1 %
- 12 arxiv.org

Internet Source

<1 %

13 eprints.ucm.es

Internet Source

<1 %

14 link.springer.com

Internet Source

<1 %

15 Neeraj Pant, Satyanarayana Gedela, Ravindra K. Bisht. "Stellar modeling with the Einstein-Maxwell field equations via gravitational decoupling", Chinese Journal of Physics, 2021

Publication

<1 %

16 indico.ectstar.eu

Internet Source

<1 %

17 www.classicistranieri.com

Internet Source

<1 %

18 Ahmad A. Kamal. "Gravitation", 1000 Solved Problems in Classical Physics, 2011

Publication

<1 %

19 Norbert Straumann. "General Relativity", Springer Nature, 2004

Publication

<1 %

20 Gonzalo J. Olmo, Diego Rubiera-Garcia, Aneta Wojnar. "Stellar structure models in modified theories of gravity: Lessons and challenges", Physics Reports, 2020

Publication

<1 %

- 21 Doan Thi Loan, Ngo Hai Tan, Dao T. Khoa, Jerome Margueron. "Equation of state of neutron star matter, and the nuclear symmetry energy", Physical Review C, 2011  
Publication <1 %
- 
- 22 d-nb.info Internet Source <1 %
- 
- 23 Submitted to Arab Open University <1 %  
Student Paper
- 
- 24 Submitted to Higher Education Commission Pakistan <1 %  
Student Paper
- 
- 25 Luca Baiotti. "Gravitational waves from neutron star mergers and their relation to the nuclear equation of state", Progress in Particle and Nuclear Physics, 2019  
Publication <1 %
- 
- 26 P. Betzios, E. Kiritsis, V. Niarchos. "Emergent gravity from hidden sectors and TT deformations", Journal of High Energy Physics, 2021  
Publication <1 %
- 
- 27 mdpi-res.com Internet Source <1 %
-

Exclude quotes

On

Exclude matches

< 17 words

Exclude bibliography

On